MAGNETIC SURFACE RELAXATION AND RECONSTRUCTION PHENOMENA IN FRUSTRATED MAGNETIC SYSTEMS

by

MELANIE SARAH HOPPER

A thesis submitted to
The University of Birmingham
for the degree of
DOCTOR OF PHILOSOPHY

School of Physics and Astronomy
The University of Birmingham

September 2010

Abstract

This thesis is concerned with magnetism at the surfaces of frustrated magnets, and in particular with magnetism on face-centred cubic (FCC) lattice systems. Normally, magnets do not react to a surface. Frustrated magnets do, however, and we consider two cases: Magnetic relaxation and the more unusual magnetic reconstruction phenomenon. Magnetic relaxation involves the extinction near the surface of a magnetic order that is present in the bulk and exists as a type of magnetic domain wall. Calculations of the ground state configuration of a semi-infinite system of uranium dioxide, an FCC triple-q magnet, show a solitonic solution corresponding to this relaxation. Fluctuations of this domain wall are considered in order to explain the unusual disordering observed experimentally in the near-surface region at a temperature below the bulk ordering transition temperature. The rarer case of reconstruction involves completely new magnetic order from the bulk appearing at the surface spontaneously and at a temperature below the bulk ordering transition temperature. Analysis of this phenomenon is undertaken via the construction of a phase diagram for a frustrated square lattice Heisenberg model. Regions of the phase diagram are found to exist in which the reconstruction is expected to occur, and furthermore the results can be mapped directly to type-1 FCC lattice systems.

Acknowledgements

Firstly I'd like to thank my supervisor Dr Martin Long for being such an inspiration these past few years and opening my eyes to the wonders that can be reached by pursuing academic research. I have learnt so much and hope that I will continue to challenge my mind. It has been an honour to be able to study the field in such depth and with such a talented physicist and mathematician. Thank you, Martin, for always having the door open (especially to questioning that at times I'm sure has been unbelievably repetitive), for having such patience and for persevering with me. Thank you also to my second supervisor Jorge for his wonderful support and insightful discussions and ideas, as well as his hospitality at the Rutherford Appleton Laboratory. It was always a real pleasure to visit the labs and discuss physics with Jorge, I always left feeling incredibly motivated, inspired and frankly proud to be studying physics at such a level. Since leaving research it is those lab visits that I miss the most.

Thanks also go to my fellow postgraduates, especially to Martyn and Tom for their wonderful and constant support and astonishingly high tolerance for having their ears talked off. Thank you in particular to my friend Helen who has been my rock. My first port of call in any crisis, I don't know what I would have done without her. She has been there for me through the worst, offering wise words, comfort, and also of course her hard cash many a time to a certain Seattle-based coffee company at the drop of a hat.

Thank you to Tom for offering to edit my references during the final sprint to the finish and whatsmore doing this incredibly dull and monotonous task with fervour and perfection, I knew I could rely on him to do a grand job (of course as long as persistent cups of good quality coffee were supplied). Thank you also to Denis for, to be honest, probably proofreading more of my thesis than I in the run up to my viva and offering practice examinations and general discussion at any time, I am truly grateful.

Finally, and most importantly, I'd like to thank my parents and sister Manda, whose sturdy and unconditional support has been beyond words. I am immensely lucky to have been blessed with such a wonderful family who are also my best friends. They have put up with a lot as I have ridden the emotional rollercoaster that is doctorial research and they have been there with encouragement and support, day and night.

The past couple of years in particular have brought some really tough times, but I have pulled through and completed this work because I have the support of some truly amazing people, many of whom I have not had room to mention, but hopefully will know how incredibly important they are. Thankyou, I am so glad, lucky and proud to know you all.

To my parents and sister Manda

....

"It is not the possession of truth, but the success which attends the seeking after it, that enriches the seeker and brings happiness to him" - Max Planck

"Less brute force and ignorance" - Martin W Long

....

Contents

List of Figures

Chapter 1

INTRODUCTION

This thesis investigates the magnetic surface of face-centred-cubic(FCC) magnets. FCC magnets possess geometric frustration in the form of exotic multiple-q magnetism, which in turn leads to the possibility of access to degenerate magnetic states. As a result, the magnetic spins can react to the inclusion of a surface in interesting, and in one of the cases we shall be presenting, novel ways. In particular, these states can possess more than one magnetic order parameter, in the form of multiple Bragg spots. As such, FCC lattice materials have the potential to reorient the magnetic spins in reaction to a change in a parameter, and in some cases to completely alter the magnetic translational symmetries present in the system. This change in parameter can be in the form of, for example, temperature, uniaxial stress or impurity concentration. The focus of this research is the investigation of how such systems react to the introduction of a surface, which can be thought of as an impurity to a system which in its pure form extends to infinity in all dimensions.

The behaviour of materials at surfaces is a discipline in its own right - whereas some treat the surfaces as an inevitable but unwanted disorder effect that impacts negatively on their bulk measurements, others embrace the resulting properties of the material. We consider the case of pure surfaces, ignoring effects such as leaching, roughening etc.

The effect of the presence of a surface on the chemical make up of a material

is well studied. The system alters in order to minimise the number of the dangling bonds present due to the broken chemical bonds. This can be realised by either *rearrangements* of the atoms, whereby the atoms are displaced from their bulk positions but maintain the bulk periodicity, or *reconstructions* of the surface, which alters the periodicity from that in the bulk such that the symmetry parallel to the surface becomes lower than the bulk.

Reconstruction can result in highly complex structures, such as one of the most heavily studied; the Si(111) 7x7 reconstruction[1][9]. The currently accepted geometry is that of a Dimer-adatom-stacking fault, the DAS model, first proposed by Takayanagi *et al* [10] and illustrated in fig 1.1. The surface geometry involves 12 adatoms per unit cell, 6 rest atoms (those that have not been saturated by adatoms) sitting 1 layer below this new 'surface' that are 3-fold co-ordinated, and vacancies at the corners of the unit cell. Fig 1.2 details these different building blocks as well as others found on other silicon surface geometries. Half of the new unit cell has a stacking sequence identical to the bulk, whereas the other half does not. The result is four layers at the surface that are reconstructed compared to the bulk chemical geometry, with 19 broken chemical bonds, or dangling bonds, pointing towards the vacuum. The translational symmetry parallel to the surface is as a result lowered, as described by the unit cell, which alters from being defined as 1x1 to be 7x7.

Analogous to this are the magnetic relaxation and reconstruction phenomena, both of which are studied in this thesis. In comparison with the system minimising the number of dangling bonds by atomic relaxation or reconstruction, the system minimises the magnetic energy lost from broken magnetic bonds by orienting spins to have minimum frustration. This can be achieved by orienting spins to have less frustration parallel to the surface than perpendicular. In this way the introduction of the surface takes away the frustration and magnetic energy lost from broken bonds can be compensated for. The energetically-favourable orientation can be understood by considering spins surrounding a spin on the surface as a local field.

Loss of bonding can alter the local field if the spins are non-collinear, resulting in a relaxation of the spins towards the surface. Alternatively, if the spins are collinear relaxation cannot occur, *but* the new phenomenon of magnetic reconstruction can under certain circumstances, where new order is introduced at a 'surface-ordering' temperature. In this way a 'new' local field is introduced at the surface which results in an energetically-favourable reorientation of the spins, compensating for the lost bonding.

The analogy of magnetic relaxation to chemical relaxation can be considered by defining magnetic relaxation as the 'displacement', or perturbation, of the magnetic spins from their bulk state, which constitutes a reorientation of the spin direction, but with no underlying change in symmetry parallel to the surface. This includes, among other examples, the case of uranium dioxide which is one of the studies within this thesis. In this case, there is an altering of the magnitude of order in the near surface region from the bulk, but the translation symmetry perpendicular to the surface remains the same. The case of magnetic surface *reconstruction* which constitutes the second study within this thesis is the more exotic case and is a completely new phenomenon previously not thought possible. It is the exotic class of multiple-q magnets that possess the characteristics required for this new type of reconstruction.

The recent reignited interest in surface magnetism has come about due to recent advances in experimental techniques that have as a result become capable of probing the near-surfaces of materials to high enough accuracy. Experimental techniques for imaging surfaces have been developed over the years to include 'purely surface layer' techniques, such as atomic force microscopy, and those that penetrate a finite depth into the material with a function-dependent absorption profile, such as LEED. An example of the application of LEED can be seen in figs. 1.3 and 1.4 which shows the depth profiling of the Si surface reconstruction discussed earlier. These techniques have been used previously for determining atomic and electronic structure, but so

3
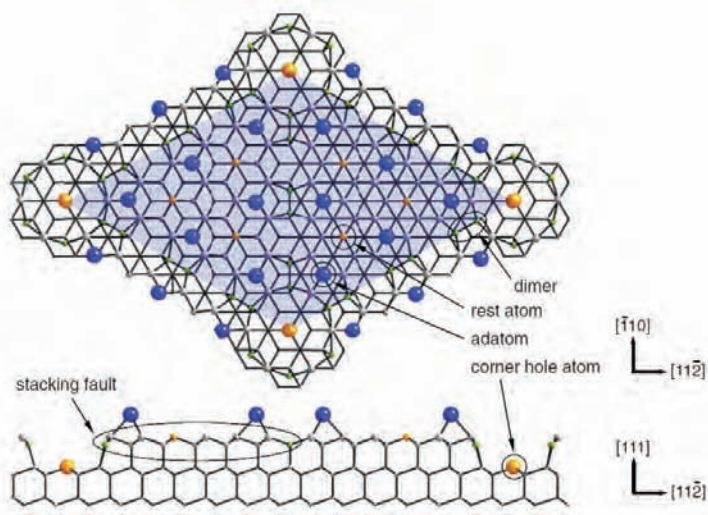
Figure 1.1: *The DAS mode for the Si(111) 7x7 surface reconstruction[1]*
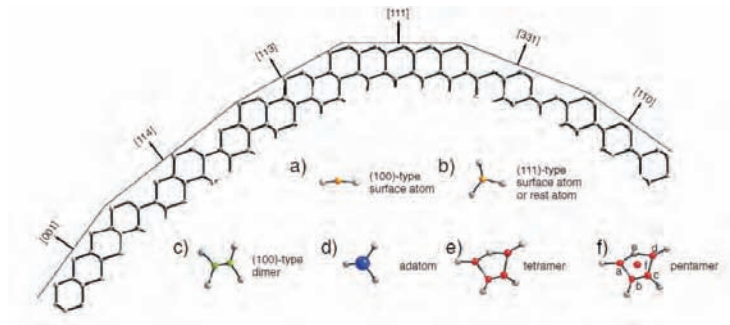
Figure 1.2: *Building blocks of the Si surface reconstruction [1]*

far not magnetic structure due to the difficulty or impossibility of coupling the magnetism to the probe. However, there have been advances in recent years whereby techniques originally used to determine either atomic and electronic structures on the surface, or magnetic structure in the bulk, have been tailored to probe the magnetism at the surface of the samples and are becoming very powerful tools.

Depth-profiling near surfaces is no mean feat, and there have been several different experimental techniques used in the past to achieve it, to varying degrees of success. Depth selective conversion electron Mössbauer spectroscopy (MS) has been performed[11] to examine hematite and $FeBO_3$ crystals. This is a great method for depth profiling with accuracy, however the compound must consist of the one of the MS probing atoms, for example ^{57}Fe.
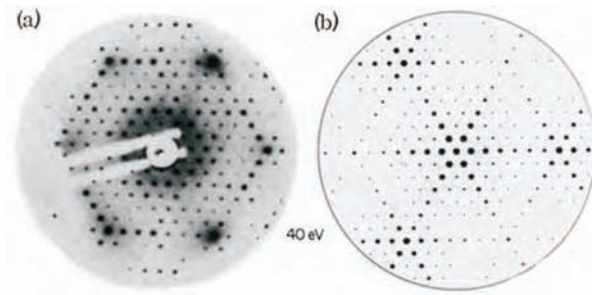
Figure 1.3: *LEED measurement at 40eV of Si with a (111) surface [2]. Since the electron mean free path is very small, only one graphite-like layer primarily contributes to the scattering*

At first sight neutron scattering seems unsuited to be a surface probe due to the penetrating nature, and only samples with a large surface-to-bulk ratio could give reasonably-sized signals for the surface, for example fine powders. However glancing angle scattering can provide reasonable resolution and the analysis is performed by examining lateral cuts across the resulting truncation rods. Evanescent neutron scattering has also provided decent results [12] and can be used simultaneously. However, the minimum escape-depth (scattering depth) of evanescent neutrons is in most cases around 100 Å for angles lower than the critical angle of the sample. As such, the probe is not good enough for probing effects *very* close to the surface, nor purely 2D magnetic phenomena, *unless* the material is highly-absorbing, for example Gd[12].

Watson *et al* [13] have developed evansecent magnetic x-ray scattering to obtain data for near-surface regions of semi-infinite systems, made possible by relatively recent access to synchrotron radiation light sources. The depth weight functions involved in this method are exponentials, which makes accurate depth profiling tricky, but again, lateral analysis across truncation rods can bear fruit.

The pioneering work on the behaviour of the order parameter near the surface of antiferromagnets was undertaken decades ago on ultrafine hematite particles where it was found that there was a magnetic behaviour in the first few atomic layers that was different from that of the bulk. The work was then extended to thin films, and then to magnetism near surfaces of larger crystals resulting in the observation of a
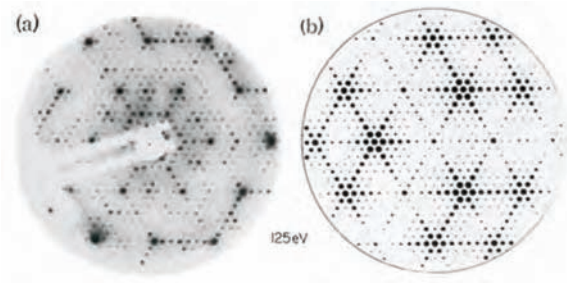
Figure 1.4: *LEED measurement at 125eV of Si with a (111) surface [2]*

range of phenomena.

Ginzburg-Landau theories have been applied to magnetism at surfaces in order to obtain critical laws and exponents for the associated magnetic behaviour. The theories concern the enhancement of or decrease in magnetic surface coupling as the causes of magnetic phenomena associated with the near-surface. If the surface coupling is enhanced, then one can expect, in terms of approaching the magnetic ordering temperature from above, the surface to magnetically order *before* the bulk, with the depth of the near-surface region being given by the magnetic correlation length. Below the bulk transition temperature the surface should exhibit an enhanced order parameter value compared to that of the bulk. If conversely the coupling is decreased at the surface, then the bulk is expected to order first, at the 'original' bulk transition temperature, and this order then to leak to the surface, such that magnetic ordering is only present *below* the bulk transition temperature. In this case, the near-surface has decreased order from the bulk at any temperature but *identical* order, and so has no phase transition associated solely with itself. However no literature has so far been concerned with magnetic surface ordering transitions that occur independently and what's more *below* the bulk ordering temperature, and it is this type of transition that this thesis will provide theoretical evidence for, along with preliminary proposals that the theory has in fact already been experimentally observed. This is the magnetic reconstruction phenomenon and we find that multiple-q systems, in particular type-1 FCC magnetic materials, are prime candidates for this unique transition.

The magnetic reconstruction is studied by determining a phase diagram for a semi-infinite square lattice system with frustration, modelled by a Heisenberg Hamiltonian. A phase boundary to the reconstruction is found and the configuration determined explicitly for some locations of the phase diagram. The study allows the development of ideas that lead to a statement of the criteria needed for magnetic reconstruction to occur. In addition, and of great significance, it is shown that the results for the square lattice can be mapped directly onto an FCC type-1 magnet.

The second investigation within this thesis concerns magnetic surface studies of UO_2, for which interesting phenomena has been observed experimentally, in terms of unusual magnetic disordering behaviour of the near-surface region at a temperature below the bulk ordering temperature. The ground state of the semi-infinite system is determined using a Heisenberg Hamiltonian with appropriate anisotropy terms and is found to take a solitonic form, describing a domain wall between a 2q state on the surface and a 3q state in the bulk . The determination of the ground state provides a basis for understanding how thermal fluctuations may disorder the system. Literature containing fluctuation calculations based on this ground state is consulted [14] and a picture for what the unusual disorder observed may correspond to provided. In addition, the phenomenon of wetting is considered for the system in question, but a different theory is proposed as a more likely scenario, in which fluctuations of the domain boundary present in the system between the 2q and 3q states descend towards the bulk on the increase of temperature. This movement of the wall does not need to be discontinuous to explain the unusual sharp behaviour observed, since the increase of the length scale associated with the fluctuations could simply be increasing past the length scale of the depth probe which would show up in this way.

We begin this thesis by introducing the main principles behind the determination of magnetic spin configurations, followed by a review of multiple-q magnetism and associated transitions and magnetic surface transitions, before beginning our

two studies: magnetic surface relaxation in uranium dioxide and magnetic surface reconstruction.

Chapter 2

DETERMINING CLASSICAL SPIN CONFIGURATIONS

In this chapter, we detail how one determines the spin configuration of magnets for different lattices and interactions. The method is based on the use of a Bloch transform, and the subsequent minimisation of the energy as performed in reciprocal space subject to appropriate constraints. The determination of spin configurations in turn leads us to classify different types of magnets according to the spin state degeneracies they possess in the ground state. The second part to this chapter involves solving for the magnetic state of different types of lattice. It is here that we introduce multiple-q magnetism and study the magnetism of the FCC lattice with nearest neighbour coupling, which will be the foundation of our subsequent studies.

2.1 Diagonalisation

The Bloch transform can be used to diagonalise any Hamiltonian that describes a system of discrete sites that possesses periodicity. A system possesses periodicity if the potential viewed from any particular atom is equivalent to that of any other, and as such the translation through any vector joining two atoms is thereby a symmetry of the system. A lattice that possesses this property is known as a Bravais lattice, and it is the translational symmetry of these lattices that is exploited in order to

diagonalise the Hamiltonian as will be shown in the next few sections.

The diagonalisation of the Hamiltonian is achieved by using the property that commuting operators can be simultaneously diagonalised (or, more precisely, block-diagonalised). It will be shown below that any symmetry operator of the Hamiltonian commutes with the Hamiltonian and thus, if one can find a symmetry of the Hamiltonian and determine the basis in which the symmetry is diagonalised, one can reduce or even solve the problem of diagonalising the Hamiltonian by transforming it into this basis.

Consider two operators: $\hat{H}$, a Hamiltonian which is necessarily a hermitian operator, and $\hat{U}$, a unitary operator. A symmetry of the Hamiltonian is defined as any unitary transformation that leaves the Hamiltonian invariant. As such, if

$$\hat{H}\lambda = \phi \tag{2.1.1}$$

for the two wavefunctions λ and ϕ, then the Hamiltonian should also map the transformed wavefunctions onto each other too:

$$\hat{H}\hat{U}\lambda = \hat{U}\phi. \tag{2.1.2}$$

Since the unitary operator can be inverted, we can write

$$\hat{U}^{-1}\hat{H}\hat{U}\lambda = \phi = \hat{H}\lambda \tag{2.1.3}$$

and since this must be true for all wavefunctions, we find that

$$\hat{U}^{-1}\hat{H}\hat{U} = \hat{H}, \tag{2.1.4}$$

which leads us to the commutation relation

$$[\hat{H}, \hat{U}]_- = 0. \tag{2.1.5}$$

Hence, a unitary operator, $\hat{U}$, that is a symmetry of the Hamiltonian has the property that it commutes with the Hamiltonian.

Next, we show that commuting operators can be simultaneously diagonalised. We remind the reader that hermitian operators have real eigenvalues, and that eigenvectors associated with distinct eigenvalues are automatically orthogonal. This is also true for unitary operators, as we shall now show by visiting the inner product definition.

For unitary operators,

$$\hat{U}|u\rangle = u|u\rangle, \tag{2.1.6}$$

the following inner product equation is satisfied:

$$(u, u') = (\hat{U}u, \hat{U}u') \tag{2.1.7}$$

and so, acccording to the eigenvalue equation above,

$$(u, u') = u^* u'(u, u'). \tag{2.1.8}$$

11

Writing the inner product using bra and ket notation and we see that

$$(1 - u^* u')\langle u | u' \rangle = 0. \tag{2.1.9}$$

Thus, substitution of $u = u'$ unveils that the eigenvalues u have unit modulus, and that therefore eigenvectors corresponding to distinct eigenvalues are orthogonal. Given this property, and that $\hat{U}^\dagger = \hat{U}^{-1}$, one can write

$$u'(u, u') = (u, \hat{U} u') = (\hat{U}^\dagger u, u') = (\hat{U}^{-1} u, u') = (u^{-1})^* (u, u') = u(u, u'). \tag{2.1.10}$$

As such, one can still use the notation $\langle u | \hat{U} | u' \rangle$ for eigenstates of a unitary operator and allow $\hat{U}$ to operate in both directions.

Using this allowed notation and the property of commuting operators already discussed, one can consider picking a basis in which $\hat{U}$ is diagonal and see how $\hat{H}$ acts in this basis. We write down the matrix elements in the following form to exploit the properties discussed above:

$$u\langle u | \hat{H} | u' \rangle = u\langle u | \hat{U} \hat{H} | u' \rangle = \langle u | \hat{H} \hat{U} | u' \rangle = \langle u | \hat{H} | u' \rangle u' \tag{2.1.11}$$

and can therefore write

$$(u - u')\langle u | \hat{H} | u' \rangle = 0. \tag{2.1.12}$$

From this, we see that if one considers the matrix elements of $\hat{H}$ that couple eigenvectors corresponding to *different* eigenvalues, then the matrix elements are

zero and we have 'block-diagonalisation', whereby the matrix H can be written such that the elements are non-zero only in 'blocks' of matrix elements that follow the diagonal of the matrix:

$$
\begin{bmatrix}
\begin{bmatrix} H_1 \end{bmatrix}_{u_1} & 0 & \dots & 0 \\
0 & \begin{bmatrix} H_2 \end{bmatrix}_{u_2} & \dots & 0 \\
. & . & \dots & . \\
. & . & \dots & . \\
. & . & \dots & . \\
0 & 0 & \dots & \begin{bmatrix} H_N \end{bmatrix}_{u_N}
\end{bmatrix}
$$

Each of these blocks only contain elements that correspond to identical eigenvalues u_n, and as such are independent of other blocks. To completely diagonalise this matrix, one then needs to determine other symmetries of H that 'decouple' the remaining dependence within the blocks. The final operation that fully diagonalises H is constructed by multiplying these unitary transformations together.

2.2   Bloch Transform

To diagonalise a Hamiltonian that describes a Bravais lattice, one exploits the periodicity of the lattice, using the translational symmetry of translation by 1 atom in 1 direction, $\hat{T}$. The overall diagonalisation involves separating out the different dimensions of the lattice and dealing with each one one-at-a-time. Note that the

Bloch transform that is related to a single dimension serves to *block*-diagonalise the Hamiltonian (unless of course the problem is in 1D, in which case the Hamiltonian will be fully diagonalised).

Our first step is to diagonalise $\hat{T}$ after applying periodic, or ring boundary conditions in order to make the matrix a finite size.

$\hat{T}=$

$$
\begin{bmatrix}
0 & 1 & 0 & 0 & 0 & 0 \\
0 & 0 & 1 & 0 & 0 & 0 \\
0 & 0 & 0 & 1 & 0 & 0 \\
. & . & . & . & . & . \\
. & . & . & . & . & . \\
0 & 0 & 0 & 0 & 0 & 1 \\
1 & 0 & 0 & 0 & 0 & 0
\end{bmatrix}
$$

One thereby obtains the normalised eigenvectors $\mathbf{c}_n$ and eigenvalues t_n that are given by

$$
\mathbf{c}_n = \frac{1}{\sqrt{L}} \exp\left(\frac{i2\pi n}{L}j\right) \tag{2.2.1}
$$

$$
t_n = \exp\left(\frac{i2\pi n}{L}\right), \tag{2.2.2}
$$

where n labels the eigenvector (and corresponding eigenvalue), j labels the elements of the eigenvector, being the original position integer describing the location of the atoms on the lattice, and L is the number of atoms within the translation direction in the lattice, i.e. in the corresponding single dimension we are currently dealing with. By convention, one makes the parameterisation

$$
k = \frac{2\pi n}{L}, \tag{2.2.3}
$$

where k is called the Bloch momentum. One must restrict the range of k in order to get distinct eigenstates and prevent overcompleteness. This idea leads to the representation of $\mathbf{k}$ in reciprocal space, as becomes more apparent if we generalise the Bloch transform to multi-dimensions....

The eigenbasis for diagonalising the Hamiltonian is the set of eigenstates that are each comprised of the multiplication of the translation eigenstates corresponding to each dimension:

$$\mathbf{c} = \frac{1}{\sqrt{N}}.e^{\frac{i2\pi n_1}{L_1}x}e^{\frac{i2\pi n_2}{L_2}y}e^{\frac{i2\pi n_3}{L_3}z} \tag{2.2.4}$$

$$= \frac{1}{\sqrt{N}}.e^{i\mathbf{k}.\mathbf{R}_j}, \tag{2.2.5}$$

where $N = L^3$, the total number of spins in the lattice, $\mathbf{k} = (k_1, k_2, k_3)$ and $\mathbf{R}_j = (x, y, z)$.

We are now in a position to construct the Bloch transform. From linear algebra, the transformation of a vector from one basis to another is achieved by multiplying the vector by the inverse of the matrix U_{jk} which is the matrix constructed from columns of the eigenstates that make up our new basis. As such, the transformation of a vector $\mathbf{s}_{\mathbf{R}_j}$ representing the spin vectors at each location j into the basis in which the Hamiltonian is diagonalised is represented by

$$\mathbf{s}_{\mathbf{R}_j} = \frac{1}{\sqrt{N}}\sum_{\mathbf{k}}\mathbf{s}_{\mathbf{k}}e^{i\mathbf{k}.\mathbf{R}_j}, \tag{2.2.6}$$

which is our Bloch transform. Its inverse is defined as

$$\mathbf{s}_{\mathbf{k}} = \frac{1}{\sqrt{N}}\sum_{\mathbf{R}_j}\mathbf{s}_{\mathbf{R}_j}e^{-i\mathbf{k}.\mathbf{R}_j}. \tag{2.2.7}$$

The transform is often defined as the following, involving a rescaling of the vector $\mathbf{s}_{\mathbf{k}} \to \sqrt{N}\mathbf{s}_{\mathbf{k}}$:

$$\mathbf{s}_{\mathbf{R}_j} = \sum_{\mathbf{k}} \mathbf{s}_{\mathbf{k}} e^{i\mathbf{k}.\mathbf{R}_j}, \qquad (2.2.8)$$

and it's inverse

$$\mathbf{s}_{\mathbf{k}} = \frac{1}{N} \sum_{\mathbf{R}_j} \mathbf{s}_{\mathbf{R}_j} e^{-i\mathbf{k}.\mathbf{R}_j}. \qquad (2.2.9)$$

This is a more convenient form since most spin configurations are constructed from a single $\mathbf{k}$, or at most 3 $\mathbf{k}$'s. The rescaling gives a one-to-one mapping for the magnitude of the real and reciprocal lattice spin vectors if a single $\mathbf{k}$ is used and as such makes more sense - without this scaling the $\mathbf{s}_{\mathbf{k}}$ vector scales macroscopically with system size.

The overcompleteness of $\mathbf{k}$ discussed previously leads to the construction

$$e^{i\mathbf{k}.\mathbf{R}_j} = e^{i\tilde{\mathbf{k}}.\mathbf{R}_j} \qquad (2.2.10)$$

for certain values of $\tilde{\mathbf{k}}$. Solving this equation we end up with the eigenvector being identical (and hence the transformation being identical) if

$$\tilde{\mathbf{k}} = \mathbf{k} + \mathbf{G}, \qquad (2.2.11)$$

where $\mathbf{G}$ satisfies the condition

$$e^{i\mathbf{G}.\mathbf{R}_j} = 1 \qquad \forall j, \qquad (2.2.12)$$

the condition satisfied by a Bloch wave. As such, there exist what we term 'equivalent' $\mathbf{k}$'s, defined since any $\mathbf{k}$'s that are separated by a reciprocal lattice vector correspond to identical spin configurations in real space. As such, we represent the

$\mathbf{k}$'s in reciprocal space, which is in turn generated from the direct lattice, and restrict attention to solely the first Brillouin zone.

2.3 Reciprocal Space

The conjugate basis to real space, reciprocal space, is generated from primitive reciprocal lattice vectors, $\mathbf{G}_1$, $\mathbf{G}_2$ and $\mathbf{G}_3$, which we now detail. They are constructed such that they satisfy $\mathbf{R}_i.\mathbf{G}_j = \delta_{i,j}2\pi$, where $\mathbf{R}_i$ are primitive real space lattice vectors, so that they belong to the reciprocal lattice, and are given by cyclic permutations of the following:

$$\mathbf{G}_\alpha = 2\pi \frac{\mathbf{R}_\beta \times \mathbf{R}_\gamma}{\mathbf{R}_\alpha.\mathbf{R}_\beta \times \mathbf{R}_\gamma}. \tag{2.3.1}$$

These vectors are permitted to be primitive vectors, that is they define a general reciprocal lattice vector $\mathbf{G}$ as:

$$\mathbf{G} = m_1\mathbf{G}_1 + m_2\mathbf{G}_2 + m_3\mathbf{G}_3, \tag{2.3.2}$$

where m_1, m_2, m_3 are integer values, since (a) they are linearly independent, which can be seen from

$$\mathbf{G}_1.\mathbf{G}_2 \times \mathbf{G}_3 = \frac{(2\pi)^3}{\mathbf{R}_1.\mathbf{R}_2 \times \mathbf{R}_3} \tag{2.3.3}$$

and (b) the m_i are necessarily integer values, from

$$e^{2\pi m_i} = 1, \tag{2.3.4}$$

where the real space vector $\mathbf{R}$ is defined with respect to the primitive real space lattice vectors

$$\mathbf{R} = x_1\mathbf{R}_1 + x_2\mathbf{R}_2 + x_3\mathbf{R}_3, \tag{2.3.5}$$

where x_i are integer values.

We define the range of $\mathbf{k}$ within which we have inequivalent $\mathbf{k}$ points as the Brillouin zone, and the first Brillouin zone is that which contains the $\mathbf{k} = 0$ point. The Brillouin zone can be constructed by taking the perpendicular bisectors of the reciprocal lattice vectors.

2.4 Identities

Several identities are used in conjunction with the Bloch transform in order to determine spin configurations, and we detail them here. We simply state our first identity which is a consequence of spins being real:

$$\mathbf{s}_\mathbf{k}^* = \mathbf{s}_{-\mathbf{k}}. \tag{2.4.1}$$

Our second identity is the following:

$$\sum_{j=1}^{N} e^{i\mathbf{k}.\mathbf{R}_j} = N \sum_{\mathbf{G}} \delta_{\mathbf{k},\mathbf{G}}, \tag{2.4.2}$$

which is valid for any bravais lattice, where N is the total number of sites in the system.

We begin the proof by defining an N'th root of unity, $\bar{\omega}$,

$$\bar{\omega}^N - 1 = 0. \tag{2.4.3}$$

One can consider writing this expression in terms of a summation:

$$0 = (\bar{\omega} - 1)\left(1 + \bar{\omega} + \bar{\omega}^2 + .. + \bar{\omega}^{N-1}\right) \tag{2.4.4}$$

such that $\bar{\omega}$ can either be equal to 1, or defined to satisfy

$$\sum_{p=0}^{N-1} \bar{\omega}^p = 0, \tag{2.4.5}$$

where p are integers. The second expression can be redefined with respect to the sum as

$$\sum_{p=1}^{N} \bar{\omega}^p = 0 \tag{2.4.6}$$

due to the periodic nature of roots of unity, and therefore both possibilities for $\bar{\omega}$ can be encapsulated with the expression

$$\sum_{p=1}^{N} \bar{\omega}^p = N\delta_{\bar{\omega},1}. \tag{2.4.7}$$

To apply this identity to our Bloch phase, we split the phase into the different translational symmetry components present in the system via expansion of the position vector $\mathbf{R}_j$ in terms of its primitive lattice vectors:

$$\sum_{j=1}^{N} e^{i\mathbf{k}.\mathbf{R}_j} = \sum_{a_1=1}^{N_1} e^{i\mathbf{k}.a_1\mathbf{R}_1} \sum_{a_2=1}^{N_2} e^{i\mathbf{k}.a_2\mathbf{R}_2} \sum_{a_3=1}^{N_3} e^{i\mathbf{k}.a_3\mathbf{R}_3} \tag{2.4.8}$$

and consider each summation component separately, where a_l are integers, $\mathbf{R}_l$

19

label the primitive vector directions in which the system possesses translational symmetry and N_l are the number of atoms the system possesses along each of the $\mathbf{R}_l$ directions.

Equating the single term $\sum_{a_1=1}^{N_1} e^{i\mathbf{k}.a_1\mathbf{R}_1}$ with identity 2.4.7 is valid *only if* $\exp^{i\mathbf{k}.\mathbf{R}_1}$ is a root of unity. To determine when this is true, we expand the vector $\mathbf{k}$ in terms of the primitive reciprocal lattice vectors:

$$\mathbf{k} = k_1\mathbf{G}_1 + k_2\mathbf{G}_2 + k_3\mathbf{G}_3. \tag{2.4.9}$$

Given that $\mathbf{R}_i.\mathbf{G}_j = 2\pi\delta_{i,j}$, the root of unity requirement may be expressed as

$$\left(e^{i\mathbf{k}.\mathbf{R}_1}\right)^{N_1} = \left(e^{i2\pi k_1 n_1}\right)^{N_1} = 1 \tag{2.4.10}$$

and hence we see that $k_1 N_1$ must equal an integer, r_1. As such, the term may be expressed as

$$\sum_{a_1=1}^{N_1} e^{i\mathbf{k}.a_1\mathbf{R}_1} = N_1 \delta_{e^{i\mathbf{k}.\mathbf{R}_1},1}$$
$$= \sum_{r_1} \delta_{k_1,r_1}. \tag{2.4.11}$$

Performing the same procedure on the other terms completes the proof:

$$\sum_{j=1}^{N} e^{i\mathbf{k}.\mathbf{R}_j} = N \sum_{r_1,r_2,r_3} \delta_{k_1,r_1}\delta_{k_2,r_2}\delta_{k_3,r_3}$$
$$= \sum_{\mathbf{G}} \delta_{\mathbf{k},\mathbf{G}}. \tag{2.4.12}$$

2.5   Constraints

In solving our spin Hamiltonian, we must adhere to the constraint on the length of each spin, which in real space is given by

$$\mathbf{s}_j.\mathbf{s}_j = S^2 \tag{2.5.1}$$

for ALL lattice points j. We transform this constraint into reciprocal space to obtain a form that we can exploit in determining the minimum energy spin config-uration, as detailed in the next section. We shall show in the following derivation that this leads to the constraints in reciprocal space being

$$\sum_k \mathbf{s}_k.\mathbf{s}_k^* = S^2 \quad \text{if q=0} \tag{2.5.2}$$

$$\sum_k \mathbf{s}_k.\mathbf{s}_{k+q-G} = 0 \quad \text{if } q \neq 0. \tag{2.5.3}$$

Multiplying eq.2.5.1 by $\frac{1}{N}e^{i\mathbf{q}.\mathbf{R}_j}$, where $\mathbf{q}$ is an arbitrary translation in reciprocal space, summing over all j and implementing eq. 2.4.2 gives

$$\frac{1}{N}\sum_j \mathbf{S}_j.\mathbf{S}_j e^{i\mathbf{q}.\mathbf{R}_j} = \frac{1}{N}S^2 \sum_j e^{i\mathbf{q}.\mathbf{R}_j}$$
$$= S^2 \sum_{\mathbf{G}} \delta_{\mathbf{q},\mathbf{G}}. \tag{2.5.4}$$

We now apply a Bloch transform to the left-hand side to obtain

$$\frac{1}{N}\sum_j \sum_{\mathbf{k}} \sum_{\mathbf{k}'} \mathbf{S}_{\mathbf{k}}.\mathbf{S}_{\mathbf{k}'} e^{i\mathbf{k}.\mathbf{R}_j} e^{i\mathbf{k}'.\mathbf{R}_j} e^{i\mathbf{q}.\mathbf{R}_j} \tag{2.5.5}$$

$$= \frac{1}{N} \sum_{\mathbf{k},\mathbf{k}'} \mathbf{S_k}.\mathbf{S_{k'}} \sum_j e^{i(\mathbf{k}+\mathbf{k}'+\mathbf{q}).\mathbf{R}_j}. \qquad (2.5.6)$$

.

Applying eq. 2.4.2 to expression 2.5.6 we obtain

$$\sum_{\mathbf{k}} \sum_{\mathbf{G}} \mathbf{S_k}.\mathbf{S_{G-k-q}}. \qquad (2.5.7)$$

Given that the inverse Bloch transform of $-\mathbf{k}$ can be written as

$$\mathbf{S_{-k}} = \frac{1}{N} \sum_j \mathbf{S}_j e^{i\mathbf{k}.\mathbf{R}_j} = \mathbf{S_k^*}, \qquad (2.5.8)$$

we arrive at the following expression for the real-spins constraint transformed into reciprocal space

$$\sum_{\mathbf{k}} \sum_{\mathbf{G}} \mathbf{S_k}.\mathbf{S_{k+q-G}^*} = S^2 \sum_{\mathbf{G}} \delta_{\mathbf{q},\mathbf{G}}. \qquad (2.5.9)$$

This leads to 2 constraints on the spins in reciprocal space:

$$\sum_{\mathbf{k}} \mathbf{S_k}.\mathbf{S_k^*} = S^2 \quad \text{if } \mathbf{q} = \mathbf{G}, \qquad (2.5.10)$$

$$\sum_{\mathbf{k}} \mathbf{S_k}.\mathbf{S_{k+q-G}^*} = 0 \quad \text{if } \mathbf{q} \neq \mathbf{G}. \qquad (2.5.11)$$

Hence, if $\mathbf{k}_{min}$ are a reciprocal lattice vector apart, then they contribute to the sum of eq.2.5.10. Else, they contribute to the sum of eq.2.5.11. Examples of the

application of these constraints will be shown in calculations of magnetic ground states in the following sections.

2.6 Minimisation Procedure

Now that we have a method of transforming our real space problem into one that diagonalises our Hamiltonian along with the constraints, we can develop a method to determine the minimum energy solution to our spin Hamiltonian. The procedure is performed in the reciprocal space basis where the Hamiltonian is diagonalised and therefore where it is easy to determine which state corresponds to the minimum energy solution.

In the following sections, we will find that the minimum energy spin configuration is given by putting the spin density down only at the $\mathbf{s_k}$'s that correspond to $\mathbf{k}$'s that minimise a quantity called the structure factor. We label these particular $\mathbf{k}$'s as the $\mathbf{k}_{min}$. Furthermore, we detail how to deal with systems where we have degenerate $\mathbf{k}_{min}$, and also show that in some cases both $\mathbf{k}_{min}$ and $-\mathbf{k}_{min}$ must be used in order to ensure reality with respect to the spins in real space.

We begin by representing the Heisenberg energy of the spin system in reciprocal space by performing our previously-defined Bloch transform on the system. The point group symmetry of the lattice system, being the group of rotations and inversions that keep the lattice invariant, is exploited in writing the expression for the Hamiltonian. We therefore define the Hamiltonian as

$$H = \sum_n \frac{J_n}{2} \sum_{<j,j'>_n} \mathbf{S}_j.\mathbf{S}_{j'}, \qquad (2.6.1)$$

where n defines each set of points on the real space lattice that are generated by the point group from a point j_n, with $< j, j' >_n$ indicating the sum is performed over all j'_n generated from j_n. The notation n is alternatively often referred to as describing the nth nearest neighbours of the lattice, with $< j, j' >_n$ therefore

describing how the sum is performed over all j and j' that are nth nearest neighbours. J_n is the antiferromagnetic coupling between nth nearest neighbours. The factor of a half takes care of double-counting with respect to the summation over all nearest neighbours.

Applying the Bloch transform to eq. 2.6.1 we obtain

$$H = \sum_n \frac{J_n}{2} \sum_{<j,j'>_n} \sum_{\mathbf{k}} e^{i\mathbf{k}.\mathbf{R}_j} \mathbf{S}_{\mathbf{k}}. \sum_{\mathbf{k'}} e^{i\mathbf{k'}.\mathbf{R}'_j} \mathbf{S}_{\mathbf{k'}}, \tag{2.6.2}$$

which can be re-arranged as

$$H = \sum_n \frac{J_n}{2} \sum_{\mathbf{k},\mathbf{k'}} \mathbf{S}_{\mathbf{k}}.\mathbf{S}_{\mathbf{k'}} \sum_j e^{i\mathbf{R}_j.(\mathbf{k}+\mathbf{k'})} \sum_{\mathbf{m}_n} e^{i\mathbf{k'}.\mathbf{R}_{\mathbf{m}_n}}, \tag{2.6.3}$$

where $\mathbf{m}_n$ are vectors $(\mathbf{R}_j - \mathbf{R}_{j'})$ for nth nearest neighbours. Using our identity

$$\sum_j e^{i(\mathbf{k}+\mathbf{k'}).\mathbf{R}_j} = N\delta_{\mathbf{k}+\mathbf{k'},\mathbf{G}}, \tag{2.6.4}$$

we arrive at

$$H = \frac{N}{2} \sum_{\mathbf{k}} \mathbf{S}_{\mathbf{k}}.\mathbf{S}_{-\mathbf{k}} \sum_n J_n \sum_{\mathbf{m}_n} e^{i\mathbf{k}.\mathbf{R}_{\mathbf{m}_n}}. \tag{2.6.5}$$

The structure factor[1] is defined as

$$\gamma_{\mathbf{k}} = \sum_n J_n \sum_{\mathbf{m}_n} e^{i\mathbf{k}.\mathbf{R}_{\mathbf{m}_n}} \tag{2.6.6}$$

and so we can write the Hamiltonian in the simple form of

---

[1]The convention is to define the structure factor as $z\gamma_{\mathbf{k}}$ such that the structure factor is normalised between -1 and 1

$$H = \frac{N}{2} \sum_{\mathbf{k}} \mathbf{S}_{\mathbf{k}}.\mathbf{S}_{\mathbf{k}}^{*} \gamma_{\mathbf{k}}. \tag{2.6.7}$$

.

It is useful at this stage to note that the Hamiltonian in the reciprocal space basis obeys the same point group symmetry as that in real space. As such, if one can rotate the real space lattice such that the Hamiltonian remains invariant, then performing this particular rotation in reciprocal space leaves the Hamiltonian invariant too and hence provides other $\mathbf{k}$ that give the same value of $\gamma_{\mathbf{k}}$. To demonstrate this property, we consider acting a rotation $\hat{U}$, which is a unitary operator, on the lattice site locations $\mathbf{R}_j$ to obtain $\mathbf{s}_{\hat{U}\mathbf{R}_j}$ and determine what happens to the Bloch-transformed spins:

$$\mathbf{s}_{\hat{U}\mathbf{R}_j} = \frac{1}{\sqrt{N}} \sum_{\mathbf{k}} \mathbf{s}_{\mathbf{k}} \exp^{i\mathbf{k}.\hat{U}\mathbf{R}_j}. \tag{2.6.8}$$

Using the definition of a unitary operator in terms of the scalar product, and introducing the vector $\mathbf{q} = \hat{U}^{\dagger}\mathbf{k}$, we obtain

$$\mathbf{s}_{\hat{U}\mathbf{R}_j} = \frac{1}{\sqrt{N}} \sum_{\mathbf{q}} \mathbf{s}_{\hat{U}\mathbf{q}} \exp^{i\mathbf{q}.\mathbf{R}_j}, \tag{2.6.9}$$

which corresponds to the spin density being put down at $\hat{U}\mathbf{k}$ rather than the pre-rotation $\mathbf{k}$.

Now that we have an expression for our Heisenberg energy in reciprocal space, we return to the aim of our procedure; we wish to minimise the energy of the spin system, subject to the spin length remaining a fixed length in real space. We define the problem as determining the minimum energy solution to the following

reciprocal-space expression:

$$E = \frac{\sum_{\mathbf{k}} \mathbf{s_k} . \mathbf{s_{k^*}} \gamma_{\mathbf{k}}}{\sum_{\mathbf{k}} \mathbf{s_k} . \mathbf{s_{k^*}}} \qquad (2.6.10)$$

whereby the first constraint in reciprocal space, eq. 2.5.10, is included as the normalisation factor. The second constraint, 2.5.11, will be applied later. To determine the vector field $\mathbf{s_k}$ that minimises the expression, we first express the vector field instead as a vector $\mathbf{a}$ that includes all degrees of freedom:

$$\mathbf{a} = (a_{k_1}^{\alpha_1}, a_{k_1}^{\alpha_2}, a_{k_1}^{\alpha_3}, a_{k_2}^{\alpha_1}, ..., a_{k_N}^{\alpha_3}) \qquad (2.6.11)$$

where $\alpha = (\alpha_1, \alpha_2, \alpha_3)$ labels the Cartesian components (x, y, z) of the spin vector in spin space and the set k label all available reciprocal space positions $\mathbf{k}$. We differentiate the expression for E with respect to each of degree of freedom present in the expression for E, requiring the differential equal zero for *every* degree. Given that we are in the reciprocal space basis in which the Hamiltonian is diagonal in $\mathbf{k}$, and that, in addition to this independence of the k components, the energy consists of scalar product interaction between the spin space vectors and hence only couples the elements of a of identical α labels, the expression simplifies to

$$E = \frac{\sum_k \sum_\alpha (a_k^\alpha)^* (a_k^\alpha) \gamma_k}{\sum_k \sum_\alpha (a_k^\alpha)^* (a_k^\alpha)}. \qquad (2.6.12)$$

Differentiating with respect to each component a_l of a, and the corresponding complex conjugates present in 2.6.12, leads to two expressions for the turning points of the energy[2]:

---

[2]We assume $\mathbf{a}$ and $\mathbf{a}^*$ are independent and end up with two equations related to each other as is expected

$$E(a_q^\alpha)* = \gamma_q(a_k^\alpha)^* \qquad (2.6.13)$$

and

$$E(a_q^\alpha) = \gamma_q(a_k^\alpha) \qquad (2.6.14)$$

that must be obeyed for *all l*. For each l, there are two possible solutions to the equations; either

$$E \neq \gamma_q \quad \text{then} \quad (a_q^\alpha) = 0 \quad \text{for all } \alpha \qquad (2.6.15)$$

or

$$E = \gamma_q \quad \text{then} \quad (a_q^\alpha) = \tau_\nu \quad \text{for all } \alpha_\nu, \qquad (2.6.16)$$

where the τ_ν are not as yet defined in magnitude and are also unrelated to each other at present. As such, we find that for $E = \gamma_q$, a turning point energy, $\mathbf{a}_{turn}$, consists of non-zero elements only at a_q^α *unless* there is a degeneracy in energy. If this degeneracy exists, then there exist k's such that $\gamma_k = \gamma_q$, in which case the elements a_k^α may be non-zero, resulting in a multiple-q spin configuration.

Returning to the original representation of our spin state, the minimum energy state $\mathbf{s_k}$ therefore corresponds to any state that consists of spin space vectors $\mathbf{s}$ that are non-zero only at reciprocal space locations $\mathbf{k}$ that correspond to the minimum value of the structure factor $\gamma_\mathbf{k}$. In other words, the minimum energy state corresponds to the eigenvector of the Hamiltonian that corresponds to the minimum eigenvalue. From now on we shall refer to the $\mathbf{k}$ that minimises the structure factor

as $\mathbf{k}_{min}$. The final step in the minimisation procedure is the assignment of these non-zero spin space vectors such that they adhere to the second constraint on spin length, 2.5.11. This is easily performed since only those spin densities $\mathbf{s_k}$ corresponding to $\mathbf{k} = \mathbf{k}_{min}$ exist. The choice of which of the *potentially* non-zero spin vectors to assign as non-zero however requires some further thought.

The use of more than one $\mathbf{s_{k}}_{min}$ encompasses the spin configurations of multiple-q magnetism present in real systems. Additionally, in certain cases, more than one spin space vector $\mathbf{s_{k}}_{min}$ must be non-zero in order to ensure the real space spins are real, as is the case for spin spirals. Specifically, for cases in which $\mathbf{s_{k}}_{min}$ is complex, which occurs for any system that breaks the inversion symmetry of the lattice, leading to $\mathbf{k} \neq -\mathbf{k}$ (from identity 2.4.1), the real space spin must be constructed from an $\mathbf{s_{k}}_{min}$ *and* its complex conjugate. The result simplifies nicely according to identity 2.4.1 and as such, the real spin $\mathbf{s}_j$ can be written as

$$\mathbf{s}_j = \mathbf{s_k}e^{i\mathbf{k}.\mathbf{R}_j} + \mathbf{s_{-k}}e^{i\text{-}\mathbf{k}.\mathbf{R}_j}. \qquad (2.6.17)$$

This requirement comes about from the inversion symmetry present in the spin system. Any system whose $\mathbf{k}_{min}$ do not lie mid-way between reciprocal lattice points requires this construction.

Finally we mention the shortfalls of this procedure. In most cases, the procedure we have described is sufficient to obtain the solution to the problem subject to both our constraints. *However*, this is not always the case, as in some systems the second constraint cannot be satisfied using the $\mathbf{k}_{min}$. This is true for some cases in which there is more than 1 atom per unit cell.

Chapter 3

FRUSTRATION AND DEGENERACY

We now introduce the concept of frustration that leads to degeneracy in the spin ground states and hence to interesting behaviour at surfaces. This leads us to classify different types of magnets according to the spin state degeneracies they possess in the ground state. We then determine the spin configurations of different types of systems in order to demonstrate these different classes. The last section of the chapter is concerned with multiple-q magnets and in particular those associated with the FCC lattice, the focus of my research.

3.1 Frustration and degeneracy

A system is said to be frustrated if it possesses interactions such that no spin state exists whereby all bonds can be completely satisfied simultaneously. The common example is that of a 3 spin problem whereby the spins have a triangular formation and equal interactions between each site, as shown in fig 3.1. There is no direction that the third spin can point in and satisfy all bonds simultaneously. Frustration can be achieved in two different ways: via competing interactions, or geometric frustration. Examples of frustration brought on by competing interactions include the 1D chain of atoms that possesses both nearest neighbour and second nearest neighbour interactions, and the 2D frustrated square lattice again with both nearest and second nearest neighbour coupling that we shall be tackling shortly. Geometrical
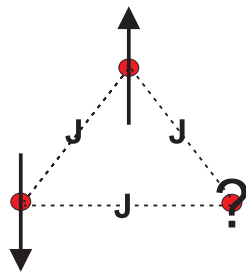
Figure 3.1: *Example of a frustrated system*

frustration occurs as a result of the lattice being based in triangular or tetrahedral units, for example the triangular, hexagonal close packed or pyrochlore lattice. The face centred cubic lattice possess tetrahedral units and we will be analysing the frustration later on.

Frustration is required for a magnetic spin state to 'care' about a surface. For the state to prefer to reorient or reconstruct, there must be a larger proportion of frustration parallel to the surface in comparison with perpendicular to it. In this way, it becomes possible for the system to gain back more energy by using a different spin configuration of different symmetry, for which there is a better ratio of frustration with respect to the perpendicular and parallel directions. Thus, when bonds are broken by the introduction of the surface, some of the frustration is lost by using the alternative state and energy can therefore be gained by reorienting or reconstructing to this state.

3.2 Classification of Magnets

Magnets can be classified into different styles according to the types of degeneracy their ground states possess. The term degeneracy is used to describe degeneracy between state with different point-group symmetries, as opposed to the trivial degeneracy describing states connected simply by a global spin rotation with no associated change in symmetry. The degeneracy shows up as spin states related by point-group symmetries of the Hamiltonian. We must be more specific however in

what we mean by this, as the Heisenberg Hamiltonian possesses invariance with respect to operations on the spins in spin space as well as operations solely concerned with the lattice. It is the second of these two types of operations that lead to different translational symmetries and are the symmetries we are interested in. As such, when we refer to the point group symmetries of the Hamiltonian, we refer to those relating to the lattice or lattice-plus-spin-space operations, and *not* solely to the global rotations of spins in spin space. We remind the reader that, as was shown in section 2.6, rotations of this type act on the $\mathbf{k}$'s in reciprocal space in exactly the same way as in real space. Thus, studying the problem in reciprocal space eliminates confusion associated with the extra space of the spin vectors, and as such we shall be classifying magnets by studying the problem in reciprocal space. Specifically, we classify magnets in terms of the number of $\mathbf{k}_{min}$'s and their relation to one another, as this indicates the number and type of appropriate degeneracies the system possesses in the ground state.

The simplest class is one in which the system occupies a single $\mathbf{k}_{min}$ that maps onto itself under all point-symmetries of the Hamiltonian. Ferromagnetism ($\mathbf{k} = 0$) and bipartite antiferromagnetism are examples of this class of magnet. The second simplest involves two $\mathbf{k}_{min}$ points that are related by inversion symmetry. As a result of eq. 2.4.1, the spin density vectors $\mathbf{S_k}$ and $\mathbf{S_{-k}}$ are constrained to be complex conjugates of each other, and as such the magnitude of the spin density put on each $\mathbf{k}$ must be identical. The resulting magnet in real space is a spin spiral, with 2-fold degeneracy associated with left or right-handed chirality.

The final class is that of multiple-q magnets, which encompasses magnets that have more than one distinct $\mathbf{k}_{min}$ and which are related by the rotational symmetry group of the Hamiltonian. Within this class there are 1-q, 2-q and 3-q multiple-q magnets that have simultaneously 1, 2 or 3 styles of long-range order, associated with putting the spin density down at more than one location in reciprocal space, and we have continuous degeneracy. Anisotropy and effects such as quantum fluctuations or
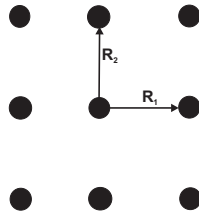
Figure 3.2: *Real space lattice vectors for the 2D square lattice.*

inclusion of impurities in the system breaks the degeneracy associated with how the spin density is split between the different $\mathbf{k}_{min}$ and we shall discuss this in section 3.3.

We now proceed to determine the ground state magnetic configurations of a few systems as examples of the different classes of magnets, using the theory developed in the preceeding sections.

3.2.1 The 2D Nearest Neighbour Square Lattice

Our first example involves a system which has a single distinct $\mathbf{k}_{min}$, remaining invariant under the action of all the point symmetries of the Hamiltonian. We are to use a 2D square lattice modelled with an antiferromagnetic Heisenberg Hamiltonian (i.e. where $J_n > 0$), with only nearest neighbour interactions, J, included.

The real space lattice vectors are defined as in figure (3.2) and given by

$$\mathbf{R}_1 = (1, 0)$$
$$\mathbf{R}_2 = (0, 1). \tag{3.2.1}$$

The structure factor $\gamma_{\mathbf{k}}$ is hence given by

$$\gamma_{\mathbf{k}} = J \sum_m e^{i\mathbf{k}.\mathbf{R}_m}$$
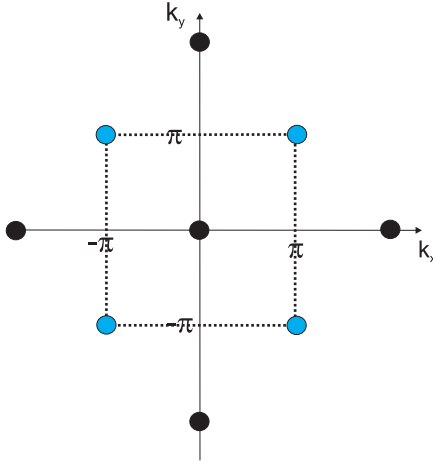
Figure 3.3: $\boldsymbol{k}_{min}$ for the square lattice modelled with a Heisenberg Hamiltonian with nearest neighbour coupling. The $\boldsymbol{k}_{min}$ are shown as blue spots, black spots are the reciprocal lattice points and the dotted line indicates the location of the first Brillouin zone boundary.

$$= 2J[cos(k_x) + \cos(k_y)]. \tag{3.2.2}$$

$\mathbf{k}_{min} = (\pi, \pi)$ minimises the structure factor expression. We implement the point group symmetries of H in real space in the reciprocal space to generate other $\mathbf{k}_{min}$ from (π, π), namely using $\frac{\pi}{2}$ rotations. The resulting full set of $\mathbf{k}_{min}$ is shown in fig.(3.8). The primitive reciprocal lattice vectors, $\mathbf{G}_1$ and $\mathbf{G}_2$ are constructed using eq.2.3.1 and are found to be

$$\mathbf{G}_1 = (2\pi, 0)$$
$$\mathbf{G}_2 = (0, 2\pi). \tag{3.2.3}$$

The primitive vectors are then implemented to determine which $\mathbf{k}_{min}$ are distinct, and we find that π, π describes the only distinct vector that exists.

The reciprocal lattice constraints are now implemented. Only eq. 2.5.10 is nontrivial in this case and simply gives
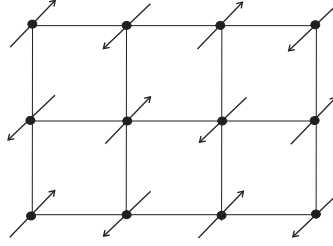
Figure 3.4: *Real space spin configuration for the 2D square lattice.*

$$\mathbf{S}_{(\pi,\pi)}.\mathbf{S}^*_{(\pi,\pi)} = S^2, \tag{3.2.4}$$

the simple result of which is that the length of the spin is fixed in reciprocal space and no other constraint on the spin vector $\mathbf{S_k}$ is present. As a result, the corresponding real space configuration, obtained by performing an inverse Bloch transform, is described by

$$\mathbf{S_{R_j}} = \sum_{\mathbf{k}} e^{i\mathbf{k}.\mathbf{R}_j}\mathbf{S_k} = e^{i\pi R_x}.e^{i\pi R_y}\mathbf{S}_{\pi,\pi}, \tag{3.2.5}$$

where $\mathbf{S}_{\pi,\pi}$ is free to point in any direction in real space. The resulting spin configuration can be seen in figure (3.4) and is an antiferromagnet in its Neél state.

3.2.2 The 2D Triangular Lattice

We next tackle a system whose two distinct $\mathbf{k}_{min}$ are related by inversion symmetry; the 2D nearest neighbour triangular lattice modelled again with an antiferromagnetic Heisenberg Hamiltonian.

The position vectors

$$\mathbf{R}_1 = (1,0)$$
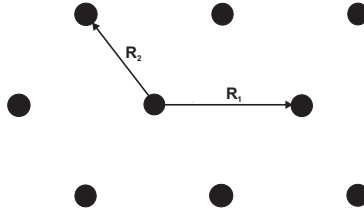
Figure 3.5: *Real space lattice vectors for the 2D triangular lattice.*

$$\mathbf{R}_2 = \left(-\frac{1}{2}, \frac{\sqrt{3}}{2}\right). \tag{3.2.6}$$

as illustrated in fig. 3.5, are used to label the lattice points. The structure factor is hence given by

$$\gamma_{\mathbf{k}} = 2\left[\cos\left(\mathbf{k}.\mathbf{R}_1\right) + \cos\left(\mathbf{k}.\mathbf{R}_2\right) + \cos\left(\mathbf{k}.(\mathbf{R}_1 + \mathbf{R}_2)\right)\right]. \tag{3.2.7}$$

Substituting for $\mathbf{R}_1$ and $\mathbf{R}_2$ and simplifying we obtain

$$\gamma_{\mathbf{k}} = 2\left[\cos\left(k_x\right) + 2\cos\left(\frac{k_x}{2}\right)\cos\left(\frac{\sqrt{3}}{2}k_y\right)\right]. \tag{3.2.8}$$

To minimise the expression we re-write it in a more convenient form by completing the square

$$\gamma_{\mathbf{k}} = 2\left[2\left(\cos\left(\frac{k_x}{2}\right) + \frac{1}{2}\cos\left(\frac{\sqrt{3}}{2}k_y\right)\right)^2 - \frac{1}{2}\cos^2\left(\frac{\sqrt{3}}{2}k_y\right) - 1\right], \tag{3.2.9}$$

and hence obtain some $\mathbf{k}_{min}$:

$$\mathbf{k}_1 = \left(\frac{4\pi}{3}, 0\right)$$

35
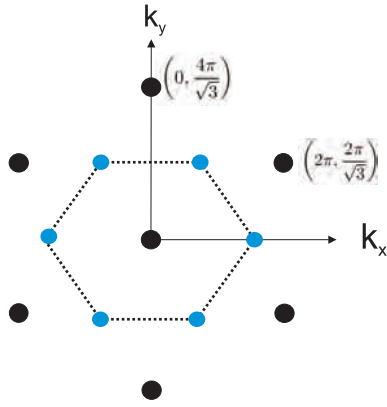
Figure 3.6: $\mathbf{k}_{min}$ *for the triangle lattice modelled using a Heisenberg Hamiltonian with nearest neighbour coupling. The* $\mathbf{k}_{min}$ *are shown as blue spots, black spots are the reciprocal lattice points and the dotted line indicates the location of the first Brillouin zone boundary.*

$$\mathbf{k}_2 = \left(\frac{2\pi}{3}, \frac{2\pi}{\sqrt{3}}\right). \tag{3.2.10}$$

The point group symmetries of the Hamiltonian, of rotations by $\frac{\pi}{6}$, generate all other $\mathbf{k}_{min}$ values, which are shown in figure (3.6).

The reciprocal lattice vectors are calculated to be

$$\mathbf{G}_1 = \left(2\pi, \frac{2\pi}{\sqrt{3}}\right)$$
$$\mathbf{G}_2 = \left(0, \frac{4\pi}{\sqrt{3}}\right). \tag{3.2.11}$$

From inspection of figure (3.6), we can see that there are 2 distinct $\mathbf{k}_{min}$ that are inversion-related[1]

$$\mathbf{k}_1 = \left(\frac{4\pi}{3}, 0\right)$$
$$\mathbf{k}_2 = -\mathbf{k}_1 = \left(\frac{-4\pi}{3}, 0\right). \tag{3.2.12}$$

---

[1]The inversion-relation can be shown by considering that translating $\mathbf{k}_2$ by lattice vector $\mathbf{G}_1$ gives an equivalent $\mathbf{k}$, which in this case is $-\mathbf{k}_1$

Before proceeding with the reciprocal lattice constraints, we note that, by implementing the identity

$$\mathbf{S}_{-\mathbf{k}} = \sum_j e^{-i\mathbf{k}.\mathbf{R}_j} \mathbf{S}_{\mathbf{R}_j} = \mathbf{S}_{\mathbf{k}}^*, \tag{3.2.13}$$

we have that

$$\mathbf{S}_{\mathbf{k}_2} = \mathbf{S}_{-\mathbf{k}_1} = \mathbf{S}_{\mathbf{k}_1}^*. \tag{3.2.14}$$

We now apply the reciprocal lattice constraints. The first constraint, eq.2.5.10, gives

$$2\mathbf{S}_{\mathbf{k}_1}.\mathbf{S}_{\mathbf{k}_1}^* = S^2, \tag{3.2.15}$$

giving that the magnitude of the spin vectors $|\mathbf{S}_{\mathbf{k}_1}| = |\mathbf{S}_{-\mathbf{k}_1}| = \frac{S}{\sqrt{2}}$. The second constraint, eq.2.5.11, gives[2]

$$\mathbf{S}_{\mathbf{k}_1}.\mathbf{S}_{\mathbf{k}_1} = 0$$
$$\mathbf{S}_{-\mathbf{k}_1}.\mathbf{S}_{-\mathbf{k}_1} = 0. \tag{3.2.16}$$

Since the spin space vectors do not have to be real in reciprocal space, we can solve eq.3.2.16 by using complex vectors whose real and imaginary components have identical magnitudes. From eq.3.2.15 the magnitude of the vectors must be $\frac{S}{\sqrt{2}}$ and so we arrive at

---

[2]The two separate equations arise from the fact that the vector $\mathbf{q}$ joining $\mathbf{k}_1$ to $\mathbf{k}_2$ is not the same as that joining $\mathbf{k}_2$ to $\mathbf{k}_1$.

$$\mathbf{S_{k_1}} = \frac{S}{2}(\hat{\mathbf{e}}_1 + i\hat{\mathbf{e}}_2)$$

$$\mathbf{S_{-k_1}} = \mathbf{S_{k_1}^*} = \frac{S}{2}(\hat{\mathbf{e}}_1 - i\hat{\mathbf{e}}_2),$$

$$(3.2.17)$$

where $\hat{\mathbf{e}}_1$ and $\hat{\mathbf{e}}_2$ are orthogonal unit vectors arranged arbitrarily in real space.

We finally transform back into real space, given that $\mathbf{R}_j = n_1\mathbf{R}_1 + n_2\mathbf{R}_2$ where n_1 and n_2 are integers, to obtain

$$
\begin{aligned}
\mathbf{S}_j &= \sum_{\mathbf{k}} e^{i\mathbf{k}.\mathbf{R}_j}\mathbf{S}_j = \mathbf{S_{k_1}}e^{i\mathbf{k}_1.\mathbf{R}_j} + \mathbf{S_{-k_1}}e^{-i\mathbf{k}_1.\mathbf{R}_j} \\
&= S\left[\cos\left(\frac{2\pi}{3}(2n_1 - n_2)\right)\hat{\mathbf{e}}_1 - \sin\left(\frac{2\pi}{3}(2n_1 - n_2)\right)\hat{\mathbf{e}}_2\right] \\
&= S\left[\cos\left(\theta_{n_1,n_2}\right)\hat{\mathbf{e}}_1 + \sin\left(\theta_{n_1,n_2}\right)\hat{\mathbf{e}}_2\right], \qquad (3.2.18)
\end{aligned}
$$

where

$$\theta_{n_1,n_2} = \frac{2\pi}{3}(2n_1 + n_2). \qquad (3.2.19)$$

The spin configuration is shown in figure (3.7). The two degenerate states, which are the right-handed and left-handed chiral states, are accessed by altering the phases of the spin density put at the two spots; the magnitudes remain fixed. This can be contrasted with the accessing of the different degenerate state in multiple-q magnets, which we shall be showing are accessed by instead altering the magnitude of the spin densities at the spots.
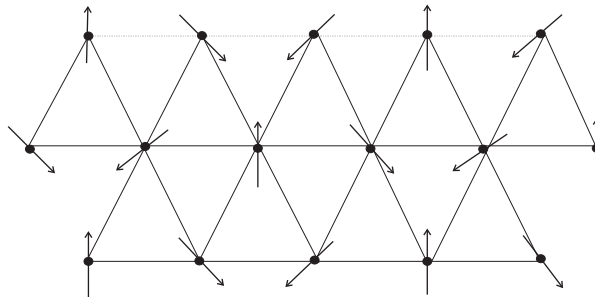
Figure 3.7: *Ground state spin configuration of the 2D triangular lattice modelled using a Heisenberg Hamiltonian with nearest neighbour interactions.*

3.2.3 The 2D Frustrated Square Lattice

We now solve for the ground state spin configuration of a square lattice which contains, via the introduction of a second nearest interaction, frustration. The second nearest neighbour interaction, J_2, in effect serves to split the geometry into triangles, which as we know leads to frustration. As such, the Néel state, which completely solved all bonds in the previous 2D square lattice system studied, is no longer an unfrustrated state and as such is not the ground state for the whole of parameter space. We shall find that the solution is our first example of a multiple-q magnetic state.

In addition to the introduction of J_2, our 2D square lattice is also modified by removing the constraint of all nearest neighbour interactions being identical to each other. Specifically, we allow nearest neighbour interactions that act in directions perpendicular to each other to be unrelated in strength. This adds extra states to our phase space that are differentiated between in terms of their translational symmetry in different directions. This will become useful when we introduce the surface, and so we label the different nearest neighbour interactions with the subscripts $\parallel$ and $\perp$ in anticipation. Our resulting Heisenberg Hamiltonian is described by:

$$H = \frac{J_\parallel}{2} \sum_{<jj'>_\parallel} \mathbf{S}_j.\mathbf{S}_{j'} + \frac{J_\perp}{2} \sum_{<jj'>_\perp} \mathbf{S}_j.\mathbf{S}_{j'} + \frac{J_2}{2} \sum_{<jj'>_2} \mathbf{S}_j.\mathbf{S}_{j'}, \qquad (3.2.20)$$

where $< jj'>_\parallel$ denotes nearest-neighbour bonds parallel to the surface, $< jj'>_\perp$ denotes nearest-neighbour bonds perpendicular to the surface and $< jj'>_2$ denotes second-nearest-neighbour bonds.

The structure factor associated with this Hamiltonian is

$$\gamma_{\mathbf{k}} = 2J_\perp \cos k_x + 2J_\parallel \cos k_y + 4J_2 \cos k_x \cos k_y \qquad (3.2.21)$$
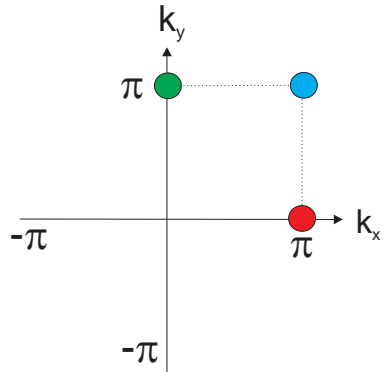
Figure 3.8: *Degenerate, inequivalent $\mathbf{k}_{min}$ for the frustrated square lattice system.*
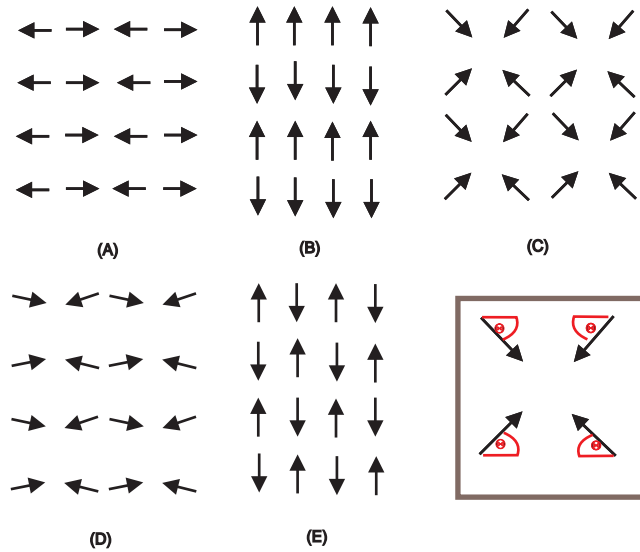
Figure 3.9: *Possible spin orientations of our square lattice antiferromagnet, along with the θ convention used to describe them. We have (a) Single-q (x-oriented) (b) Single-q (y-oriented) (c) Double-q (Equal mixture) (d) Double-q (Unequal mixture) (e) Néel State.*

41
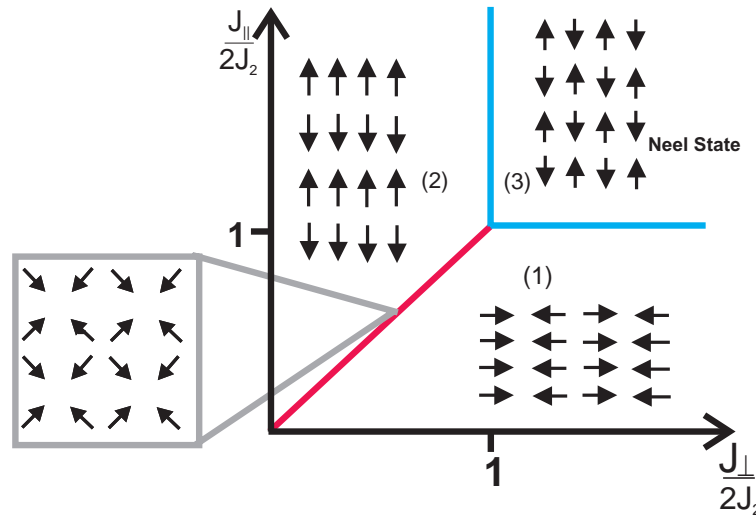
Figure 3.10: *Bulk phase diagram for our square lattice, showing 3 regions containing the 3 single-q states, plus 3 degeneracy lines corresponding to regions of double-q (and a single point of triple-q). Region (1) is $\theta = 0$ and region (2) $\theta = \pi/2$*

and can be miminised simply by inspecting the form obtained by 'completing the square'

$$\gamma_k = 4J_2 \left(\cos k_x + \frac{J_\parallel}{2J_2} \right) \left(\cos_{k_y} + \frac{J_\perp}{2J_2} \right) - \frac{J_\parallel J_\perp}{J_2}. \qquad (3.2.22)$$

.

The inequivalent $\mathbf{k}_{min}$ are shown in fig 3.8 and become active for different values of parameters. The spin arrangements available to our square lattice are pictured in fig. 3.9 and we plot the associated phase diagram with respect to the natural parameters $\frac{J_\parallel}{2J_2}$ and $\frac{J_\perp}{J_2}$ in fig.3.10. The phase diagram involves multiple-q states as we shall now describe.

Notice that the $(0, \pi)$ and $(\pi, 0)$ points are related by the rotational symmetry of the Hamiltonian that is present for the case of $J_\parallel = J_\perp$. This is a property of multiple-q systems; magnetic states map onto other *distinct* magnetic states via a rotational symmetry of the Hamiltonian. As a result, these states are degenerate in energy but possess different translational symmetries and therefore different

magnetic order. As such, there can exist a spin state corresponding to the super-imposition of states that possess different magnetic order. This 'combined' state, whereby the spin density is put down at *two* locations in reciprocal space simultaneously, is termed a double-q state. In three dimensions, a triple-q state can exist, whereby the system has the potential to possess three spin orders simultaneously, and we shall come across this possibility later.

The spin quantisation direction of the states is of course degenerate since global rotations of the spins in spin space leave the Hamiltonian invariant. As such, we choose the spin quantisation direction of each state as illustrated in fig. 3.9, such that we can conveniently describe all available states with respect to an angle θ. The double-q state just described exists on the diagonal phase boundary, and there is freedom to choose the relative strengths of the two spin densities that it is comprised of, subject to the length constraints. These states thereby correspond to θ taking any value in the range $0 \leq \theta \leq \pi/2$. Similarly, the other two phase boundaries correspond to degeneracy between the Néel state and the $\mathbf{k} = (0, \pi)$ or $\mathbf{k} = (\pi, 0)$ magnetic states and hence to other double-q states (although these degeneracies are not between states related by the rotational symmetry of the Hamiltonian). The convention with respect to θ can also be used to describe these states, since the Néel character can be incorporated by using alternate values of the angle on successive parallel layers. This will become useful when a surface is introduced to the system in chapter 6.

3.2.4 FCC Lattices

We now solve for the spin state of the FCC lattice described by the AFM Heisenberg Hamiltonian with nearest neighbour coupling. This lattice possesses geometric frustration since each elementary cell consists of a tetrahedron formed from four triangular plaquettes, as shown in fig. 3.11. We shall find that this frustration leads to multiple-q magnetism, and in particular, we find that, in the absence of anisotropy,
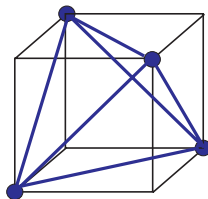
Figure 3.11: *Elementary cell of the FCC lattice, a tetrahedron, which can be considered as being constructed from four triangular plaquettes.*
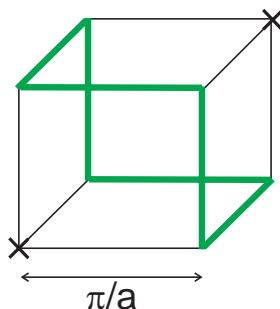
Figure 3.12: $\boldsymbol{k}_{min}$ *for the FCC lattice for the AFM Heisenberg Hamiltonian with nearest neighbour coupling. The cell depicted in reciprocal space is 1/8th of the BCC unit cell. The thick green lines are the $\boldsymbol{k}_{min}$ while the crosses mark the underlying lattice symmetry, being BCC. The real space lattice spacing magnitude is denoted a.*

we obtain *lines* of degenerate $\mathbf{k}_{min}$.

The structure factor for this system is given by $\gamma_{\mathbf{k}} = \cos k_x \cos k_y + \cos k_z (\cos k_x + \cos k_y)$ and the resulting k-points corresponding to minimum energy are shown as thick 'lines of degeneracy' on the reciprocal space lattice in figure 3.2.4, which depicts 1/8th of the body-centred cubic (BCC) reciprocal lattice

The real space spin configuration cannot be constructed using a superposition of points that are located on lines that protrude in different directions. The proof is not trivial, so we merely state this fact and proceed to study a single line to determine the allowed spin configurations of the model. Noting that there is only 1 non-equivalent line in each direction (making use of the reciprocal lattice vector), we focus our attention on the line in the k_z-direction.

Since we are dealing with a line as opposed to a point, we shall describe lines as $\tilde{k} = (k_x, k_y)$, and so in this case, $\tilde{k} = (\pi, 0)$. Since all the points along the

line correspond to degenerate spin configurations[3], one can consider the real space configuration in general terms as being a sum over these points where we may or may not assign an $\mathbf{s}_k$ to each one, the details of which are dictated by the spin length constraints. As such, we can perform a Bloch transform parallel to the z-direction and obtain the expression

$$\mathbf{s}_{(k_x,k_y,n_z)} = \sum_{k_z} e^{ik_z.n_z} \mathbf{s}_{(k_x,k_y,k_z)}. \tag{3.2.23}$$

Given that the ground state configuration is constructed only using spots that correspond to $(k_x, k_y) = (\pi, 0)$, one can Bloch transform parallel to x and y to obtain

$$\mathbf{s}_{(n_x,n_y,n_z)} = e^{i(k_x,k_y).(n_x,n_y)} \mathbf{s}_{(k_x,k_y,n_z)}. \tag{3.2.24}$$

This expression demonstrates that, if we localise to any xy plane, which we label n_z, only a square lattice Néel state is present. This phase in turn leads to a special case where the interaction of a spin with those neighbours in the plane above or/and below has a net value of zero, and as such spins in neighbouring planes are independant of each other.

Due to the presence of these 'degeneracy' lines in all three directions x, y and z, the ground state spin configuration can therefore be constructed from independent planes in the x, y or z direction which have a Néel configuration but whose spin quantization direction is independent from other planes.

3.3   Multiple-q FCC Magnets

The degeneracy of the n.n. FCC ground state spin configuration, present as lines in reciprocal space, is broken in real systems. It has been observed that the degeneracy

---

[3]As such, we shall in future refer to these lines as 'lines of degeneracy'.
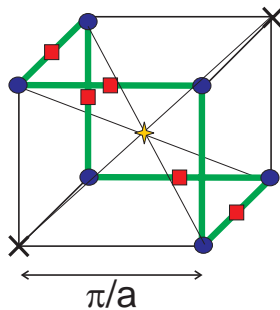
Figure 3.13: $\mathbf{k}_{min}$ for the FCC lattice magnetic types 1,2 and 3. The cell depicted in reciprocal space is 1/8th of the BCC unit cell. The thick green lines are the $\mathbf{k}_{min}$ obtained from the nearest neighbour Heisenberg Hamiltonian, void of anisotropy. Blue spots denote type-1 magnetism, red squares type-3, and the yellow star in the centre of the cell type-2. The crosses mark the underlying lattice symmetry, being BCC. The real space lattice spacing magnitude is denoted a.

can be broken in three different ways, corresponding to 3 standard sets of $\mathbf{k}_{min}$. We shall from now on refer to the $\mathbf{k}_{min}$ as their experimental counterpart Bragg spots. These are measured in reciprocal space and correspond to our $\mathbf{k}_{min}$ vectors. The different sets of Bragg spots are shown in fig. 3.13 and are a result of competing phenomena. Type 1 occurs for systems in which the nearest neighbour interactions are dominant and further neighbours are not significant. Type 3 is stabilised by second nearest neighbor interactions, if the nearest neighbour interactions are still the dominant coupling. Finally, type-2 systems correspond to those for which the second nearest neighbour coupling is dominant over the nearest neighbour interactions.

We shall be studying systems of type 1, whose Bragg spots are located at highly symmetric points and hence this type is the simplest case to study. Specifically, the non-equivalent Bragg spots are located at $\mathbf{k}_1 = (\pi, 0, 0)$, $\mathbf{k}_2 = (\pi, 0, 0)$, $\mathbf{k}_3 = (\pi, 0, 0)$ and the corresponding magnetic states, including multiple-q states, are shown in fig. 3.14. It is possible to access different multiple-q states by moving through parameter space, moving for example from a single-q to another single-q state, or from single-q states to double-q states. One can observe these types of transitions in the phase diagram for Manganese Nickel alloys constructed by Honda *et al* [3], shown in fig. 3.15. The transitions in spin configuration, brought on in this case by the impurity concentration of Ni increasing, result in structural transitions that
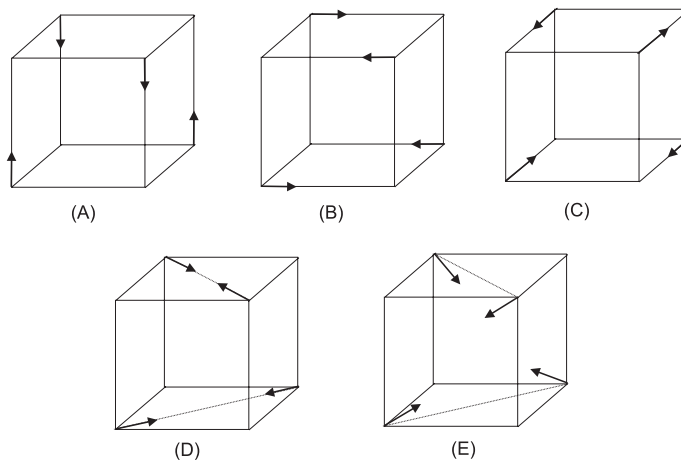
Figure 3.14: *The five distinct types of multiple-q state found in FCC type 1 antiferromagnets. (A)-(C) are single-q, (D) equal mixture double-q and (E) equal mixture triple-q*

effectively alter the magnetic coupling between the spins on the lattice and further stabilise the different states.

The increase in impurity concentration, which results in alloy disorder, serves to stabilise double or triple-q spin configurations over single-q configurations, for reasons that will be visited in the following chapter. Other effects that affect the stability of the different multiple-q states include quantum fluctuations, order from disorder, magnetoelasticity, and itinerancy.

On top of the degeneracy associated with the location and strength of the Bragg spots, there is the additional degeneracy of spin quantisation direction present in Heisenberg models that is broken in real systems via for example spin-orbit coupling. Magnets are thus classed as longitudinal, where the spin quantisation direction follows the direction of the $\mathbf{k}$ vector, and transverse magnets, whereby the spin quantisation direction lies in a plane perpendicular to the $\mathbf{k}$ vector direction. There are two possible domains describing the spin directions for transverse magnets, with the spin directions in the domains being orthogonal to each other. This issue of domain mixture will be covered in the next chapter.

We close this section by exploring the construction of spin configurations from Bragg spot data for our FCC lattice type-1 systems. These systems possess the useful
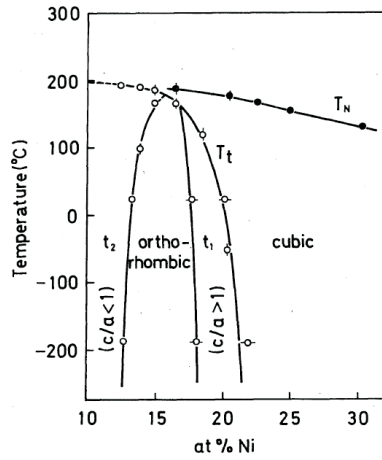
Figure 3.15: *Phase diagram of the γ Mn Ni alloy system, showing structural distortions as a function of Ni concentration and temperature. Both t_1 and t_2 are tetragonal. T_N is the Néel point and T_t the distortion temperature [4]. The structural distortions can be associated with transitions between different magnetic states*

property of the spots obeying the condition $\mathbf{k} = \mathbf{-k}$. From demanding that the spins in real space be real such that $(\mathbf{s_k})^* = \mathbf{s_{-k}}$, and simultaneously demanding that the length of the real space spin be constrained, one can determine, using the reciprocal space constraints of (2.5.10) and (2.5.11), that the $\mathbf{s_k}$ used to construct the real space spin are all directed orthogonally to each other. Moreover, the constraints also force the sum of the squares of the magnitudes of each $\mathbf{s_k}$ vector to be equal to the square of the total spin length in real space. As such, one can represent the $\mathbf{s_k}$'s in polar coordinates as

$$
\begin{aligned}
\mathbf{S_{k_1}} &= \hat{\mathbf{e}}_1 S \sin\left(\theta\right) \cos\left(\phi\right) \\
\mathbf{S_{k_2}} &= \hat{\mathbf{e}}_2 S \sin\left(\theta\right) \sin\left(\phi\right) \\
\mathbf{S_{k_3}} &= \hat{\mathbf{e}}_3 S \cos\left(\theta\right),
\end{aligned}
\tag{3.3.1}
$$

and the construction hence becomes trivial.

Now that we have introduced the FCC lattice and its spin configuration in its bulk form, we have the tools to proceed with our goal of determining how the spin

48

configuration of a FCC lattice may be altered when a surface is introduced. However before we tackle the two main studies of this thesis, we first give an overview of the field of multiple-q magnets, focussing on the domain structures, effects that stabilise the different multiple-q states and phase transitions between them.

Chapter 4

PHENOMENA ASSOCIATED WITH

MULTIPLE-Q MAGNETS

The motivation behind this chapter is to introduce properties of multiple-q magnets that are central to the requirements of the reconstruction phenomenon, and also aid in the modelling of uranium dioxide and the reorientational spin configuration. We begin by discussing the mixture of domains present in multiple-q systems which allows a description of the different types of degeneracy present in real magnets and offers validity to real systems possessing states in the bulk that would reconstruct towards the surface.

Effects that stabilise the different multiple-q states are then discussed to aid the modelling of different systems and will be used to understand the main effects at work in uranium dioxide and also any effects that would stabilise or hinder reconstruction so that appropriate materials can then be determined that have the potential to show reconstruction at the surface.

Finally, a case study of the phase transitions observed in γ-Mn Ni alloys is presented. The study demonstrates how a system can go through a series of spin reorientation transitions between different multiple-q states and how magnetoelastic coupling then results in structural distortions that respect the symmetry of the magnetic states, further stabilising them in the domain mixture. The origin of this magnetoelastic coupling is discussed briefly.

4.1 Domains and Magnetoelastic Distortions

We begin this chapter with a discussion of domains as applied to multiple-q magnets. Multiple-q magnets are special in that additional domains are present in the domain mixture and as such the possibility of a different type of domain wall exists. These walls are called T-domains and are the relevant walls to consider in our surface reorientation and reconstruction phenomena.

Magnetic domain mixtures exist in real systems due to effects such as stacking faults, dislocations, grain boundaries and crystallographic twins. It is the bulk rather than surface that controls the domain distribution. This point will become important for our surface reconstruction phenomenon later. A description of the domain mixtures present in multiple-q systems will now be explored with the aid of experiments performed on NiO. [3][15][16][17].

The magnetic spins of antiferromagnetic NiO are frustrated, residing on a FCC lattice. The spin states are type-3 due to stronger second nearest than nearest neighbour coupling. According to neutron scattering measurements obtained in the 60's [15], there are either 1 *or* two distinct Bragg spots. The complication in distinguishing multi-single-q domains and double or triple-q magnets arises from the fact that both types of system possess identical Bragg spots. For the case of a single-q magnet, within a reciprocal space description each star of **k** wave vector corresponds to a single K domain [18]. For a double or triple-q magnet however, some or all of these star of **k** contribute to the single type of domain of the double or triple-magnet. Magnetic neutron scattering experiments, and indeed any experiments that are global probes that rely on interference of the probe over the entire crystal, provide Bragg spots at the star of **k** wavevectors. As such, distinguishing between a mixture of single-q domains and a magnet of double or triple-q spin structure is generally not possible by analysing Bragg peaks. Furthermore, whilst experimenting on a single-domain crystal would solve this issue, producing these crystals via for example
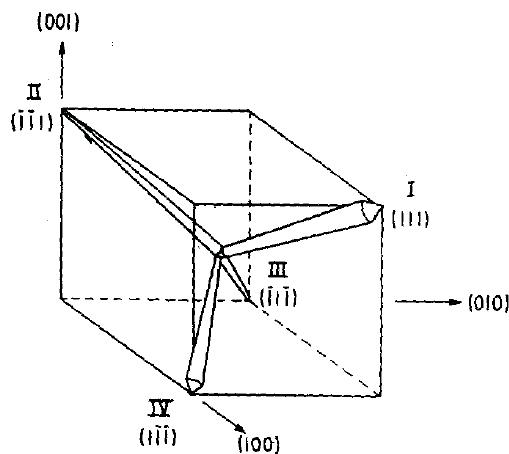
Figure 4.1: *Orientation of the T regions in NiO (ferromagnetic planes lie parallel to these vectors). [15]*

TABLE I. Bulk antiferromagnetic domains in NiO.

T domain		T_1	T_2	T_3	T_4
Associated 111-plane		[111]	[11$\bar{1}$]	[1$\bar{1}$1]	[$\bar{1}$11]
Bulk *S*-domains	1	[$\bar{2}$11]	[2$\bar{1}$1]	[21$\bar{1}$]	[211]
	2	[1$\bar{2}$1]	[$\bar{1}$21]	[121]	[12$\bar{1}$]
	3	[11$\bar{2}$]	[112]	[$\bar{1}$12]	[1$\bar{1}$2]

Figure 4.2: *Bulk antiferromagnetic domains in NiO [3]*

uniaxial stress is not easy. This is due to the large energetic cost associated with moving the domain walls in a multiple-q magnet, a result of the large magnetoelastic distortions that stabilise the domains.

Roth and Stark [17][15] proposed that the system consisted of a mixture of single-q domains [19]. These planes are directed parallel to the (111) direction *and* all equivalent directions, as detailed in figure 4.1, and the direction of the spins were proposed to lie *within* these planes. Their proposed domains are thus fully described by what are termed T-domains, which differ according to which plane contains the ferromagnetically aligned spins, plus an S-domain description, which describes the direction in which the spins point within the ferromagnetic sheets. The S-domains were proposed to contain spins in the different $\langle 211 \rangle$ directions[15][20], as indicated

52
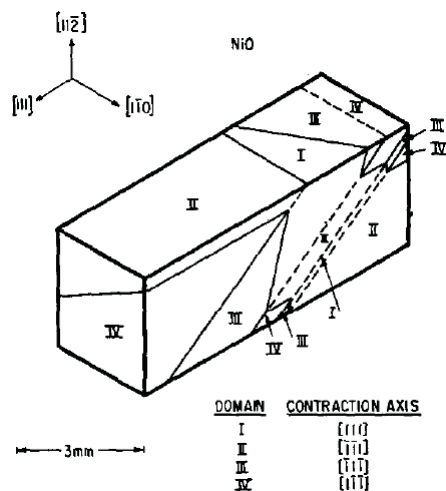
Figure 4.3: *The twinning pattern observed in a crystal by Slack et al after a high temperature anneal. The solid lines indicate visible T-walls, the dotted ones are walls with zero-facial tilt angles. This is an example of a complex 4-wall pattern where all 4 T-domains exist.* [17]

by polarisation experiments, an example of which is shown in Fig. 4.6. The different T-domains contain ferromagnetic configurations in the different 111 planes, of which there are four possible domains in the system. Their proposed domain mixture is detailed in table 4.2 and an example of a mixture that was observed in a crystal by Slack shown in figure 4.3.

T-domains are the real space manifestation of K-domains. They exist in multiple-q magnets as a result of the different Bragg spots, corresponding to different translational symmetries in real space, being related by the point group symmetry of the Hamiltonian. Due to the existence of T-domains, a domain wall can exist between two domains that have different, *distinct* Bragg spots, and this domain wall can be constructed from multiple-q states. This type of domain wall will be crucial to our reconstruction phenomenon, and is in contrast to the simple rotation of spins seen in normal magnetic systems.

For normal magnets that possess only one distinct Bragg spot, the mixture of domains solely involves S domains, related by the global rotations of spins that maintain the magnetic phase. If a spin orbit coupling exists, the orbital population becomes biased according to perturbative spin-orbit effects and the degeneracy is

broken into longitudinal or transverse cases. For the longitudinal case, the spin direction in real space is parallel to the wavevector $\mathbf{k}_{min}$ and for the transverse case perpendicular to it. Additionally, for the transverse case, there only exists two degenerate configurations with respect to spin direction, or in other words two domains in the real system, such that the spin directions lie within the plane perpendicular to $\mathbf{k}_{min}$ *and* are orthogonal to each other. The spin quantisations respect the symmetry of the system and normally lie either along crystallographic directions, along body-diagonals, or along face diagonals. S-walls between these types of domains consist of a rotation of the spins.

Magnetoelastic Distortion

There is often a magnetoelastic distortion associated with the different domains due to the magnetism breaking the symmetry present in the paramagnetic phase. This is via spin-orbit coupling; as described above, the perturbative spin orbit effect causes a bias in the orbital population. This leads to non-spherically-symmetric spatial distributions for the spins and allows the lattice to distort to gain energy from the Coulomb attraction and hopping. Thus, the different S-domains distort in different directions according to the direction of the spin within the domains, and crystallographic twinning occurs. However, the distortion is perturbatively small, and could not be observed by x-rays or the crystallographic techniques available at the time of Roth and Stark's analysis.

There is however another driver of magnetoelastic distortion that is present for multiple-q systems and which is of a much larger energy scale. The distortion is driven again by orbital population bias, but the orbital degeneracy is split on the scale of the magnetic interaction. This is caused by the magnetic multiple-q spin state reducing the symmetry of the system to tetragonal, and can lead to a sizeable distortion - $Mn_{1-x}Ni_x$ distorts by 6% [21]. As such, domain mixtures can be stabilised further than the stability offered by spin-orbit effects, and the transformation from
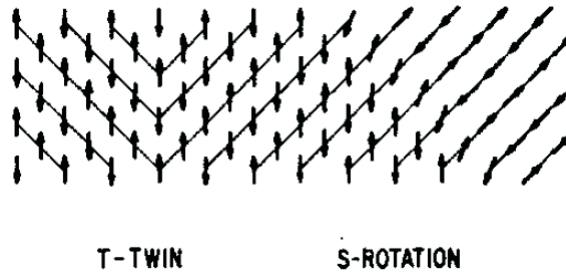
Figure 4.4: *Illustration of the different T and S domains found in Ni. The section is parallel to (100). The traces of the ferromagnetic sheets are shown and all of the spins lie within (111). [15]*
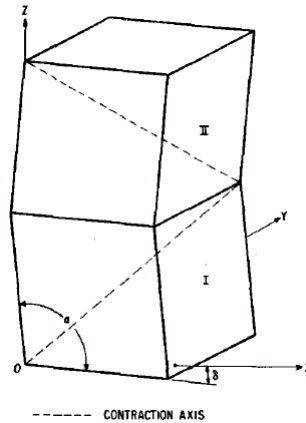
Figure 4.5: *An exaggerated model of the rhombohedral distortion in NiO below T_N. The Oxyz axes are orthogonal. The rhombohedral angle α is greater that 90 deg, and each of the rhombohedral axes makes an angle δ with the Oxyz axes. A twin wall on a (001) plane between T-domains of types I and II are shown. [17]*

one domain to another or rather the movement of domain walls requires a much larger energy scale.

Roth *et al* propose that the walls between the T-domains do not involve any rotation of the spin, so that the walls are located between T-domains along faces that have a ferromagnetic spin phase. Their proposal can be seen in figure 4.4 which illustrates their T and S wall types. The model is based on observing the rhombohedral twinning that is the result of magnetoelastic distortion of the domains due to the non-cubic symmetry of the spin states involved, and is illustrated in figure 4.5. It was found that twinning between T-domains only occurred along two different faces, and this constraint was explained via the non-rotation of spins.

However, a domain wall constructed in this way is energetically terrible due to the large Heisenberg cost of aligning spins ferromagnetically along the wall in a direction that should be antiferromagnetically aligned according to the Heisenberg interaction. The spin directions of the twinned domains is actually unknown since this information is not available from the type of experiments performed on the material, nor from the distortion directions. This leaves room for another, much more likely scenerio: twinning between different T domains of orthogonal spin direction with respect to each other. In this way, a domain wall can be set up that rotates the spins from one T domain to the other by passing through a double-q state which is energetically close in energy. This type of wall will be used for the magnetic reconstruction phenomenon we shall be proposing.

Magnetoelastic distortions can help to solve the problem of distinguishing between single-q domain mixtures and 2q or 3q states. For example, the reason why the generally accepted single-q structure of UO_2[22] was challenged was the lack of magnetoelastic tetragonal deformations that would be present. The triple-q structure was hence proposed for UO_2 due to its maintenance of the cubic symmetry which would not lead to any such distortion and subsequent experiments and analysis seem to confirm this analysis [23].

The application of uniaxial pressure can be used to distinguish between single-q multi-domain and multiple-q systems due to the difference in spin symmetry that leads to the large magnetoelastic distortion discussed. Specifically, single and double-q magnetic states have tetragonal symmetry whereas triple-q states have cubic symmetry. On applying a uniaxial stress to a magnetic material, one can move the domain walls as one domain is energetically favourable over others and this can occur if the domains are single or double-q domains due to the broken cubic symmetry; the pressure is favoured by those domains whose AFM phase is in the uniaxial direction, since magnetic energy can be gained from shortening these bonds whilst lengthening FM ones. For the UO_2 compound, the lack of biased population of Bragg

spots after applying uniaxial pressure led to more evidence for the triple-q magnetic structure. For the NiO compound, the proposal of single-q domains was based on the redistribution of the Bragg spot intensities observed after annealing and stressing [15]. This points towards NiO consisting of single-q domains, since the percentages of the total intensity moved from being approximately equally distributed between the 4 different T-domains to becoming 98.7% of a single type, the other 1.3% assigned to the only other type that can be involved in the crystallographic twinning with the dominant domain. However, the annealing and stressing processes could instead have forced the system out of a double-q structure if the energies were large enough, and so it is not possible to state the type of spin states within the domains with complete certainty. In addition, the rhombohedral distortion also does not indicate which multiple-q state the material takes since the contraction along the $< 111 >$ axes, occuring to shorten antiferromagnetically aligned spins and lengthen ferromagnetically aligned spins, can result from 1q, 2q or 3q spin configurations

Domain Mixtures and Reconstruction in Type-1 Materials

The spin configuration of the type-3 NiO compound can be mapped to type-1 by introducing an oscillation of π in the direction (111). Thus the analysis of domains so far presented can be applied easily to the discussion of γ-Mn Ni that follows and also to the reorientation and reconstruction studies tackled later. A point crucial to these studies is that the surface domain distribution is dictated by bulk rather than surface effects, as is demonstrated by experiments on cleaved surfaces of NiO using polarisation-dependent x-ray absorption. The domain mixture at the surface was consistent with that of the bulk, with a mixture of T-domains being observed[3]. Additionally, it was observed that surface roughness, in terms of defects, does not affect the domains. In particular, on heating above the Néel temperature and subsequently cooling, the domain structure reappears to take the same pattern, indicating it is controlled by defects and stresses that are already incorporated within the crys-
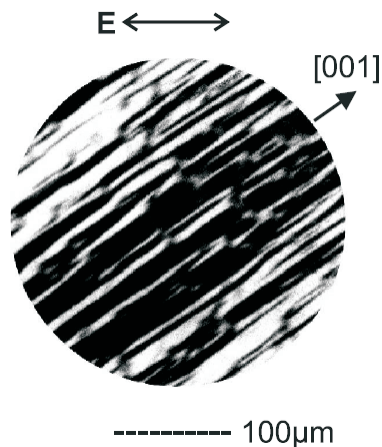
Figure 4.6: *AF domains on a cleaved NiO surface. The bright and dark areas on the image indicate smaller and larger angles between magnetic moments and light polarisation, where the direction of light polarisation is shown by the double-headed arrow. The field of view is 300 µm [3]*

tal, probably formed during growth. Thus the preference of a particular state by the surface does *not* overcome the domain mixture present in the bulk so that the entire crystal simply takes this state. Rather there is scope for magnetic reconstruction to occur since there exist domains in the bulk consisting of states not preferred by the surface. However since there is still a T-domain distribution on the surface for NiO, reconstruction has not occurred for this material.

4.2 Stabilisation of Different MSDW states

Multiple-q magnets are very interesting since they can 'heal' disorder introduced to them [24][25][26][27] (and references therein). Surfaces can be thought of as a type of impurity in terms of missing spins in a system, in the same way as an impurity could be the introduction of a spin with a modified moment or coupling. A cluster calculation has been performed by Long to calculate the effect of perturbing the length of an impurity's moment on the spin configuration[24], with the result that the spins within a non-collinear multiple-q state reorient around the impurity with a rotation that is finite and sizeable in order to compensate for the loss in magnetic energy. In the following section it will be shown for the case of a missing spin

that this reorientation again occurs in non-collinear multiple-q magnets and not in collinearly-arranged magnetic spins systems and in this way multiple-q magnets can indeed react to a surface in an interesting way. Single-q states do not have the capacity to reorient around an impurity (which could also be a site containing a spin with a different moment or with different coupling strengths), since the loss of the impurity spin does not alter the collinear alignment of the local field to any spin, and the only way to compensate for this loss of moment is to alter the length of spins, an energetically-costly move.

As such, the introduction of impurities to a system serves to stabilise *multiple* spin density waves (MSDW) over single-q states (SSDW). There are other effects that are believed to stabilise different MSDW states, which include ordering-by-disorder [27][26][28](and references therein), magnetoelasticity, quantum fluctuations and impurities [24]. Ordering-by-disorder was termed by Villain in work concerning the nearest neighbour Ising antiferromagnet on an FCC lattice [29]. The term describes the breaking of degeneracy in a frustrated system by thermal fluctuations, favour those ground states whose low energy excitations have the largest density of states. Henley [26] extended the work to n-component vector spin systems, using a spin wave calculation and minimising a free energy that included temperature via entropy terms. The work indicates thermal fluctuations favour collinear states, in a similar way to quantum fluctuations. We shall now analyse the effect of quantum fluctuations and also of impurities on the stabilities of the different MSDW states via perturbation theory calculations. The results will be compared and contrasted with each other in order to assess relative stability and also which of the dominant energy contributions are responsible for such stabilisations.

4.2.1 Quantum Fluctuations

Perturbation theory is performed on the following Heisenberg Hamiltonian

$$H = J \sum_{<ii'>} \mathbf{s}_i . \mathbf{s}_{i'} \qquad (4.2.1)$$

$$= H_0 + \Delta H. \qquad (4.2.2)$$

The quantum fluctuations are considered in the classical limit and are best described by performing a Holstein-Primakoff transformation on the spins. The transform acts to describe a state according to the number of bosons at each site, where the boson represents a quanta of fluctuation away from the z-direction. The transformed spin operators in this new bosonic basis are given by:

$$\mathbf{s}_i^z = S - b_i^\dagger b_i \qquad (4.2.3)$$

$$\mathbf{s}_i^+ = \sqrt{(2S - b_i \dagger b_i)} b_i \qquad (4.2.4)$$

$$\mathbf{s}_i^- = b_i^+ \sqrt{(2S - b_i^\dagger b_i)}. \qquad (4.2.5)$$

The operators are expanded to first order in $\sqrt{S}$, which is valid in the classical limit $S \to \infty$. The real space spin vector can thus be represented incorporating the quantum nature, up to the appropriate order, as:

$$\mathbf{s}_i = \left(\sqrt{(S/2)} b_i^\dagger, \sqrt{S/2} i b_i^\dagger, S \right) \qquad (4.2.6)$$

$$\mathbf{s}_i = S\hat{\mathbf{e}}_3 + \sqrt{S} b_i^\dagger \hat{\mathbf{e}}_+ + \sqrt{S} b_i \hat{\mathbf{e}}_-, \qquad (4.2.7)$$

with $\hat{\mathbf{e}}_+ = \left(1/\sqrt{2}\right) \left(\hat{\mathbf{e}}_1 + i\hat{\mathbf{e}}_2\right)$ and $\hat{\mathbf{e}}_- = \left(1/\sqrt{2}\right) \left(\hat{\mathbf{e}}_1 - i\hat{\mathbf{e}}_2\right)$, where $\hat{\mathbf{e}}_1$, $\hat{\mathbf{e}}_2$, $\hat{\mathbf{e}}_3$ form an orthonormal basis and $\hat{\mathbf{e}}_3$ is the direction the classical spin takes in the ground state.

To perform perturbation theory, firstly an appropriate H_0 and associated eigenstates must be decided upon. H_0 is chosen to commute with $\hat{\mathbf{s}}_z$ such that the eigenstates used in the determination of the perturbation will be those that describe all

available quantum spin states in our new representation of the spins. These eigenvectors are described by the number of bosons on each site, $(b_1^+)^{n_1}...(b_m^+)^{n_m}...|0\rangle$. As such, H_0 is chosen to be

$$H_0 = J \sum_{<ii'>} s_i^z s_{i'}^z. \tag{4.2.8}$$

In this way, the unperturbed Hamiltonian does not couple bosons into the states since there are no $\hat{s}_i^+$ or $\hat{s}_i^-$ terms to do this. As such, there is no potential for the existence of quantum fluctuations as there is no potential for a boson to exchange, or in other words the number of bosons on each site to fluctuate.

The full Hamiltonian is now obtained by substituting the quantum representation of the spins as given by 4.2.7 and the resulting terms analysed. However it must first be taken into account that this representation assumes the classical direction of each spin is aligned with the (global) z-direction rather than to their own classical quantisation direction. The states being considered are not simple classical ferromagnetic states but instead are general MSDW states. We shall therefore need to perform rotations on the spins of our general MSDW state in order that all spins have their classical directions aligned to the single global frame that the Heisenberg Hamiltonian acts in. This is achieved using the rotation matrices R_i:

$$\tilde{\mathbf{s}}_i = R_i \mathbf{s}_i. \tag{4.2.9}$$

In this representation our Hamiltonian becomes

$$H = J \sum_{<ii'>} \tilde{\mathbf{s}}_i^\top (R_i^{-1} R_{i'}) \tilde{\mathbf{s}}_{i'} \tag{4.2.10}$$

and we are now in a position to substitute the quantum representation of the spins which gives

$$H = JS^2 \sum_{<ii'>} \hat{\mathbf{e}}_3^\top R_i^{-1} R_{i'} \hat{\mathbf{e}}_3 + 2JS\sqrt{S} \sum_{<ii'>} \hat{\mathbf{e}}_3^\top R_i^{-1} R_{i'} \hat{\mathbf{e}}_+ b_{i'}^+$$

$$+ JS \sum_{<ii'>} \hat{\mathbf{e}}_+^\top R_i^{-1} R_{i'} \hat{\mathbf{e}}_+ b_i^+ b_{i'}^+. \quad (4.2.11)$$

Applying non-degenerate perturbation theory (since there is no degeneracy associated with the ground state) one obtains the first order perturbation to the energy:

$$\epsilon_1 = \langle 0|\Delta H|0\rangle. \quad (4.2.12)$$

The term $\Delta H|0\rangle$ is best determined by evaluating:

$$
\begin{aligned}
H|0\rangle = (H_0 + \Delta H)|0\rangle = \; & J \quad S^2 \sum_{<ii'>} \hat{\mathbf{e}}_3^\top R_i^{-1} R_{i'} \hat{\mathbf{e}}_3 |0\rangle \\
+ \; & JS\sqrt{S} \sum_{<ii'>} \hat{\mathbf{e}}_3^\top R_i^{-1} R_{i'} \hat{\mathbf{e}}_+ b_{i'}^+ |0\rangle \\
+ \; & JS\sqrt{S} \sum_{<ii'>} \hat{\mathbf{e}}_+^\top R_i^{-1} R_{i'} \hat{\mathbf{e}}_3 b_i^+ |0\rangle \\
+ \; & JS \sum_{<ii'>} \hat{\mathbf{e}}_+^\top R_i^{-1} R_{i'} \hat{\mathbf{e}}_+ b_i^+ b_{i'}^+ |0\rangle. \quad (4.2.13)
\end{aligned}
$$

The first term is $H_0|0\rangle$, and so ΔH, the contributions from quantum fluctuations, is assigned to be the second, third and fourth terms according to the order to which we are working.

We proceed to analyse the first three terms by making use of a property of the rotations which is a result of the symmetry inherent in the system.

The rotations $\mathbf{R}_\alpha$ required to map the spins in the different sublattices $\alpha = [0, 3]$ of the type-q AFM FCC magnet to the z-direction spin $\tilde{\mathbf{s}}_i$ are constructed from $\mathbf{R}_0$, the matrix that rotates the spin in sublattice $\alpha = 0$ to the z-direction, and the three matrices $\mathbf{T}_\alpha$ which map the spins in each sublattice $\alpha = 1, 2, 3$ to $\mathbf{s}_0$:

$\hat{R}_0 =$

$$\begin{bmatrix} \cos\theta\cos\phi & \cos\theta\sin\phi & -\sin\theta \\ -\sin\phi & \cos\phi & 0 \\ \sin\theta\cos\phi & \sin\theta\sin\phi & \cos\theta \end{bmatrix}$$

$\hat{T}_1 =$

$$\begin{bmatrix} 1 & 0 & 0 \\ 0 & -1 & 0 \\ 0 & 0 & -1 \end{bmatrix}$$

$\hat{T}_2 =$

$$\begin{bmatrix} -1 & 0 & 0 \\ 0 & 1 & 0 \\ 0 & 0 & -1 \end{bmatrix}$$

$\hat{T}_3 =$

$$\begin{bmatrix} -1 & 0 & 0 \\ 0 & -1 & 0 \\ 0 & 0 & 1 \end{bmatrix}$$

such that the $\mathbf{R}_{\alpha \neq 0}$ correspond to $\mathbf{R}_\alpha = \mathbf{T}_\alpha \mathbf{R}_0$. Given this notation, the property

$$\mathbf{s}^0 + \mathbf{s}^1 + \mathbf{s}^2 + \mathbf{s}^3 = 0 \tag{4.2.14}$$

leads to an identity for the rotations

$$\sum_{\alpha=0}^{3} R_\alpha = 0, \tag{4.2.15}$$

which can be understood by noting that $\mathbf{s}^0 = R_0 \tilde{\mathbf{s}}_i$ and subsequently acting the $\mathbf{R}_\alpha$'s that map to the spin $\tilde{\mathbf{s}}_i$ to the spins on other sublattices to obtain 4.2.14.

Substituting (4.2.15) into the first term of (4.2.13) and splitting the spins into different sublattices in order to exploit the symmetry of the general MSDW spin state, one obtains

$$H_1|0\rangle = JS^2 \sum_\nu \sum_\alpha \sum_{\alpha' \neq \alpha} \sum_{X_{\alpha'}} \hat{\mathbf{e}}_3^\top \mathbf{R}_{\alpha'}^{-1} \mathbf{R}_\alpha \hat{\mathbf{e}}_3 |0\rangle, \qquad (4.2.16)$$

where ν is the number of sublattices in the system and $X_{\alpha'}$ are nearest neighbours to spins in sublattice α'. Rewriting the expression to make use of identity 4.2.15 one arrives at

$$H_1|0\rangle = \frac{1}{3} N X J S^2 |0\rangle, \qquad (4.2.17)$$

where $X = 12$ is the total number of nearest neighbours per spin and N the total number of spins in the system. Thus the ground state energy of the unperturbed system, or rather the classical ground state energy, is $-\frac{1}{3} J S^2 N X$. The second term and third term are tackled in a similar way and return

$$
\begin{aligned}
H_2|0\rangle \;=\; & JS\sqrt{S} \sum_\nu \sum_\alpha \sum_{\alpha' \neq \alpha} \sum_{X_{\alpha'}} \hat{\mathbf{e}}_3^\top \mathbf{R}_{\alpha'}^{-1} \mathbf{R}_\alpha \hat{\mathbf{e}}_+ b_{i'}^\dagger |0\rangle \\
& + JS\sqrt{S} \sum_\nu \sum_\alpha \sum_{\alpha' \neq \alpha} \sum_{X_{\alpha'}} \hat{\mathbf{e}}_+^\top \mathbf{R}_{\alpha'}^{-1} \mathbf{R}_\alpha \hat{\mathbf{e}}_3 b_i^\dagger |0\rangle \\
=\; & 0. \qquad\qquad\qquad\qquad\qquad\qquad\qquad\qquad\qquad (4.2.18)
\end{aligned}
$$

This is not suprising - the ground state $|0\rangle$ is the state that is stable against first order fluctuations. As a result, the first order correction to the energy does not lead to a breaking of degeneracy, indicating that two spin fluctuations are effectively independent at this order and so the second order correction is required:

$$\delta\epsilon_2 = \frac{\sum_{n\neq0}\langle 0|\Delta H|n\rangle\langle n|\Delta H|0\rangle}{\epsilon_0 - \epsilon_n}.$$

(4.2.19)

For the order to which we are working, only the eigenstates $|k\rangle = b_{i'}^+ b_i^+ |0\rangle$, where i and i' are nearest neighbours, give a non-zero value for $\langle n|\Delta H|0\rangle$, and so the summation over n can be replaced with a summation over $|k\rangle$ and the completeness relation applied to simplify the expression to:

$$\delta\epsilon_2 = \frac{\sum_{k\neq0}\langle 0|\Delta H\Delta H|0\rangle}{\epsilon_0 - \epsilon_n}.$$

(4.2.20)

Given that

$$\Delta H = JS \sum_{<ii'>} \hat{\mathbf{e}}_+^\top R_i^{-1} R_{i'} \hat{\mathbf{e}}_+ b_i^+ b_{i'}^+,$$

(4.2.21)

the second order perturbation to the ground state energy is given by

$$\delta\epsilon_2 = -\frac{3}{2XJS} \sum_{<ii'} 2J^2S^2 |\hat{\mathbf{e}}_+^\top R_i^{-1} R_{i'} \hat{\mathbf{e}}_+|^2$$

(4.2.22)

and simplified to

$$\delta\epsilon_2 = -JSN \sum_{\alpha=1}^{3} |\mathbf{X}^\top \mathbf{T}_\alpha \mathbf{X}|^2,$$

(4.2.23)

where $\mathbf{X} = \mathbf{R}_0 \hat{\mathbf{e}}_+$. Calculating $\delta\epsilon_2$ explicitly, given the rotation matrices, we find

$$\delta\epsilon_2 = -JSN \left[4\left(|x_1|^4 + |x_2|^4 + |x_3|^4\right) - |x_1^2 + x_2^2 + x_3^2|^2 \right],$$

(4.2.24)

where x_1, x_2, x_3 are the components of $\mathbf{X}$. Using spherical polar coordinates to describe the MSDW state, it can be shown, using complex analysis, that

$$\delta\epsilon_2 = -JSN(1 - 2\sin^2\theta\cos^2\theta - 2\sin^2\phi\cos^2\phi\sin^4\phi), \qquad (4.2.25)$$

which is minimised for collinear states.

4.2.2 Impurities

We now perform a calculation using the same methodology as the perturbation calculation we applied in the previous section for analysing the effect of quantum fluctuations. The impurity is modelled as the absence of a single spin at location at the origin $i = 0$, such that the perturbation to the system H_0 is now given by

$$\Delta H = -2J \sum_{[0i]} \mathbf{s}_0.\mathbf{s}_i \qquad (4.2.26)$$

leading to

$$\Delta H|0\rangle = -2J \sum_{[0i]} \left[S^2 \hat{\mathbf{e}}_3^\top R_{i'=0}^{-1} R_i \hat{\mathbf{e}}_3 |0\rangle + S\sqrt{S} \hat{\mathbf{e}}_+^\top R_{i'=0}^{-1} R_i \hat{\mathbf{e}}_3 b_0^+ |0\rangle + \right.$$

$$\left. S\sqrt{S} \hat{\mathbf{e}}_3^\top R_{i'=0}^{-1} R_i \hat{\mathbf{e}}_+ b_i^+ |0\rangle + S\hat{\mathbf{e}}_+^\top R_{i'=0}^{-1} R_i \hat{\mathbf{e}}_+ b_0^+ b_i^+ |0\rangle \right].$$

We again analyse the terms to determine which unperturbed eigenstates dominantly contribute to the perturbed state and perturbation to the energy. The summation is split as before into firstly a sum over sublattices and secondly a sum over the nearest neighbours present in each sublattice in order to make use of the rotation identity. The first term simplifies to

66

$$-2J \sum_{[0i]} S^2 \hat{\mathbf{e}}_3^\top R_{i'=0}^{-1} R_i \hat{\mathbf{e}}_3 |0\rangle = 8JS^2 |0\rangle \tag{4.2.27}$$

and returns the magnetic energy lost from taking the impurity spin out of the lattice ignoring the effect of fluctuations. The second term vanishes. This term is associated with the interaction of the impurity spin with its local field derived from the surrounding nearest neighbour spins. Since the local field is parallel to the direction of the spin that has been taken out, any fluctuations that were associated with this missing spin did not couple to the local field, and as such the loss of the spin at the origin does not affect the energy of the system through this contribution. The third term however does not necessarily vanish. This is because the loss of the impurity perturbs the local field of the spin $\mathbf{s}_i$ that neighbours the missing spin. As such, the local field to $\mathbf{s}_i$ is not necessarily collinear any more, and so fluctuations of this spin may couple to its local field. This is therefore the leading order process by which the loss of a spin affects the system's energy, and in particular the change in local field can cause the neighbouring spins to gain from their fluctuations.

The second order perturbation is thus given by

$$
\begin{aligned}
\delta\epsilon_2 &= \frac{6}{XJS} \sum_{[0i]} J^2 S^3 |\hat{\mathbf{e}}_3^\top R_{i'=0}^{-1} R_i \hat{\mathbf{e}}_+|^2 \\
&= 2JS^2 \sum_{\alpha=1}^{3} |\mathbf{Y}^\top T_\alpha \mathbf{X}|^2,
\end{aligned}
\tag{4.2.28}
$$

where $\mathbf{Y} = R\hat{\mathbf{e}}_3$ is the uniformly-rotated classical spin direction. The state taken by this reorientation can be deduced by again determining the perturbative energy in terms of θ and ϕ and minimising the resulting expression. Performing complex analysis in a similar way as previously, and given that $\mathbf{X}.\mathbf{Y} = 0$, the solution is determined to be

$$\delta\epsilon_2 = -2JS^2 \sin^2\theta(\cos^2\theta + \sin^2\phi\cos^2\phi\sin^2\theta). \qquad (4.2.29)$$

There is no saving for the collinear case and a maximum energy saving for the triple-q case at $\delta\epsilon_2 = \frac{2}{3}JS^2$, in direct contrast to the states stabilised by the quantum fluctuations alone.

These fluctuations perturb the energy from that of the classical state by an order JS^2, i.e. of the order of the classical energy, in comparison with the order JS by which quantum fluctuations associated with the entire lattice gained from the classical state. As such, the loss of a spin causes a much larger perturbation of the nearest neighbouring spins from the classical state than that caused simply from quantum fluctuations, and the spins near the impurity relax around it to compensate for the loss of a spin.

The perturbative calculation has limitations in terms of validity, as the energy perturbation to the classical ground state is not small in the case of the impurity perturbation; indeed, it is of the same order as the energy of the unperturbed (classical) Hamiltonian. This is because the perturbation of the neighbouring spins to the lost spin is in no way small - the spins rotate through relatively large angles in order to compensate for the loss of antiferromagnetic energy , a result of only the nearest neighbour spins having been allowed to move to compensate for the impurity. The solution to the classical problem, whereby the impurity is free to affect spins up to any length scale, is tricky for exactly this reason of large length scale.

However, the two calculations that have been performed give an indication as to what processes are responsible for making either the collinear or non-collinear MSDW states stable. The quantum fluctuations stabilise the collinear state due to the coupling of neighbouring fluctuations. These fluctuations are only coupled if they have a component parallel to each other, requiring therefore that the original

spins are collinear such that the fluctuations occur in the same plane. On the other hand, the introduction of an impurity in terms of the loss of a spin stabilises the triple-q state due to the interaction of the neighbouring spins with the lost spin, $\mathbf{s}_i$, with their local field that has been perturbed by the loss of a spin and which therefore may no longer lie parallel to $\mathbf{s}_i$. This occurs for the case of a non-collinear MSDW magnet and can be thought of as the ability of the state to compensate for the lost spin by rotating the spins.

4.3 Case Study: Phase Transitions Between SDW states

We present an overview of phase transitions that are observed when the γ-manganese is alloyed with most other transition metals. A cascade of structural phase transitions is observed as the doping concentration increases, and this is attributed to magnetic phase transitions between different spin density waves states. The magnetic transitions are believed to occur due to the presence of impurities in the γ-Mn in the form of the doping element, a composition also referred to as alloy disorder. Different SDW states are then stabilised due to the impurity, with the particular state stabilised being a function of the concentration of impurity. A picture arises whereby, on increasing the doping concentration, the regions in which the spins relax around impurities begin to overlap. This results in the correlation length of the magnetic component associated with the spin relaxation increasing until the length is over a macroscopic scale and long-range order sets in. This new order shows up as Bragg spots appearing at wavevectors corresponding to the new magnetic component. Diffuse scattering can be associated with the new magnetic components surrounding the impurity concentrations at which long range order of the new magnetic order has not yet set in, due to the local nature of the impurity and resulting reorientation. Calculations by Long et al[30] analysing the diffuse scattering agree
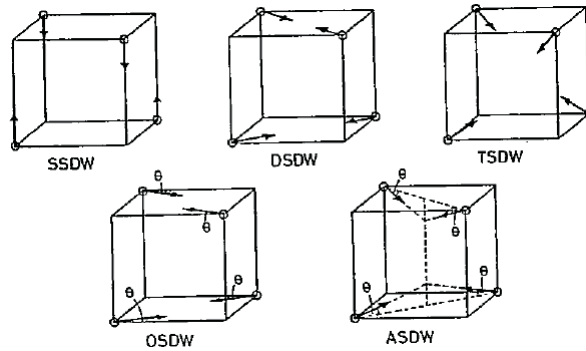
Figure 4.7: *Five distinct types of multiple-q state found in FCC type-q antiferromagnets: Single(S), double(D), triple(T), orthorhombic(O) and another tetragonal (A) spin density wave (SDW) states. The magnetic unit cell is simple cubic and a single cell is depicted in each case. [28]*

with experiments on γ-Mn$_{73}$Ni$_{27}$.

There is an associated magnetoelastic distortion because, for MSDW systems, the spin waves are coupled to the phonons, and these phonons are equivalent to elasticity, being distortions of the charge density. As discussed in the previous section, magnetoelastic distortions can occur if the MSDW state does not take a cubic arrangement such that the cubic symmetry of the system is broken, and these distortions are observed experimentally via lattice parameter and elastic constant measurements, and what's more predicted theoretically via expected spin wave and phonon softening at magnetic transitions.

We shall focus primarily on the alloy γ-Mn-Ni. The 'pure' alloy of γ-Mn has an antiferromagnetic state, labelled as the SSDW (single spin density wave) state in figure 4.7, which consists of two antiferromagnetic sublattices. The spin direction points in the (100) direction [4]. The electrons are believed to be itinerant and have a predominantly d-orbital moment. There is a magnetoelastic distortion due to the broken cubic symmetry to the tetragonal symmetry of the spin state and this distortion is a sizeable 6%[28].

Experiments by Honda *et al* [4] show an alteration in the symmetry of the lattice structure as a function of both temperature and Ni concentration, which can be seen in figures 4.8 and 4.9 via the variation of the lattice parameters. In particular, the
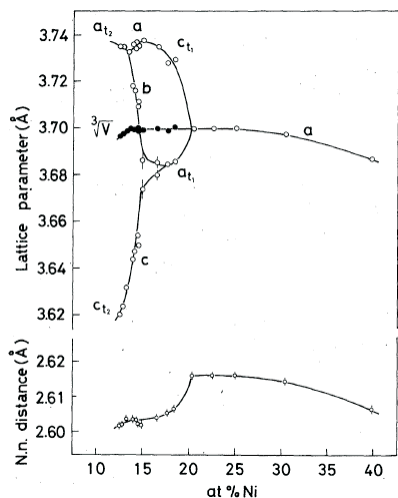
Figure 4.8: *Composition dependence of lattice parameters and nearest neighbour distance of γ-Mn Ni alloys at 24°C.V is the unit cell volume so that $\sqrt[3]{V}$ is the cubic lattice parameter[4].*

system passes through cubic, tetragonal and orthorhombic phases. t_1 refers to the tetragonal and orthorhombic types in which the lattice parameter $a < c$, and t_2 to the $a > c$ case. For the case of 15% Ni, the structure can be seen in figure 4.9 to convert as the temperature is increased through t_1 orthorhombic, t_2 orthorhombic, t_2 tetragonal and finally becomes cubic symmetric. The 13.9% alloy, also shown, indicates transitions from t_2 orthorhombic to t_2 tetragonal and finally to cubic. As a function of increasing Ni concentration for measurements taken at 24°C, figure 4.8 shows a cascade of structural transitions from t_2 tetragonal to orthorhombal to t_1 tetragonal and finally to a cubic phase. The nearest neighbour distance can be seen to increase with concentration up to the cubic phase, at which it begins to decrease. Furthermore, this variation in nearest neighbour distance is smooth except at the t_1-tetragonal-to-cubic boundary, at which point there is a sharp change.

The spin orbit distortion is apparent in experimental data obtained via neutron scattering by Uchisiba *et al* [31]. The spin configuration in the tetragonal SSDW states was determined. It was found that the t_2 tetragonal phase has the spin direction pointing along the c-axis and the t_1 tetragonal phase spin pointing orthogonally to the c-axis, such that the ferromagnetic layers always point perpendicular to the

71
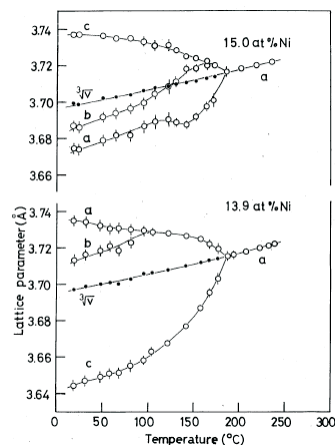
Figure 4.9: *Temperature dependence of lattice parameters of γ-Mn Ni alloys for 13.9 and 15.0 at % Ni[4].*

spin direction, which points parallel to the shortest axis. This is in agreement with distortions expected from spin-orbit coupling effects.

A summary of the phase boundaries between the different states defined by the structural symmetry is shown by the phase diagram of figure 4.10 as a function of temperature and concentration.

Honda *et al* also undertook elastic measurements of the structure as a function of temperature and concentration, in terms of Young's modulus (Y), internal friction and shear modulus, the latter of which is shown in fig.(4.11). The shear modulus shows the steepest temperature dependence at the Néel temperature where there is a step-type change of the curve, indicative of a first order transition. The minimum corresponds to a t_1 to cubic transition. Young's modulus bears a close resemblance to the behaviour of the shear modulus. The unit cell volume does not change appreciably at the structural transition temperatures, indicating a volume-conserving distortion is at work; in other words, a decrease in one dimension is accompanied by a roughly compensatory expansion in the orthogonal dimension.

Long and Yeung [32]studied magnetic states that could bring about the structural distortions and associated elastic behaviour observed by Honda *et al* and Lowde *et al* [6] and were able to construct models that reproduced the behaviour seen experi-
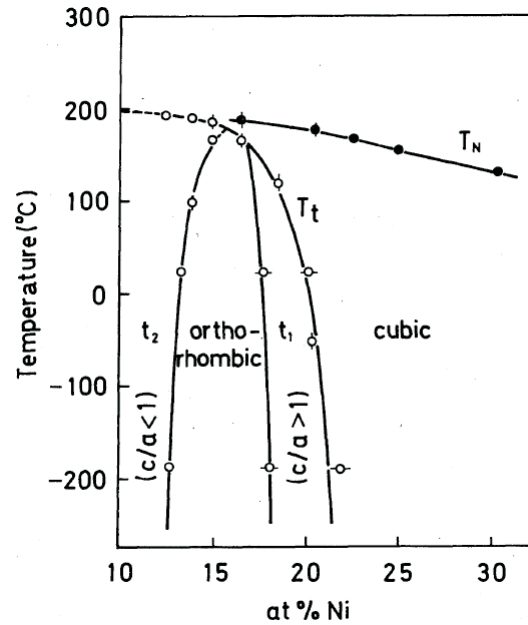
Figure 4.10: *Magnetic and crystallographic phase diagram of the γ-Mn-Ni alloy system. Both t_1 and t_2 are tetragonal. T_N is the Néel point and T_t the distortion temperature. [4]*
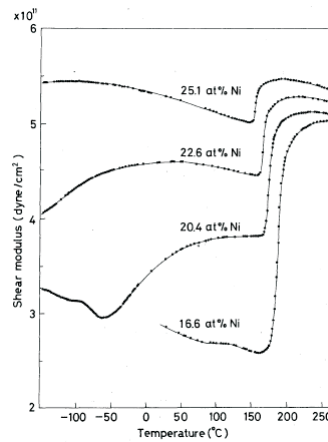
Figure 4.11: *Temperature dependence of shear modulus of γ-Mn-Ni alloys [4].*

mentally. The work allows the prediction of the behaviour of the elastic constants at the magnetic phase transitions involving SDW states, based on the type of magnetic transition the system is undergoing.

Long and Yeung began by constructing a Landau model in terms of magnetisation order parameters and studying the types of phase transitions available to the system between states with different symmetry. The resulting phases and transitions available to these models in terms of magnetisation was then related to structural distortions via a simple magnetoelastic coupling term, which serves to couple the magnetic configuration to the lattice. The coupling of phonons to spin waves in this material is key in terms of why the magnetoelastic coupling occurs in this form. Long-wavelength phonons describe charge distortion and as such are equivalent to lattice strains. These strains cause distortions that change the symmetry of the lattice observed experimentally. Due to the nature of MSDW states, phonons and spin waves are coupled and as such a transition to a different magnetic state, which corresponds to macroscopically occupying a different spin wave, is coupled to a phonon and hence a lattice distortion. The inclusion of Ni as an impurity causes magnetic state transitions between the different MSDW states, and it is the magnetic transition that is the driving force for the structural distortions, with any stability or instability brought about by magnetoelastic effects not the dominant factor but merely serving to stabilise further any magnetic state taken by the system. The work indicates that the elasticity stabilises the SSDW state above other MSDW states.

In constructing an appropriate Landau model for the system, a model only including up to fourth order terms is not appropriate, since the model does not allow for all of the SSDW, DSDW and TSDW states as ground states. In particular, the DSDW state exists in the model as a saddle point rather than minimum. As such, a model involving up to sixth order terms and including all cubic invariants is initially studied:

$$F = \alpha m^2 + \frac{1}{2}\alpha_2 m^4 + \frac{1}{3}\alpha_3 m^6 + (\frac{1}{2}\beta_2 + \frac{1}{3}\beta_3 m^2)(m_1^4 + m_2^4 + m_3^4) +$$
$$\frac{1}{3}\gamma_3(m_1^6 + m_2^6 + m_3^6), \qquad (4.3.1)$$

where m_i are the components of magnetisation, and are defined by

$$\mathbf{s}_{\mathbf{R}_j} = \left(m_1 \cos\left(\mathbf{k}_1.\mathbf{R}_j\right), m_2 \cos\left(\mathbf{k}_2.\mathbf{R}_j\right), m_3 \cos\left(\mathbf{k}_3.\mathbf{R}_j\right) \right), \qquad (4.3.2)$$

where $\mathbf{k}_i$ are in directions corresponding to the Cartesian directions; $\mathbf{k}_i = (2\pi/a)\mathbf{e}_i$, where $\mathbf{e}_i$ is the Cartesian vector in the i'th direction. This is the specific case of $\mathbf{k}'s = \pm\pi$, for a system with a cubic-like reciprocal lattice, of the more general case we have worked with of:

$$\mathbf{s}_{\mathbf{R}_j} = \mathbf{s}_{\mathbf{k}_1} e^{i\mathbf{k}_1.\mathbf{R}_j} + \mathbf{s}_{\mathbf{k}_2} e^{i\mathbf{k}_2.\mathbf{R}_j} + \mathbf{s}_{\mathbf{k}_1} e^{i\mathbf{k}_1.\mathbf{R}_j}. \qquad (4.3.3)$$

In other words, the order parameters in the model correspond to our $\mathbf{s}_{\mathbf{k}}$ as defined in chapter 2.

α, the second order coefficient, corresponds to the inverse susceptibility, and is assumed to be linearly-proportional to temperature. This term is assumed to drive the transition both in terms of temperature and concentration, of which it is assumed to be a monotonic function. The other coefficients are functions of the type of alloy and their dependence on the variables of temperature and concentration are assumed to be small. The model permits two independent order parameters as a minimum solution, and as such there are five distinct phases as equilibria:

$$
\begin{bmatrix}
\text{SSDW} & [m_s, 0, 0] & \text{tetragonal} \\
\text{DSDW} & [m_D/\sqrt{2}, m_D/\sqrt{2}, 0] & \text{tetragonal} \\
\text{TSDW} & [m_T/\sqrt{3}, m_T/\sqrt{3}, m_T/\sqrt{3}] & \text{cubic} \\
\text{OSDW} & [m_0 \cos\theta_o, m_0 \sin\theta_o, 0] & \text{orthorhombic} \\
\text{ASDW} & [m_A \sin\theta_A/\sqrt{2}, m_A \sin\theta_A/\sqrt{2}, m_A \cos\theta_A] & \text{tetragonal}
\end{bmatrix}
$$

These SDW states are shown in figure 4.7.

The analysis of the model presents several findings. First order transitions occur for transitions SSDW↔ DSDW ↔ TSDW and so it can be proposed that the first-order cubic-to-tetragonal (c>a) structure phase transition seen by Honda corresponds to a TSDW-to-DSDW phase transition. The model also supports second-order-spin-orientation phase transitions (SOPT), in which the spins reorient *continuously* between magnetic states that possess different symmetries. At the phase transition the two different magnetic states become degenerate. Within this category there exists two cases; (1) the two states have different numbers of components for the staggered magnetisation, as in OSDW ↔ SSDW, and (2) the number of components remains the same, as in OSDW ↔ DSDW.

There is however an error in the model - the OSDW solution exists at a saddle point rather than at a minimum. In order to have α's existing at which which the OSDW and ASDW states become degenerate with those of the SSDW, DSDW or/and TSDW states, one must go to eighth order in the Landau function. An extra solution exists to this model, named the general spin density wave state (GSDW), for which there are *three* independent magnetisation components and hence the state possesses orthorhombic symmetry. In principle this state can transform into any of the other five SDW states mentioned previously, but practice there can only be transitions that involve the creation or destruction of one order parameter.

Long *et al* are able to tune the coefficients α_i, β_i and γ_i to obtain cascades of
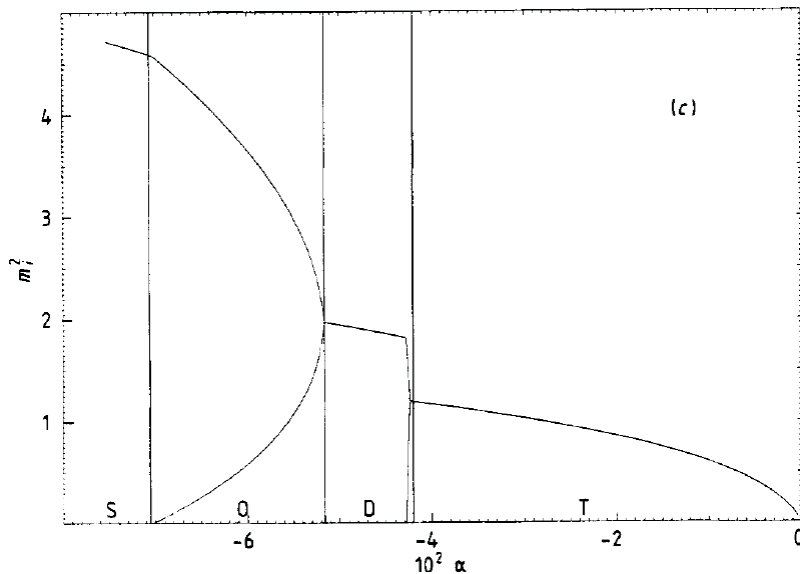
Figure 4.12: *Example of a theoretically-determined magnetic cascade, TDOS (between triple→ double→orthorhombic→single spin density wave states).[5]*

transitions as functions of α that match those seen by Honda *et al.* An example as a function of staggered magnetisation squared is shown in fig. 4.12, where a cascade TDSW →DSDW→OSDW→SSDW is shown. The phase changes are signalled by the appearance or disappearance of certain branches in the magnetisation curve.

As introduced earlier, the magnetoelastic coupling of the magnetisation to the lattice can cause structural distortions if the symmetry of the magnetic state alters due to magnon-phonon coupling in MSDW states. The driving force behind the phase transitions between states with different symmetry for the magnetisation Landau model is therefore now attributed to magnetoelasticity and this coupling is added via a 'minimum coupling term':

$$F_\epsilon = \mathbf{P}.\epsilon + \frac{1}{2}\epsilon^{'}.\mathbf{C}\epsilon. \tag{4.3.4}$$

The first term is the dominant magnetoelastic term in their minimal coupling model. The second term is the elastic strain energy term, where the tensor C_{ij} de-
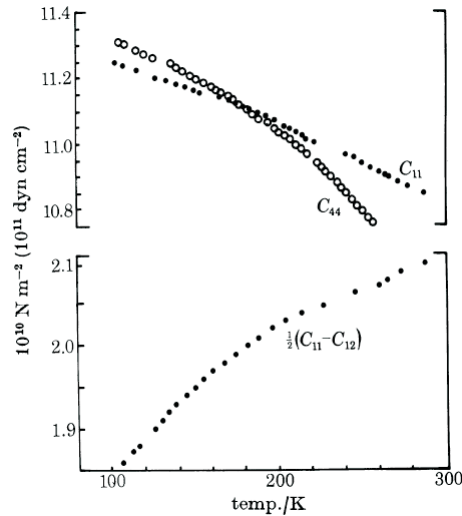
Figure 4.13: *The measured elastic constants of $Mn_{85}Ni_9C_6$. The shear elastic constant can be seen to soften as the TSDW-ASDW transition temperature is approached.[6].*

pends on the magnetisation, among other things. **P** is the magnetic pressure. Solely strains available to a lattice possessing perpendicular angles only are considered.

The stability of the spin density wave states are analysed based on the model of the free energy that consists of the magnetisation part (Landau theory) *plus* the elastic part, via a combination of fluctuation theory, renormalisation theory and finally microscopic theory. The elastic term is first minimised with respect to strain, and the resulting conditions substituted back into the free energy expression. A renormalisation of the original landau coefficients maps this function onto the original Landau expression, which is then minimised subject to self-consistency with respect to changes in magnetisation coupling to changes in elasticity. It is found that, for an SSDW state, elasticity stabilises the state further against fluctuations. For a DSDW state, the elasticity makes the states more stable to ASDW fluctuations, and conversely less stable towards the OSDW state. The presence of magnetoelasticity causes the TSDW state to be less resistant to fluctuations towards an ASDW state. In this way, the SSDW state is stabilised over other MSDW states by elasticity. This is expected due to the SSDW having the largest direction-dependent difference in magnetic interaction.
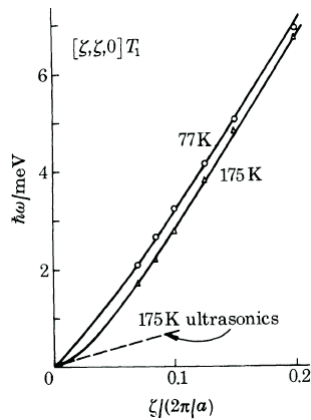
Figure 4.14: *Softening of the [110] T_1 acoustic phonon mode[6].*

In terms of the behaviour of the elastic constants, analysis of the renormalised elastic constant tensor led to several theories. Transitions between magnetic states possessing different numbers of magnetic components m_i have discontinuities in the elastic constants as observed in the t_1-to-cubic phase by Honda, with the state with the lower number of components having the lower value of elastic constant. For transitions in which the number of magnetic components remains the same, the elastic constants remain continuous across the transition and certain shear elastic constants vanish due to the change from cubic to non-cubic symmetries etc. This is demonstrated experimentally in the temperature dependence of the alloy $Mn_{85}Ni_9C_6$ [33]. Figure 4.13 shows the vanishing of the shear elastic constant at the $TSDW \leftrightarrow ASDW$, or rather cubic to tetragonal, transition. The associated softening of the [110] T_1 acoustic phonon mode that has a vibrational polarisation direction of [110] is also seen in these experiments, shown in figure 4.14. The lowering of the number of magnetic components in the state can be seen in neutron diffraction data [34], shown in figure 4.15. The intensity of one of the Bragg spots is seen to rise as the magnetism orders, and then as it begins to level off at T_{MS} it again shows a significant increase, finally levelling off at T_L. This behaviour corresponds to the system magnetically ordering in a cubic TSDW state, and then undergoing a magnetic spin reorientation transition at T_{MS}, where the spins rotate towards the basal plane continuously with
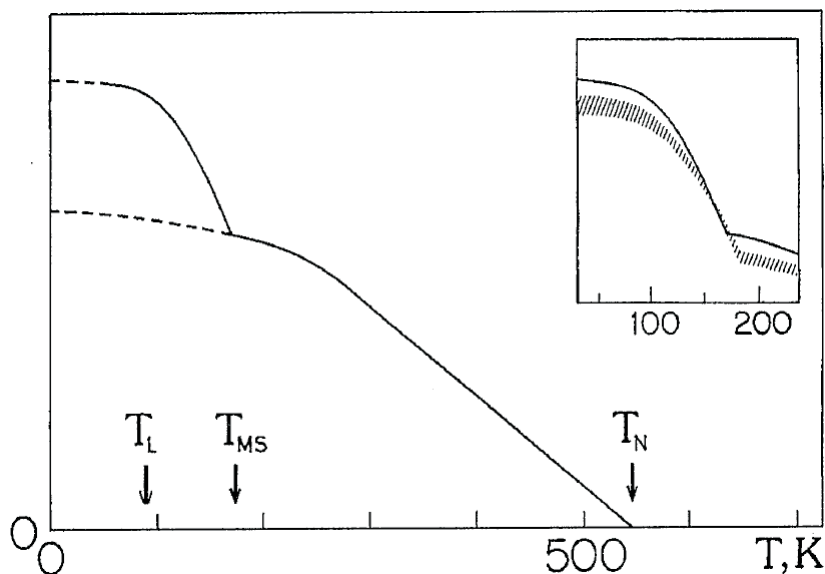
Figure 4.15: *Solid curve: the magnetic Bragg intensity $0\bar{1}1$ from a single crystal of $Mn_{85}Ni_9C_6$ as a function of temperature, showing three critical points. Broken curves by way of extrapolation show a natural division of the intensity into two components, indicating a TSDW-ASDW continuous, or 'lift-off' transition. [34].*

temperature, taking an ASDW state. The spin density is thus transferred from the third Bragg spot to the other two spots present until the system arrives at the double-q state, at which point the intensity at the two spots levels off. This type of transition termed a 'lift-off' transition if it is viewed in the context of increasing temperature.

Fig. 4.16shows structural phase diagrams theoretically produced by Long. The various phases are believed to correspond to those probed by Honda for the low temperature regime.

Magnetic surface relaxation and reconstruction can be understood using these magnetic cascades. Although there is no such quantity as a Bragg spot, due to the truncation of the system and therefore rods of magnetic scattering instead, one can consider descriptions of spots by considering the case of large-enough regions over which the scattering is observed in the perpendicular direction such that the rods approach a spot-like profile. Within this picture, as a function of depth, relaxation involves the transferral of spin density between spots, but so that there is no new
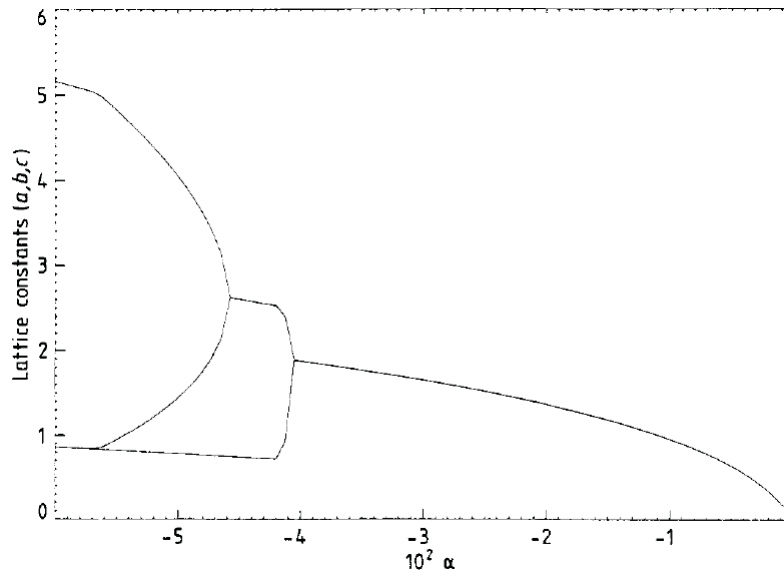
Figure 4.16: *Example of a theoretically-determined structural cascade via a strain curve, as per the minimum coupling model of Long et al.[5]*

order present, corresponding to, for example, the TSDW to DSDW transition. Conversely, magnetic reconstruction concerns the other case considered whereby a *new* magnetic component appears, as of, for example, an SSDW to OSDW transition.

Chapter 5

SURFACE MAGNETISM

5.1 Original Magnetic Surface Transitions

Phase transitions in semi-infinite systems are of many types. Lubensky and Rubin [35] identified four types of seperate surface transitions associated with the surface. Bray and Moore [36] review these different transitions by modelling with a Ginzberg-Landau-Wilson Hamiltonian for a system with $O(n)$ spin symmetry, containing an extra 'surface' contribution:

$$H = \int d^d\mathbf{x} \left[\frac{1}{2}t \sum_{i=1}^{n} \phi_i^2(\mathbf{x}) + \frac{1}{2} \sum_{i=1}^{n} (\Delta\phi_i(\mathbf{x}))^2 + \frac{u}{4} \left(\sum_{i=1}^{n} \phi_i^2(\mathbf{x}) \right)^2 \right.$$
$$\left. + \frac{1}{2}c\delta(z) \sum_{i=1}^{n} \phi_i^2(\mathbf{x}) - h_1\delta(z)\phi_1(\mathbf{x}) \right], \qquad (5.1.1)$$

where $\phi_i(\mathbf{x})$ is the i'th Cartesian component of the n-component order parameter, and the reduced temperature $t \propto (T - T_c^{MF})$ where T_c^{MF} is the mean-field transition temperature. The integration over $\mathbf{x}$ is over the half-space $z \geq 0$. The delta function $\delta(z)$ serves to incorporate a magnetic field, h_1, that couples to one of the components of the order parameter, and a surface coupling perturbation, c. This surface perturbation locally changes the value of T_c^{MF}. For a spin system with nearest neighbour exchange interactions $J(1 + \gamma)$ between spins in the surface layer
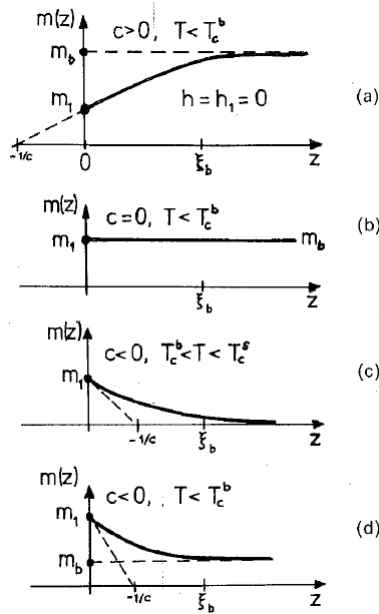
Figure 5.1: *Order parameter profiles of the ordinary (a), special (b), surface (c) and extraordinary (d) transition within the mean-field or Landau approximation. ξ_b is the bulk correlation length.[40]*

and J between all other nearest neighbour pairs, it can be shown that [37][38][39]

$$c = \frac{1 - 2(d-1)\gamma}{a},$$
(5.1.2)

where d is the dimensionality of the system and a is the lattice spacing. In mean field theory, the spontaneous magnetisation , $\phi_1(z)$ is linear in z for small z and extrapolates to zero at $z = -c^{-1}$ as is illustrated in fig. 5.1. As such, c^{-1} is called the 'extrapolation length' in the literature and is denoted λ. A positive λ refers to a system whereby the spin field $\mathbf{s_z}$ in the ordered phase would vanish if it were linearly extrapolated a distance λ outside the surface of the system, or in other words the order decreases as the surface is approached. As such, the extrapolation length effectively determines the range of the surface effects [35]

The different transitions are shown as cross-hatched lines on the phase diagram of fig. 5.2. The ordinary transition corresponds to ordering at the bulk transition temperature T_c . This occurs above the point P, which corresponds to $c = 0$ for

the infinite system and $c > c^*$ for the semi-infinite system. The 'surface' transition describes those transitions for which T_c^{MF} in the surface exceeds that in the bulk and the surface orders spontaneously at a higher temperature than the bulk. This corresponds to the phase boundary PQ. As the temperature is lowered below this surface-ordering temperature, the bulk undergoes a second order transition in the presence of the ordered surface, termed the extraordinary transition[35]. Finally, the case $c = 0$ corresponds to an enhanced surface interaction between surface spins (their eq1.2) which is not quite strong enough to split off a surface phase. For this system, the system orders at the bulk transition temperature, *but* the critical exponents and correlation function differ from those of the ordinary transition. LR call this the $\lambda = \infty$ transition, corresponding to the extrapolation length being infinite. Bray however disagrees with this nomenclature, since extrapolation length has no meaning outside of mean field theory, where in the vicinity of the transition there are fluctuations on all length scales. They also reassign the transition to $c = c^*$, due to the disagreement with the mean field value, as illustrated by the work of Binder and Hohenberg (1974). In this work, a high series expansion was performed on the semi-infinite 3D Ising model and the behaviour of the critical exponents was determined as a function of c. It was found that the existence of the surface phase for this case requires$\Delta > \Delta_c \simeq 0.6$, as opposed to the mean-field value of$\Delta_c = 1.4$. Bray assigns the phase transition associated with this reassignment of c the 'special' transition. This reassignment agrees with Lubensky and Rubin's later work [35], as shown in fig. 5.2.

The qualitatively different magnetisation profiles corresponding to the differently-ordered phases are shown in fig. 5.1. For the case whereby the mean field (MF) at the surface is smaller than in the bulk, there is an ordinary transition from the disordered state to a state with a magnetisation profile as depicted in (a), which is valid for $\lambda^{-1} > 0$, $t < 0$. For the case whereby the mean field on the surface is equal to that in the bulk, the $\lambda = \infty$ transition leads to the flat magnetisation profile of (b).
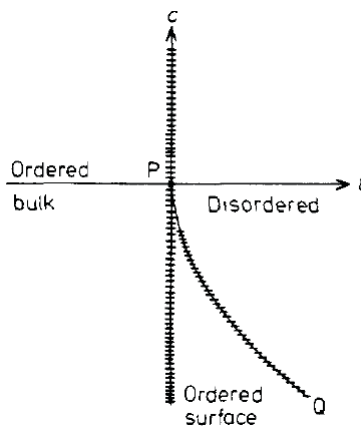
Figure 5.2: *Phase diagram as a function of c and t for $h_1 = 0 = h$. P is at the point $c = 0$ for the infinite problem and $c = c^*$ for the semi-infinite problem. The shape of the line PQ near P is $c \sim t^{1-\nu}$ or $c - c^* \sim t^{1-\nu}$ for infinite and semi-infinite problems respectively. Cross-hatched lines represent the phase boundaries as described in the text.[35]*

For $\lambda^{-1} < 0$, as the temperature is decreased past the surface transition temperature, the surface orders and the state has the magnetisation profile as shown in (c), with an exponential decay of the magnetisation into the bulk. As the temperature is then decreased further, the extraordinary transition occurs between (c) and (d), whereby the bulk orders in the presence of the surface order.

At the critical value of coupling on the surface, $J_s = J_{sc}$, at which the special transition occurs, one has simultaneous criticality of 2D surface layer correlations and bulk 3D correlations [41]. All of these behaviours are of particular interest since they have a close relation between critical wetting and prewetting phenomena[42] which shall be investigated later.

5.2 Interface Delocalisation Transitions: Wetting

Wetting was originally studied in terms of a lattice-gas picture but has also been applied to magnetic systems. Surface-induced disorder transitions (SID's) were also investigated, but initially the similarity to wetting was not realised. The SID transition will be covered in the next section, but we begin the introduction to interface delocalisation transitions with the wetting transition.

The wetting phenomenon originates from the wall, or surface, preferring a state that is different from the bulk state. As a parameter is changed, such as temperature in the magnetic picture, the preference at the surface can overwhelm the state dictated by bulk effects and the surface-preferred state that is nucleated at the wall can diverge into the bulk. Wetting requires the near-degeneracy of the phases involved, such that the energy cost of the surface-preferred state diverging into the bulk is small compared to the energy gain associated with the surface.

The preference of one magnetic state over another at the surface is artificially forced using a surface magnetic field h_1. The system is prevented from taking this surface-preferred state throughout by another magnetic field h applied to the bulk which is orientated differently (oppositely in the case of the Ising mode) from h_1. As such, a domain wall is set up between the surface and bulk magnetic states and it is the movement of the interface length, or rather the distance from the surface to the wall, that can lead to wetting.

Diehl [40] analyses the form of a Landau model that gives rise to wetting. The Hamiltonian of the system is written in terms of a surface and bulk term:

$$\mathcal{H}(\phi) = \mathcal{H}_b(\phi) + \mathcal{H}_s(\phi), \tag{5.2.1}$$

which are defined with respect to lagrangian functions:

$$\mathcal{H}_b(\phi) = \int_V dV \mathcal{L}_b(\phi, \delta\phi) \tag{5.2.2}$$

and

$$\mathcal{H}_s(\phi) = \int_S dS \mathcal{L}_s(\phi, \delta\phi), \tag{5.2.3}$$

where $\delta\phi$ is shorthand for $\partial\phi/\partial z$. The order parameter $m(z) =< \phi(z) >$ is approximated by the function that minimises the Hamiltonian. In this context, Diehl[40] assumes a form with

$$\mathcal{L}_b = \frac{1}{2}(\nabla\phi)^2 - U(\phi), \tag{5.2.4}$$

and $\mathcal{L}_s = \mathcal{L}_s(\phi)$, with no dependence on $\delta\phi$. $U(\phi)$, the potential, and $\mathcal{L}_s$, include possible bulk or surface magnetic field terms (such as the h and h_1 referred to previously). In this case, the problem applied to a semi-infinite system is extremalised by

$$\nabla^2 m(z) = -U'(m) \tag{5.2.5}$$

where the prime denotes differentiation by the argument, subject to the generalised boundary conditions for semi-infinite systems

$$m'(z) = \mathcal{L}'_s(m_1) \tag{5.2.6}$$

$$\lim_{z\to\infty} m(z) = m_b \tag{5.2.7}$$

$$\lim_{z\to\infty} m'(z) = 0, \tag{5.2.8}$$

where m_1 is the surface layer magnetisation and m_b is the bulk magnetisation,
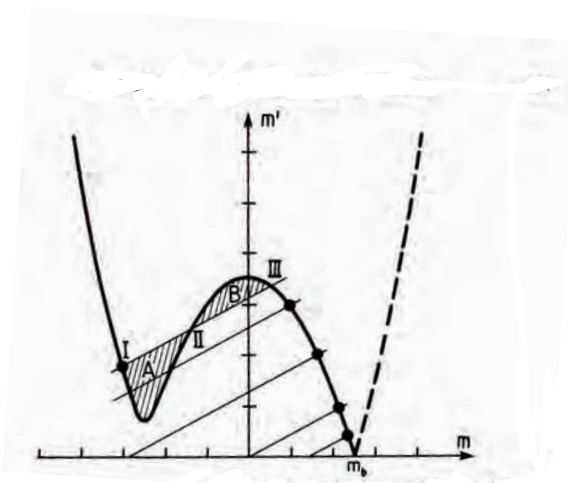
Figure 5.3: *Graphical solution of eq. 5.2.10. The solutions m_1 giving the surface free energy f_s are marked by full circles. The broken curve is $-m'$ since for $m > m_b$ one must take the negative sign of the square root $(2\Delta U)^{(1/2)}$. From [43].*

defined to be the magnetisation at the maximum of U. The condition for extrema, 5.2.5, can be rewritten using energy conservation as

$$m'(z) = \pm \left(2[U(m_b) - U(m)]\right)^{1/2},$$
(5.2.9)

where the difference $U(m_b) - U(m)$ is the bulk energy required to change the bulk magnetisation at constant temperature from m_b to m, or in other words the energetic cost of having a state in the bulk that is not a ground state of the bulk, a result of the presence of a domain wall. The extrema condition subject to the first boundary condition 6.2.14 can be written, by eliminating m', as

$$\mathcal{L}'_s(m_1) = \pm[2\Delta U(m_1; m_b)]^{1/2}.$$
(5.2.10)

The functions m' and $\mathcal{L}_s$ versus m are plotted in fig. 5.3 as per [40][43], so that the intersections of the two curves are solutions to the extrema condition subject to

88

boundary condition 6.2.14. $\mathcal{L}_s$ is plotted for a given c value, for various positive and negative values of h. The free energy expression, which can be shown to be given by

$$f_s = \int_0^\infty dz (m')^2 + \mathcal{L}_s(m_1), \tag{5.2.11}$$

is used to determine which of the multiple solutions accessible when h_1 is strong enough and negative correspond to the minimum energy equilibrium phase. Note that the free energy is a function of the variation of the magnetisation in the system, which can be thought of as the cost of a magnetic domain wall, and a contribution from the surface interaction $\mathcal{L}_s$. The free energy can also be written in a form more suited to analysis via the graph:

$$f_s = \mathcal{L}_s(m_b) + \int_{m_1}^{m_b} dm [(2\Delta U)^{1/2} - \mathcal{L}'_s]. \tag{5.2.12}$$

Minimising the free energy amounts to minimising the second term, since the first term $\mathcal{L}_s(m_b)$ is constant for fixed h, τ, h_1 and c. Thus, the free energy is minimised by minimising the second term, which amounts to minimising the difference between the shaded areas A and B of the graph. Decreasing a negative h_1 increases area A and decreases B until the areas are equal, at which point a first order transition occurs from intersection III being the stable solution to I being the stable solution. The profile of the solution corresponding to intersection III is like that of the ordinary transition. However, for sufficiently large $c > 0$, m_1 may be negative, and the magnetisation profile may thus have an inflection point, as shown in fig. 5.4(a). The intersection solution I can be seen in fig. (b) and is our first illustration of a wet system, with l_W growing without bound.

Complete wetting concerns a first order transition, whereby the thickness l_w of the wetting layer increases *discontinuously* from a finite microscopic value to an infinite
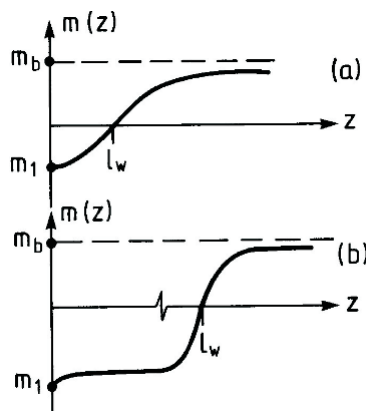
Figure 5.4: *Mean-field order parameter values for T above (a) or below (b) the wetting tempera-ture. The profile in (b) corresponds to the solution marked I in fig. 5.3.[40]*

(macroscopic) one. Other wetting phenomena also exist, which are applicable to our magnetic studies; *critical wetting* describes the diverging of l_w continuously and *prewetting* refers to the transition from a thin to thick, but finite, layer. It has been a point of contention as to whether the critical wetting phenomenon should be referred to as a phase transition since it does not involve a discontinuous jump in the parameter l_w, nor its increase from a zero value.

Nakanashi and Fisher used Landau theory to study the semi-infinite n-vector model with bulk and surface fields h and h_1 included. They show that the prewetting criticality and pure surface enhanced transitions are essentially the same phenomena, connecting the diagrams in fig. 5.5. Their work effectively unfolds figure 5.2 at the 'special' surface multicritical point P into four-dimensional thermodynamic space, in terms of the additional magnetic field variables h and h_1. The resulting phase diagrams are shown in fig. 5.6. Figure (a) of 5.6 was also reproduced by Lipowsky and Speth [44] using a mean field treatment of the Landau free energy functional defined by

$$F\{\phi\} = \int d^{d-1}\rho \int_0^\infty dz \left[\frac{1}{2}(\Delta\phi)^2 + f(\phi) + \delta(z)f_1(\phi)\right], \qquad (5.2.13)$$

where ρ describes the Cartesian components parallel to the surface, z is the coordinate perpendicular to the surface, and ϕ is the scalar field that describes the order parameter ϕ. $f(\phi)$ governs the bulk properties and $f_1(\phi)$ is the surface term that contains the influence of the surface on the order parameter field and is activated only for the surface layer $z = 0$ via the delta function. The $(\Delta\phi)^2$term is related to the energy cost of the system not taking the ground state of the bulk up to the surface. The functional presupposes short-range interactions. For the wetting case, the functions take the forms

$$f(\phi) = -\frac{\tau}{2}\phi^2 + \frac{\upsilon}{4}\phi^4 - h\phi \tag{5.2.14}$$

and

$$f_1(\phi) = \frac{1}{2}g\phi^2 - h_1\phi, \tag{5.2.15}$$

where the temperature-dependence is assumed to be dominated by the Landau coefficient a present on the bulk contribution to the free energy, and the remaining coefficients are taken to be temperature-independent. τ is the reduced temperature defined as $T_c - T$ such that the ordered phase corresponds to a positive reduced temperature and h is proportional to the bulk magnetic field. The effect of the free surface is taken into account in terms of two contributions; the first is the modified interaction between spins on the surface, which is represented by than incremental surface field g in the continuum model. Only surface enhancement, corresponding to $g > 0$, is considered. The quantity is also our inverse extrapolation length described earlier on in the chapter. The second contribution describes the affinity of the surface for the surface phase and is described by a local chemical potential or surface field h_1.
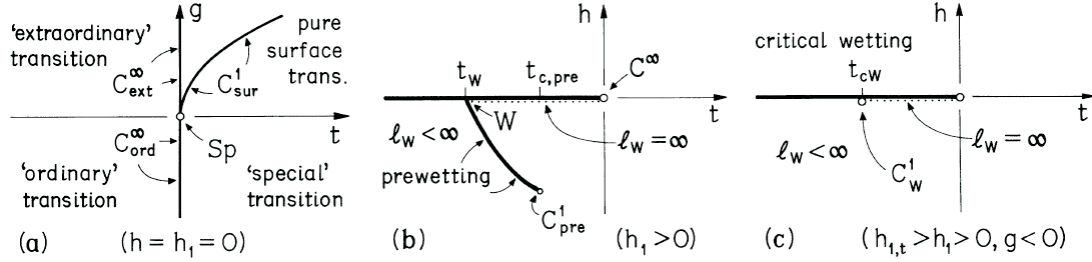
Figure 5.5: *Surface phase diagrams in terms of $t \propto T - T_c^\infty$, surface enhancement g, bulk field h, and surface field h_1 [42].*
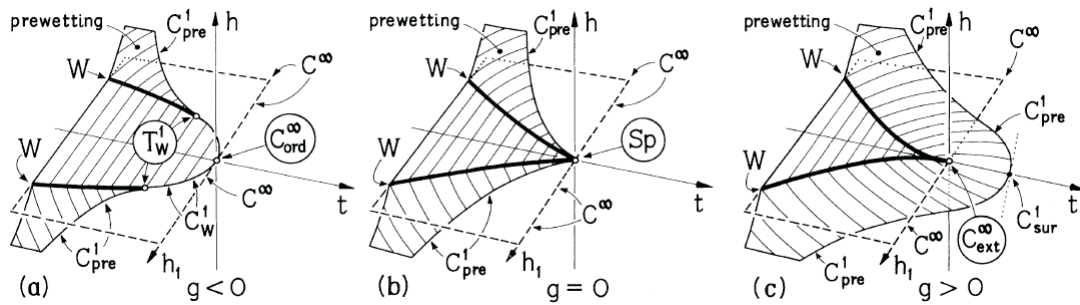
Figure 5.6: *Sections of the global surface phase diagram for various surface enhancements g, showing wetting lines, W; critical points, C_W^1, C_{pre}^1, $C_{surface}^1$, C_∞; and multicritical points (encircled labels). Superscripts ∞ and 1 distinguish transitions in which, respectively, both bulk and surface or only surface criticality occurs.[42].*

To describe the phase diagrams of figures 5.5 and 5.6 in more detail, let us go back to 5.5, where we are already familiar with diagram (a), whereby no magnetic field is present in the bulk or on the surface. Figures (b) and (c) deal with cases in which the surface magnetic field h_1 is present and positive. We consider the diagrams with respect to the Ising model for simplicity. The presence of h_1 forces the surface to take up an order parameter on the surface which permeates the entire system. If we then consider the case of $h \to 0_-$ such that the bulk magnetic field tends towards zero *but* is oppositely-directed from the field on the surface, we have the interesting case in which the surface takes on a spin up phase but deep into the bulk the system is forced to take the spin down phase. As such, the system possesses a domain wall between the phases which moves as the temperature is increased and the energetics of h that order the bulk to have spin down becomes less dominant. Eventually, the bulk disorders and the surface phase nucleated/seeded by h_1 extends across the entire system. The bulk phase is thereby *wet* by the surface phase. It is this case of $h \to 0_-$ and $h_1 > 0$ that we are therefore interested in and we shall now discuss the graphs with this path in mind.

To begin, we relate the case of $h_1 = h = 0$ in fig. 5.6(c) to 5.5(a). For supercritical surface enhancement $g > 0$, the pure surface transition C^1_{sur} of figure 5.5(a) lies on the prewetting line where it meets the t-axis, at t_c^∞. For the $g = 0$ case, the special point defined by Bray *et al*, labelled SP in fig 5.5(a), is located in 5.6(b), where the extraordinary and surface transitions merge into this single point. What's more, the SP is the common terminus of the wetting and pre-wetting lines. For $g < 0$, the special point is replaced by the critical point for the ordinary transition C^∞_{ord}. This point is more singular than the bulk-driven transition C^∞.

The interesting physics occurs for the case of $h_1 \neq 0$. The lines c^∞ in all three graphs of 5.6 for this parameter range are the bulk criticality lines which forces the free energy at the surface to have singularities. As t crosses these lines, the bulk orders. For different ranges of h_1, different types of wetting phenomena occur. In

addition to the existence of prewetting and wetting transitions, there is a new surface multicritical point T_W^1 that is not present for $g \geq 0$, where the first order wetting line W turns abruptly into the critical wetting line C_W^1. This point is termed the wetting tricritical point. For supercritical surface enhancement, for a certain range of h_1 the bulk orders in the presence of an ordered surface in a similar way to the extraordinary transition.

The equivalence of these diagrams with those of 5.5(b) and (c) thus depend on the value of h_1. fig. 5.5(c) is equivalent to 5.6(a) for $0 < h_1 < (h_1)_{critical}$, before the wetting line W appears. 5.5(b) is equivalent to both $g < 0$ and $g > 0$ of the 3D graphs; for $g > 0$, the graphs are equivalent for all $h_1 > 0$, but for $g < 0$, it coincides only for $h_1 > (h_1)_{critical}$.

We now consider these graphs in the context of magnetic systems for $h \rightarrow 0_-$. Increasing the temperature from $t = 0$, l_W begins as small and finite, since the bulk order is dominant and perseveres towards the surface layers. For the case of subcritical surface enhancement with $0 < h_1 < (h_1)_{critical}$, as the temperature increases the system goes through a critical wetting transition, at which point the thickness diverges continuously and the surface phase wets the bulk phase as the bulk becomes less ordered. For both subcritical enhancement for $h_1 > (h_1)_{critical}$ and supercritical enhancement for any $h_1 \neq 0$, as the temperature is increased the system instead undergoes a prewetting transition and the thickness of the surface phase jumps discontinuously from the small finite value to a large but nevertheless still finite value. For supercritical enhancement and large enough h_1, the prewetting jump to a larger thickness can occur at a temperature distinctly higher than the bulk ordering temperature, which in other words describes a prewetting jump occurring at a temperature at which the bulk has already disordered. The complete wetting transition in fact only occurs in the limit $h \rightarrow 0$ such that the difference in free energy between the surface and bulk phases become not just similar but equal and l_w can diverge completely.

We must now be more specific with respect to the definition of the thickness of the wall l_W. It is in fact possible for a system to possess a variable that is both macroscopic, diverging with system size, and possess a length scale that increases continuously. The effect is due to the thermal distribution associated with the interface length. Consider, for example, a power law distribution $P(l_W) \sim 1/l_W^\alpha$. We define the moments $\langle l_W \rangle^y$ by

$$\langle l_W \rangle^y = \lim_{a \to \infty} \int_1^a P(l_W) l_W^y d(l_W). \tag{5.2.16}$$

One can then envisage a case where the power law exponent α goes through a value as a function of, for example, temperature, such that the mean, corresponding to the case of $y = 1$, is finite, but the second moment is divergent. The second moment, a measure of the standard deviation of l_W from the mean value, can be thought of as a measure of the fluctuations of the wall from the mean width. Care must be taken with respect to the definitions of l_W in the papers as to whether the measurement refers to the mean value of the interface width or the fluctuations associated with it.

Lipowsky and Speth [44] also went on to solve for the magnetisation profile for both the wetting case and SID case, which we shall be discussing next. The profiles are shown in fig. 5.7 and illustrate the comparison between the two types of interface-delocalisation transition.

5.3 Surface-Induced Order-Disorder Transition; A Form of Wetting

Interface localisation-delocalisation transitions can occur for systems in which the bulk undergoes a first order disordering transition but the near-surface instead un-
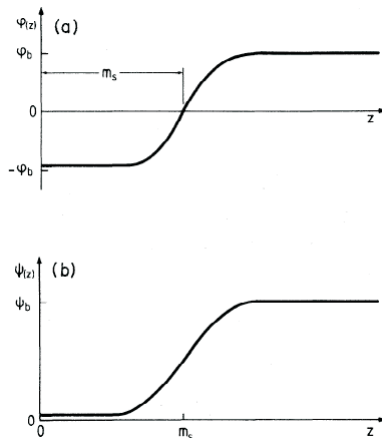
Figure 5.7: *(a)Order-parameter profile $\phi(z)$ for $\tau \geq \tau_w$ near the critical wetting transition. ϕ_b is the bulk value of the order parameter and m_s, the distance of the interface from the surface, is the coverage. $\phi(z = 0) + \phi_b \to 0$ and $m_s \to \infty$ at the wetting transition. (b) Order-parameter profile $\psi(z)$ for $a \leq a^*$ near the SID transition O_2. ψ_b is the bulk value of the order parameter. $\psi(z = 0) \to 0$ at the SID transition [44].*

dergoes a continuous disordering transition. A magnetisation profile can then be set up between the disordering surface and ordered bulk and it is the behaviour of the interface length associated with the profile that can be special - it can become delocalised and diffuse near the bulk ordering temperature, and this is considered a wetting transition. As such, the bulk ordering transition at which both bulk and surface become simultaneously disordered on approaching the temperature from below can be considered to be the divergence of the interface into the bulk. The phenomenon is an unusual form of wetting since there is no requirement for externally-applied fields h or h_1; it is the altered coupling at the surface alone that mediates the transition. The transition and can manifest in surface quantities behaving continuously even though the bulk undergoes this discontinuous transition[45][46]. Lipowsky *et al* in particular showed that for $d = 2$ in the presence of a bulk first order transition, the surface order parameter *always* behaves continuously [44]. The continuously decreasing magnetisation at the surface is made possible by the interface moving into the bulk and correspondingly the surface being shielded from the magnetic field provided by the ordered bulk as the thickness of the interface increases.

Lipowsky and Speth [46] showed that, instead of the requirement for external fields h and h_1 as in wetting, the phenomenon can be mediated solely by a non-zero value of the first order invariant a_1 of a free energy of the surface of the form

$$f_1(\psi) = \frac{1}{2}a_1\psi^2 - H_1\psi, \tag{5.3.1}$$

where the Landau free energy functional of the system is given by 5.2.13 where $f(\phi)$ which governs the bulk properties is to take a form that leaves the bulk with a first order transition from disorder, $\phi = 0$, to order, $\phi = M_B > 0$. One of the simplest models they solve for which the magnetisation profile $M(z)$ can be solved analytically is defined by the surface function 5.3.1 and the bulk function

$$f(\psi) = -H\psi + \frac{1}{2}a\psi^2 - \frac{1}{3}b\psi^3 + \frac{1}{4}c\psi^4, \tag{5.3.2}$$

with $b, c > 0$ and where a has the dominant temperature dependence. The cubic invariant forces a first order transition.

Lipowsky and Speth [44] showed that this free energy functional describing the SID transition can in fact be mapped onto that of the wetting transition using an appropriate coupling constant transformation. The resulting figure, obtained from fig. 5.6(a) using this transformation, is shown in fig. 5.8. The SID transition occurs for $H = H_1 = 0$, where the a axis cuts the coexistence plane of the wetting case, $h = 0$, $\tau > 0$.

Relating the coefficients to physical parameters, a_1 represents the enhancement or 'repression' of surface coupling, with respect to microscopic interaction parameters, in comparison with the bulk coupling. It is this term that leads to the wetting-type phenomenon. In particular, for the Potts model, $a_1 > 0$ for $J_1 << J$, corresponding to surface interaction repression, and $a_1 < 0$ when $J_1 >> J$, corresponding to surface
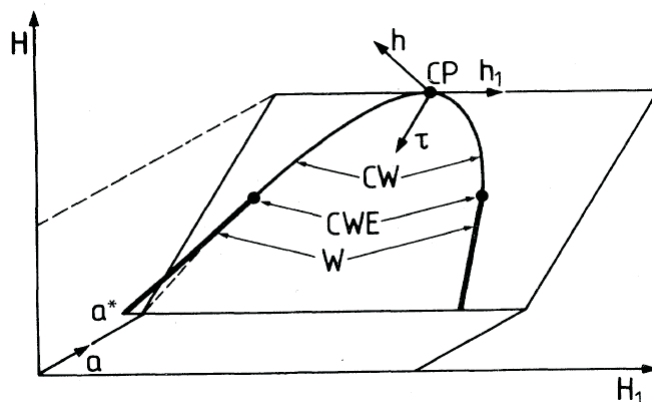
Figure 5.8: *SID phase diagram obtained from the wetting phase diagram in fig. 5.6(a) using a coupling constant transformation. The SID transition occurs for $H = H_1 = 0$, i.e. where the a axis cuts the coexistence plane [44].*

interaction enhancement. H and H_1 are *both* taken to be positive, as opposed to the case of wetting where the external fields are considered to be oppositely-directed to one another such that a different phase is preferred on the surface from the bulk and an interface is therefore automatically existent. In this way, the same phase is preferred on the surface as in the bulk and so the interface may only exist for other reasons. Specifically in this case, it is the a_1 coefficient that can cause an interface to exist in this model, which represents the size of the departure of the surface interaction strength from the bulk value

The phase diagram as a function of a and a_1 is shown in fig. 5.9, where the bulk first order transition occurs at $a = a^*$ which corresponds to the bulk transition temperature $T = T^*$. The temperature deviation is therefore proportional to $\delta a \equiv a - a^*$.

At the bulk transition, several transitions are possible, depending on the value of a_1. There are 2 extraordinary transitions E^+ and E^- that occur if one approaches the bulk transition from a higher or lower temperature respectively. For the Ising model, where the bulk orders continuously, these transitions are identical, and there is only one instead of two ordinary transitions.

$\bar{s}$ is a multicritical point.The dashed line separates two metastable profiles, and
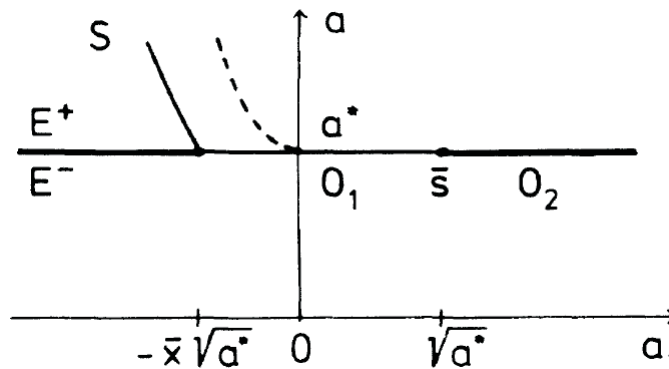
Figure 5.9: *Global a, a_1 phase diagram for for semi-infinite system exhibiting a first-order bulk transition at $a = a^*$ corresponding to the temperature $T = T^*$. The different types of transitions are denoted by S, E^+, E_-, O_1, $\bar{s}$ and O_2. The dashed line is a line of metastability [46]*

one of these becomes the equilibrium profile at the phase boundary S. For the Ising case, whereby the bulk orders continuously, the phase boundary is instead a continuous transition and so the transition line S and the dashed line of metastability are identical.

In both models considered, the order parameter at the surface, M_1, is continuous at E^- and E^+, discontinuous at O_1, and goes to zero continuously at $\bar{s}$ and O_2, even though the bulk orders continuously.

The order parameter profiles are given in fig. 5.10. Profiles (b) and (c) exhibit a monotonic increase or decrease respectively in magnetisation from the surface to the value of the bulk order parameter M_B. Whether there is an increase or decrease depends on whether the surface interaction is repressed or enhanced respectively compared to the bulk. The magnetisation profile exhibits a point of inflection for the cases of (a) and (d) and one can therefore define the existence of an interface at $\hat{l}$ and $\hat{\hat{l}}$ respectively. Unlike the length scale of the variation in (b) and (c), which is limited to the value of $1/(a^*)^{1/2}$, the interface of (a) and (c) can delocalise.

The order parameter profile of fig 5.10(a) is possible at temperatures well below the bulk transition temperature. This is due to the reduced and altered relative numbers of neighbours on the surface as a result of the termination of the material,

which in terms of the exchange energies associated with the transition, amounts to a large 'anti-'enhancement at the surface. In the magnetic picture, the anologue to the alternation of the exchange coupling is the reduction in magnetic bonding such that the spins are less tightly bound to particular directions on the surface layer than in the bulk. The surface then acts as a natural nucleus for the disordered phase in temperature ranges where the bulk is ordered. An interface can then exist in the presence of an ordered bulk which favours disorder over order, resulting in a surface region with disorder existing. The width of the interface depends on the bulk correlation length.

As the temperature is increased towards the bulk ordering transition temperature T_0 the interface moves into the bulk, growing from a micro to a meso and even macroscopic behaviour. If short-range interactions dominate on the surface, then one would expect the temperature dependence of the wetting layer to follow a logarithmic law[47]:

$$L(t) = \xi_d \ln \frac{1}{t} \tag{5.3.3}$$

where ξ is the correlation length in the disordered phase and remains finite at all temperatures.

We now report findings of x-ray evanescent scattering studies of a Cu_3Au surface which have the hallmarks of an order-disorder transition. The system possesses an interface between a disordered surface phase and ordered bulk phase that is pinned to the surface, but whose interface length increases as the bulk ordering temperature is approached from below and eventually diverges continuously into the bulk.

The experiments we discuss are those performed by Dosch, Mailander *et al* [48][45]. Cu_3Au is a binary alloy consisting of a superlattice structure as shown in fig. 5.11. The structure can be described as a simple cubic lattice decorated on
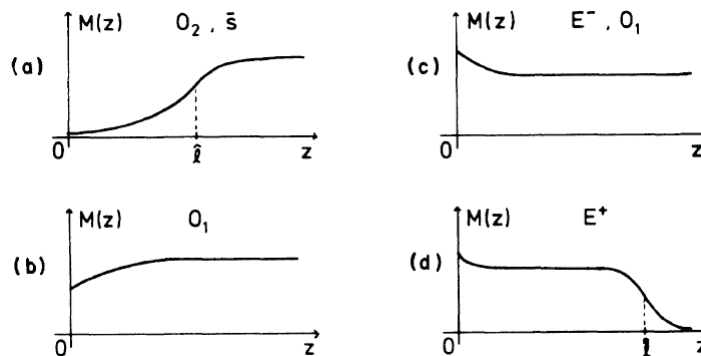
Figure 5.10: *Generic shapes of the order-parameter profile $M(z)$: (a) at the transitions O_2 and $\bar{s}$; (b) and (c) at the transitions O_1 and E^-; (d) at the transition E^+. Near O_2, $\bar{s}$ and E^+ there is an interface at $z = \hat{l}$ and $z = \hat{\hat{l}}$ respectively [46].*

each site with FCC (tetrahedral) units each comprising of 3 Cu atoms and 1 Au atom. As the temperature is lowered, the randomly-distributed Cu and Au exchange sites take the ordered form shown in fig. 5.11, leading to the definition of the Bragg-Williams order parameter

$$m = \frac{3}{4}\left[\frac{r_\alpha - c_{\text{Cu}}}{1 - c_{\text{Cu}}}\right] + \frac{1}{4}\left[\frac{r_\beta - c_{\text{Au}}}{1 - c_{\text{Au}}}\right], \tag{5.3.4}$$

where r_α and r_β are the fractions of correctly-occupied sites which range from 1 in the ordered state to c_{Cu} and c_{Au} in the disordered state, where c_{Cu} and c_{Au} are the concentrations of Cu and Au respectively. One can compare the system to a magnetic anologue modelled by an Ising model, by assigning an up spin to Cu sites and a down spin to Au sites. The ordered structure corresponds to modelling the system with a nearest neighbour AFM coupling plus an FM next nearest neighbour coupling, and this competition between interactions leads to the first order character of the ordering transition in the bulk. In comparison, the surface begins to order at the same temperature T_0 *but* as a continuous transition, as can be seen in fig. 5.13. It has been suggested by Dosch and coworkers [45][48] that this behaviour is a realisation of the surface-induced-order-disorder transition brought about by delocalisation of
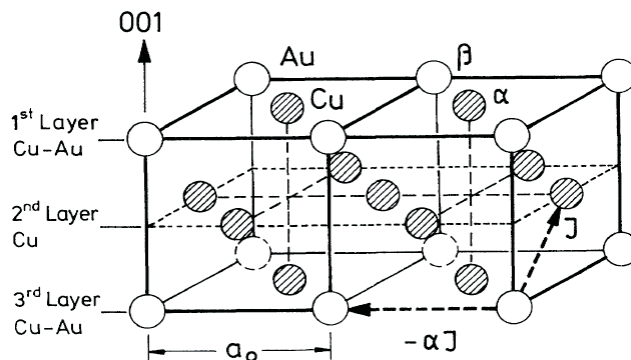
Figure 5.11: *Structure of the ordered Cu_3Au crystal. $a_0 = 3.75\text{Å}$. [45].*
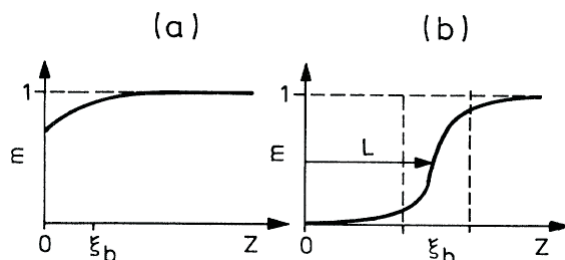
Figure 5.12: *Long-range order profiles close to the free surface. $z = 0$ denotes the surface. (a) $T \ll T_0$, onset of surface disorder; (b) $T < T_0$; disordered surface layer with thickness L. The thermal roughness of the interface is ξ_b[45].*

the order-disorder interface.

The key difference between order-disorder transitions at bulk first order transitions and ordinary bulk-ordering transitions is the size of the altered bonding on the surface - For the magnetic ordering case, the altered bonds on the surface are of the order of the size of J. In contrast, the case of Cu_3Au involves much higher differences between the bulk and surface coupling energies, being the atomic exchange energy that comes about from large thermal fluctuations. As such, the stabilisation of disorder on the surface is much more pronounced, resulting in the width of the disordered phase existing at lower temperatures and perhaps leading to the interface moving further into the bulk.

We turn our attention to the experimental signatures, which shall be helpful when we analyse similar results in our chapter concerning unusual phenomena associated
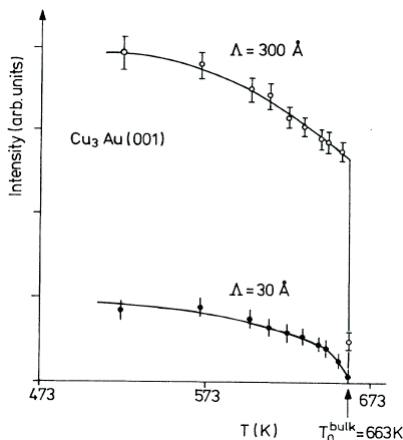
Figure 5.13: *Temperature dependence of the evanescent superlattice intensity at two different scattering depths $\Lambda = 30\mathring{A}$ and $\Lambda = 300\mathring{A}$ (The solid lines are a guide for the eyes).[45].*

with the near-surface region of uranium dioxide. The bulk ordering is characterised by the gaussian contribution of the integrated intensity distribution of fig. 5.14, thus indicating long range correlations are present. The additional diffuse contribution, which is a small, broad contribution, is attributed to short-range order in the surface.

The intensity as a function of reduced temperature t for depths ranging from 17 to 500 Åis plotted on a double-logarithmic scale in fig. 5.15. The intensity dependence on temperature is relatively weak far away from T_0, but becomes marked close to T_0, where it takes on a power-law behaviour described by

$$I_\Lambda(t) \propto |t|^{2\beta_\Lambda}. \tag{5.3.5}$$

The solid lines on the figure are fitted by this power law, and the value of the slope $2\beta_\Lambda$ is found to increase with decreasing depth by the relationship

$$\beta_\Lambda = \frac{\xi_m}{\Lambda}. \tag{5.3.6}$$

This can be seen in fig. 5.15, where the data points all fall on a straight line within the dashed error bars. For large depths, the exponent tends towards zero, which is

103
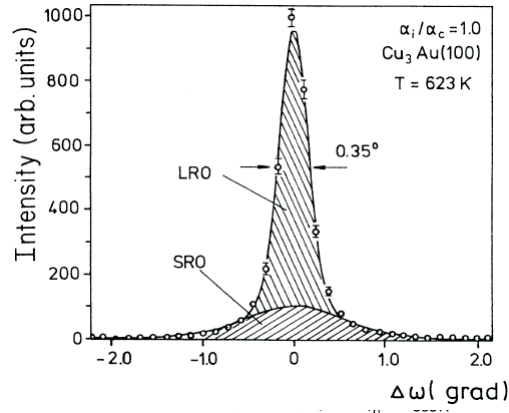
Figure 5.14: α_f-integrated intensity distribution around (100) superlattice peak at $T = 623K < T_0$ as measured in an ω scan for $\alpha_i/\alpha_c = 1.0$. The solid lines are the least squares fit to the data. The half-width of the LRO contribution is $0.35\deg$.[45].

typical of first order transitions. Thus, the data exhibits a smooth transition with depth from the continuous behaviour with temperature of the surface region to the discontinuous ordering with temperature of the bulk.

We shall refer to these results when discussing how to interpret the experimental data for uranium dioxide, since the results are similar, suggesting that an interface delocalisation may offer a reasonable picture of the behaviour.
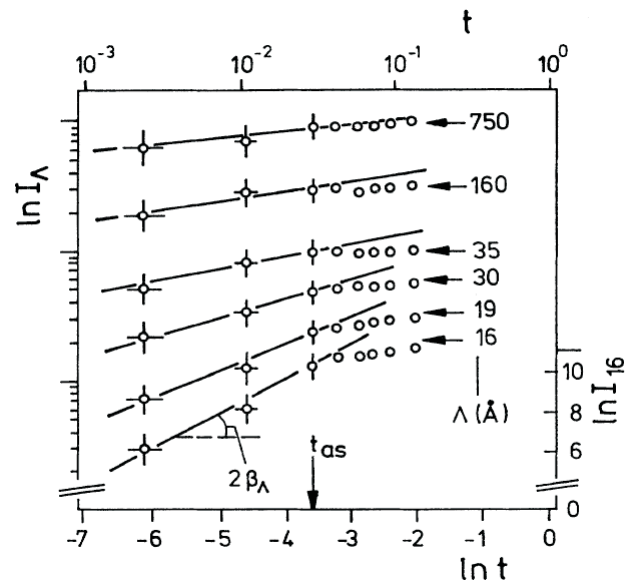
Figure 5.15: *Evanescent superlattice intensities I_Λ associated with scattering depth Λ as a function of the reduced temperature $t \equiv (T_0 - T)$ on a double-logarithmic scale. t_{as} denotes the onset of the asymptotic regime, $2\beta_\Lambda$ denotes the near-surface 'critical exponent'.[45].*

Chapter 6

MAGNETIC SURFACE RECONSTRUCTION INVOLVING NEW ORDER

We now present the first study of the thesis, in which a surface reconstruction involving new order is shown to be a theoretically possible phenomenon.

The study of Uranium Dioxide that will be presented in the next chapter is an illustration of how multiple-q magnets can compensate for energy lost at the surface; the relative spin densities corresponding to the different magnetic orders in the bulk are altered as the surface is approached, such that the system moves towards the *extinction* of an order in the near-surface region. For the case of Uranium dioxide, whereby the system takes a triple-q state in the bulk at low temperature, there is not a possibility of new order being introduced at the surface since any new magnetic order would not be compatible the triple-q state that already exists. Specifically, no new order can be introduced since there are no dimensions in real space available to the system in which to superimpose another magnetic order whilst maintaining the length of the spin everywhere.

We therefore propose a new model, in which there is potential for the introduction of new order at the surface. This is a completely novel concept, as previous literature dealing with magnetic order only concerns order identical to that in the bulk. The properties of the magnetic domain make-up of multiple-q systems allow for the appearance of order on the surface that is independent from the bulk order, since

106

each magnetic T-domain possesses *different* translational symmetries along a given direction.

Ordinary magnets do not have this property as was discussed in section 4.1; the S domains that are the only type that exist for ferromagnets and bipartite magnets can be distinguished between solely according to the direction of the spins within the domains, as opposed to any underlying difference in the symmetry. As such,these domains do not correspond to different order with respect to Bragg spots. Ordinary magnets refer to ferromagnets, bipartite magnets and chiral magnets, since they do not break the point group symmetry of the Hamiltonian.

Domains found in multiple-q magnets that take up single-q states can be equivalently generated by rotating the whole lattice-plus-spin system.[1] The resulting single-q domains for a type-1 FCC lattice are shown in (a) - (c) in fig. 6.2. As this picture illustrates, these different domains correspond to *different* Bragg spots and hence possess different translational symmetries which is *not* the case for ordinary magnets. The complete set of domains present in the system can then be generated from the figure by rotating the spins solely in spin space. This is a *continuous* symmetry for the case of the Heisenberg model, but in reality anisotropy effects such as spin-orbit coupling results in discrete rotations to degenerate states, such as those that leave the spins pointing along the crystallographic axes for example.

The property of the single-q magnet possessing domains of different underlying symmetry is crucial, as it allows us to envisage a material which favours one single-q state over another on the surface - it is the translational symmetry of the state in the direction parallel to the surface that leads to the state possessing different magnetic energies on the surface layer, and so the different magnetic domains present in a multiple-q system would be expected to react differently to a surface. If therefore the surface prefers a single-q state *different* from that present in the bulk, then

---

[1] Applying the term multiple-q to magnets that possess single-q states seems counterintuitive. In this thesis however, the multiple-q nomenclature refers to the potential for the magnet to take up more than one Bragg spot, due to the degeneracy present in the system.

it becomes feasible that the material may wish to move from the bulk-favoured single-q state to a different single-q state as the surface is approached, energy-costs permitting. As such, there may appear new order as the surface is approached, in the form of a second Bragg spot.

The reality of a material possessing a 'surface-hating' single-q T-domain in the bulk with a different single-q T-domain in close proximity energetically is actually completely feasible, as per discussions about bulk domain distributions of section 4.1. In terms of the mixture of domains in real systems, *bulk* considerations control the structural domain distribution, and consequently we would expect to find, in the absence of the surface reconstruction, a mix of the single-q domains on the surface, stabilised by energetics associated with the bulk distortion. The following chapter therefore models the behaviour of those domains that are not preferred by the surface, and we expect those that like the surface to remain at the surface, perhaps with some distortion of the domain walls between the styles of single-q as the surface is approached.

The style of reconstruction we propose in this chapter is particularly interesting as it presents the possibility of a phase transition that occurs at a temperature *below* that of the bulk magnetic ordering temperature. The bulk orders at a transition temperature T_N and this order penetrates to the surface, albeit with less magnitude due to the fewer magnetic bonds and hence ordering 'capability' present on the surface. This 'bulk' order increases in magnitude as the temperature decreases and the magnetic order overcomes thermal fluctations. We expect that, at a certain temperature,the bulk order parameter value at the near-surface has increased to a value whereby the system can benefit by possessing a different symmetry parallel to the surface from the bulk symmetry in the near-surface region. This second symmetry is an order parameter in its own right, appearing from zero to a finite value at a temperature T_2, as shown in fig 6.1. The order parallel to the surface can be quantified by the value of the intensity of the associated spin density in reciprocal
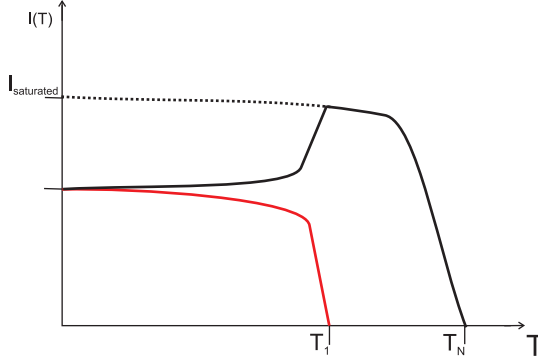
Figure 6.1: *Qualitative graph to show how order parameters associated with the different symmetries evolve as temperature is decreased.*

space. The increase in magnitude of the new order corresponds to a tilting of the spin orientation due to the superimposition of the two orders, and as such the magnitude of the 'old' bulk order decreases to compensate and maintain the spin length, as can be seen qualitatively in the figure. This will be discussed in more detail later.

There are 3 basic criteria that a system should have to allow our reconstruction. Firstly, we require the system to offer, under certain parameters, degeneracy between two states, such that a system can be 'tuned' using these parameters to exist near to the degeneracy. Frustrated systems offer this possibility. Secondly, we require the degenerate states to react differently to a surface. Finally, we require that the states are superimposed onto each other such that one can move gradually between the two phases without too high a domain wall energy cost. Thus one requires collinear spins, and a perpendicular superimposition in order that spin length is conserved.

The 'tuning' of the system away from degeneracy is often realised in real systems. On magnetically ordering to the single-q structure, magnetoelastic distortions occur that strengthen the bonds that gain energy and weakening those that loose energy. This further stabilises one domain over another in the bulk. The magnetoelastic distortion phenomenon however also results in vital complications. Unlike normal magnetoelastic phenomena, the distortion can be sizeable for single-q states (4.1) and as such the energy cost of superimposing one single-q state over another within the crystal could be too high. The distortion is also a severe modelling complica-
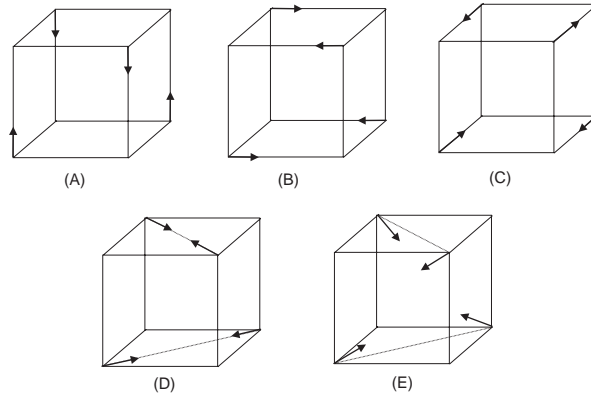
Figure 6.2: *Possible spin orientations of an FCC lattice antiferromagnet with nearest neighbour coupling (a) Single-q (x-oriented) (b) Single-q (y-oriented) (c) single-q(z-orientated) (d) Double-q (equal mixture) (e) triple-q.*

tion. As the phase changes character as the surface is approached, one expects the magnetoelastic distortions to also sympathetically change. The self-consistent determination of such distortions is beyond the scope of our investigation, and we merely point out that our investigation is in fact a worse case scenario: The sympathetic change of the magnetoelastic distortions on reconstruction would serve to stabilise further the reconstruction and so our results to show that the reconstruction exists are not negated by this effect, but in fact supported by them.

Magnetoanisotropic effects also present another problem to the reconstruction which involves non-collinear spin directions that vary in nature plane-to-plane. The anisotropy costs of such reconstructions could be large enough to prevent our reconstruction in some materials. We also ignore this complication in our investigation, and provide reasons as to why this is a valid effect to neglect later on.

6.1 Square Lattice Model

We investigate our proposal using a 2D square lattice with frustration, which can achieve all criteria for the reconstruction, yet is simple enough to study in detail. We shall show later on that this model is in fact equivalent to a FCC lattice with nearest neighbour coupling and so has immediate and important application to real

systems.

We employ the following simple model for the 2D square lattice:

$$H = J_\parallel \sum_{<jj'>_\parallel} \mathbf{S}_j.\mathbf{S}_{j'} + J_\perp \sum_{<jj'>_\perp} \mathbf{S}_j.\mathbf{S}_{j'} + J_2 \sum_{<jj'>_2} \mathbf{S}_j.\mathbf{S}_{j'}, \qquad (6.1.1)$$

which was solved for the bulk states in section 3.2.3, and we use the variable θ defined there for our work. $< jj'>_\parallel$ denotes nearest-neighbour bonds parallel to the surface, $< jj'>_\perp$ denotes nearest-neighbour bonds perpendicular to the surface and $< jj'>_2$ denotes second-nearest-neighbour bonds. The second-neighbour coupling is both crucial and sizeable in order to frustrate the system and to stabilise the multiple-q ground-states. We introduce $J_\parallel \neq J_\perp$ so that one can detune the system from degeneracy, a criteria for the surface reconstruction. This detuning models real systems as the distortion is naturally present via magnetoelastic effects, as discussed in the previous section.

6.2 Introducing a Surface

The main physical question addressed in the following sections is how the phase diagram of fig. 3.10 is modified by a surface. (we use the convention of adopting a surface in the vertical orientation, as defined in figure 3.9). A simple summing over bonds at this surface provides inequalities for the coupling parameter values for which the different states are preferred by the surface, and comparison to the phase space for the bulk indicates in which regions the surface prefers a different state from that taken in the bulk. Using the convention of section 3.2.3, the surface is taken to be parallel to the x-direction. We find that only in a region in which the bulk takes the state $\mathbf{k} = (k_x, k_y) = (0, \pi)$, or in other words the $\theta = 0$ state, is this condition satisfied, whereby the surface prefers either $(\pi, 0)$ or (π,π) depending on the particular coupling ratios. We therefore investigate a state of the type depicted

in fig.(6.3), assuming that each layer parallel to the surface, n, is characterised by a different value of the angle θ_n, which is allowed to vary freely. The figure illustrates a specific example corresponding to assuming that $\theta = \pi/2$ is preferred at the surface, and that there is a smooth, layer-by-layer evolution between these values. This corresponds to one of the solutions to the problem that we discuss below. However, for the time being we will allow, much more generally, the value of θ on each layer to vary independently. This amounts to assuming that within a given layer parallel to the surface there are no additional broken symmetries other than those present in the bulk phase diagram of Fig. 3.10.

In terms of our variable θ, the total energy per spin of the whole system is given by

$$E = J_{\parallel} \sum_{n=1}^{\infty} \cos 2\theta_n - J_{\perp} \sum_{n=1}^{\infty} \cos(\theta_n + \theta_{n+1})$$
$$-2J_2 \sum_{n=1}^{\infty} \cos(\theta_n - \theta_{n+1}) \tag{6.2.1}$$

and the mathematical task amounts to choosing the angles so as to minimise this energy.

Minimisation over θ_n provides the controlling equations which must be satisfied for all n:

$$\begin{aligned}
0 \;=\; & J_{\perp}[\sin(\theta_{n-1} + \theta_n) + \sin(\theta_n + \theta_{n+1})] \\
& + 2J_2[\sin(\theta_n - \theta_{n+1}) - \sin(\theta_{n-1} - \theta_n)] \\
& - 2J_{\parallel} \sin(2\theta_n) \qquad\qquad\qquad \text{for all } n > 1 \tag{6.2.2}
\end{aligned}$$

and

$$0 = J_\perp \sin(\theta_1 + \theta_2) + 2J_2 \sin(\theta_1 - \theta_2) - 2J_\| \sin(2\theta_1) \quad \text{for } n = 1. \quad (6.2.3)$$

We now put eq. 6.2.2 into a more convenient form. The angle sum and difference trigonometric identities are used and resulting terms grouped into coefficients of θ_n functions:

$$\begin{aligned} 0 = {} & (J_\perp - 2J_2)\cos\theta_n(\sin\theta_{n+1} + \sin\theta_{n-1}) \\ & + (J_\perp + 2J_2)\sin\theta_n(\cos\theta_{n+1} + \cos\theta_{n-1}) \\ & - 2J_\| \sin 2\theta_n. \end{aligned} \quad (6.2.4)$$

One can exploit the double-angle trigonometric form now present, by parameterising as

$$\left(\frac{J_\perp}{2J_2} - 1\right)\cos\theta_n = -R_n \cos\phi_n \quad (6.2.5)$$

and

$$\left(\frac{J_\perp}{2J_2} + 1\right)\sin\theta_n = R_n \sin\phi_n. \quad (6.2.6)$$

The choice of sign is for convenience, such that in the region of interest $J_\perp/2J_2 < 1$, θ_n, ϕ and R_n are all positive. Using this substitution, the equation can be written as

$$-\frac{J_\|}{J_2}\sin 2\theta_n = R_n \left[\sin(\theta_{n+1} - \phi_n) + \sin(\theta_{n-1} - \phi_n)\right]. \quad (6.2.7)$$

Given that $\sin\left(\theta_n - \phi_n\right) = -\left(\frac{J_\perp}{J_2 R_n}\right)\sin\theta_n \cos\theta_n$, the controlling equation for all $n > 1$ can then be written in the simplified form of

$$\sin\left(\theta_{n+1} - \phi_n\right) + \sin\left(\theta_{n-1} - \phi_n\right) = \frac{2J_\parallel}{J_\perp}\sin\left(\theta_n - \phi_n\right) \quad \text{for all } n > 1, \quad (6.2.8)$$

where ϕ is defined as

$$\tan\phi_n \equiv \frac{2J_2 + J_\perp}{2J_2 - J_\perp}\tan\theta_n, \tag{6.2.9}$$

which is valid provided that $J_\perp \neq 2J_2$. In the same way, eq. 6.2.3 can be written as

$$\sin\left(\theta_{n+1} - \phi_n\right) = \frac{2J_\parallel}{J_\perp}\sin\left(\theta_n - \phi_n\right) \quad \text{for } n = 1. \tag{6.2.10}$$

.

Eqs. 6.2.8 and 6.2.10 can be amalgamated to take the form of 6.2.10 by extending the range of n to include a virtual layer $n = 0$ and incorporating an appropriate boundary condition to effectively deal with the termination of the system at the surface $(n = 1)$ layer. This boundary condition is referred to as the 'surface' boundary condition, and is obtained by requiring

$$\sin\left(\theta_0 - \phi_1\right) = 0 \tag{6.2.11}$$
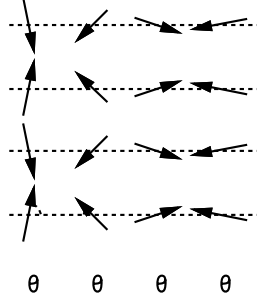
Figure 6.3: *Example of magnetic spin reorientation close to the surface (see main text).*

Thus, the turning points of the solution corresponding to any $J_\perp \neq 2J_2$ satisfy

$$\sin(\theta_{n+1} - \phi_n) + \sin(\theta_{n-1} - \phi_n) - 2\frac{J_\parallel}{J_\perp}\sin(\theta_n - \phi_n) = 0 \qquad (6.2.12)$$

for all $n\epsilon[0, \infty]$ in terms of

$$\tan\phi_n \equiv \frac{2J_2 + J_\perp}{2J_2 - J_\perp}\tan\theta_n, \qquad (6.2.13)$$

provided the surface boundary condition

$$\theta_0 = \phi_1 \qquad (6.2.14)$$

is applied.

For the special case of $J_\perp = 2J_2$, the controlling equation cannot be expressed in this way. The energy equation to minimise in this case simplifies to:

$$E = \sum_n (J_\parallel \cos 2\theta_n - 2\cos\theta_n \cos\theta_{n+1}). \qquad (6.2.15)$$

The turning points for the special case are determined by the same process as before, specifically by differentiating expression (6.2.15) with respect to θ_n and setting the resulting expressions to zero. The following expression is valid for all n if we implement the boundary condition $\theta_0 = \frac{\pi}{2}$

115

$$\sin \theta_n \left[\cos \theta_{n+1} + \cos \theta_{n-1} - 2\frac{J_\parallel}{J_\perp} \cos \theta_n \right] = 0. \qquad (6.2.16)$$

The appropriate boundary condition in the bulk is given by

$$\theta_n \mapsto \theta_\infty. \qquad (6.2.17)$$

In what follows, we will take $\theta_\infty=0$, which is valid for parameter values that simultaneously satisfy $J_\parallel < J_\perp$, and $\frac{J_\parallel}{2J_2} < 1$, in which the bulk ground state corresponds to $\theta_n = 0$. Note that if the latter condition is not met then the state favoured by the surface is the same as the bulk, and in this case we can expect the bulk phase to extend undistorted all the way up to the surface.

There are five basic approaches that unravel the expected behaviour: firstly, linearisation which establishes the phase boundary to surface distortion; secondly, a transformation that maps the Néel-like states onto the single-q-like states and completes the phase diagram; thirdly, an exactly solvable boundary which highlights the general principles and controls the energetic subtleties; fourthly, the continuum limit that provides simple pictures and physical intuition; lastly, the exact solution, found numerically, which underpins the previous more instructive calculations. However, before we solve the problem analytically, we first look into which energies in particular cause and control the existence of a surface reconstruction to get a feel for our problem and include a 'back of the envelope' calculation for length scales involved.

6.3 Feasibility Study - Energetic Considerations

Before we solve our model, we perform a short study on the energetic considerations involved. In the following section we shall perform an approximate energy balance to determine a length scale for the phenomenon, but to begin with, let us consider which energies are responsible for one state being preferred over the other at the

surface and within the bulk.

Specifically there are two energies at work: the 'intrinsic' energy from which our system is built, or in other words, the magnetic coupling J's, and the magnetoelastic energy that is gained as a result of martensitic distortions, which are proportional to $|J_\perp - J_\parallel|$. We explicity define these two energies in our Hamiltonian by writing them as two seperate terms; the average interaction energy and the magnetoelastic energy:

$$H = \left(\frac{J_\perp + J_\parallel}{2}\right)\left[\sum_{<i,j>_\perp} \mathbf{s}_i.\mathbf{s}_j + \sum_{<i,j>_\parallel} \mathbf{s}_i.\mathbf{s}_j\right]$$
$$+ \left(\frac{J_\perp - J_\parallel}{2}\right)\left[\sum_{<i,j>_\perp} \mathbf{s}_i.\mathbf{s}_j - \sum_{<i,j>_\parallel} \mathbf{s}_i.\mathbf{s}_j\right] + J_2\sum_{<i,j>_2} \mathbf{s}_i.\mathbf{s}_j. \quad (6.3.1)$$

In this way, we determine whether the different states cost different energies as a result of magnetoelasticity or simply the innate broken bonds present at the surface. We perform the summations for our particular problem, paying particular attention to boundary effects. Specifically, we must perform the summation over bonds such that at the upper limit of infinity, the contributions are correct and a new, equivalently 'surface' boundary is not introduced. As such, we sum over nearest neighbour bonds in all directions for all atoms from layer $n = 2$ to infinity, taking into account double-counting, and add the $n = 1$ layer as a separate term, hence covering all bonds in the system and overcoming termination problems. In this way, the hamiltonians for the different states we are interested in, $(k_x, k_y) = (0, \pi)$ and $(\pi, 0)$, which we label states 1 and 2 respectively, are computed. For the term that involves the summation from $n = 2$ to ∞, which we call the 'bulk' term of the Hamiltonian, we have

$$H_{bulk}^1 = \sum_{n=2}^{\infty} \left[-(J_\perp - J_\parallel) - 2J_2 \right] \tag{6.3.2}$$

for the energy if state 1 is used, and

$$H_{bulk}^2 = \sum_{n=2}^{\infty} \left[+(J_\perp - J_\parallel) - 2J_2 \right] \tag{6.3.3}$$

for the energy if state 2 is used. From this, we can immediately see that the degeneracy of the two states is broken in the 'bulk' *solely* by the magnetoelastic effects.

We now study the terms due to the surface layer, $n = 1$:

$$H_{n=1}^1 = + \left(\frac{J_\perp + J_\parallel}{4} \right) - 3 \left(\frac{J_\perp - J_\parallel}{4} \right) - J_2 \tag{6.3.4}$$

$$H_{n=1}^2 = - \left(\frac{J_\perp + J_\parallel}{4} \right) + 3 \left(\frac{J_\perp - J_\parallel}{4} \right) - J_2. \tag{6.3.5}$$

Contrary to the 'bulk', the surface layer contribution to the energy is state-dependant as a result of both the magnetoelastic distortion *and* intrinsic energy, or in other words, due merely to the existence of either or both interaction constants $J_\parallel$ and $J_\perp$. Thus this 'intrinsic' energy gain at the surface of having, for example, state 2 if we are in the regime of $J_\parallel > \frac{J_\perp}{2}$, is indeed due to the loss of bonds at the surface. The magnetoelastic distortion in this case merely serves to stabilise further one state over the other. Specifically, in the regime $J_\parallel > J_\perp$, the magnetoelastic energy serves to stabilise a state already preferred due to the loss of bonds at the surface. For $\frac{J_\perp}{2} < J_\parallel < J_\perp$, the magnetoelastic energy tries to destabilise this surface-preferred state but fails, and only in the region of $J_\parallel < \frac{J_\perp}{2}$ does the magnetoelastic energy win

over the intrinsic energy and the surface prefers the state that is taken in the bulk. As such, as is referred to previously, 'below' but near the degeneracy line $J_\parallel = J_\perp$ the surface indeed prefers state 2 over state 1, whereas the bulk prefers state 1 over state 2. We note that this calculation is approximate to help decide on feasibility, since the domain wall cost has not been included. However, in general it is true that if the $n = 1$ calculation shows the bulk state is preferred then there can be no reconstruction, but if the other state is preferred, then one of our criteria is satisfied and there may be reconstruction.

If our system, undergoes a magnetoelastic distortion, the resulting effect is a finite value of magnetoelastic energy and one state preferred over the other in the bulk. If the distortion stabilises state 1 in the bulk, then if we are close enough to degeneracy between the two states then we can expect the system to change to state 2 as the surface is approached, merely due to the loss of bonds.

6.3.1 Energy Balance

We now proceed to do a 'back of the envelope' calculation for the depth, D, to which the surface-preferred state protrudes into the bulk, by balancing relevant energies to the problem. We need to consider 3 energies: (a) the energy gained at the surface layer, $n = 1$, by adopting the surface-preferred state, which gains from the loss of bonds, (b) the energy cost of adopting the surface-preferred state down to depth D for parameter values in which it is not the ground state, the cost being attributed to the magnetoelastic energy, and (c) the energy cost of the domain wall between the two states. There is of course no energy associated with the interaction between the two states on superimposing them, since they are superimposed orthogonally.

Our energy balance simplifies nicely due to the fact that the energy cost of the domain wall can be neglected, as shall now be shown. The domain wall energy for our problem corresponds to the Heisenberg cost associated with the variation layer-by-layer of the angle θ, which occurs as state 2 is slowly transformed into state 1 as

we move further into the bulk.

We determine the Heisenberg energy cost of the state represented in fig. 6.3, whereby the θ_n varies from layer-to-layer, and determine the dependance of the energy on the existence of the domain wall by examining the dependence on the variable $\delta\theta_n$. For the purposes of this derivation we shall call this state the $\delta\theta_n$ state. Being an orthogonal superposition of states 1 and 2, the state can be written as a sum of the **s.s** contributions of state 1 and state 2. Specifically, we take the cosine of the spin vector to be the state 1 contribution and the sine of the spin vector to be the state 2 contribution. We hence obtain the following expression for $H_{bulk}^{\delta\theta_n}$ by summing for $n = 2$ to $n = \infty$ using the convention for the 'bulk' summation as applied in the H_{bulk} calculation of the previous section:

$$
\begin{aligned}
H_{bulk}^{\delta\theta_n} = S^2 \sum_{n=2}^{\infty} \Bigg[& J_\parallel \left[\cos 2\theta_n\right] - \frac{J_\perp}{2} \left[\cos\left(\theta_n + \theta_{n+1}\right)\right] - \frac{J_\perp}{2}\left[\cos\left(\theta_n + \theta_{n-1}\right)\right] \\
& - J_2 \left[\cos\left(\theta_n - \theta_{n+1}\right)\right] - J_2\left[\cos\left(\theta_n - \theta_{n-1}\right)\right] \Bigg].
\end{aligned}
\tag{6.3.6}
$$

We take a Taylor expansion of the cosine functions using the conventions $\theta_{n+1} = \theta_n + \delta\theta_n$ and $\theta_{n-1} = \theta_n - \delta\theta_{n-1}$ to obtain

$$
\begin{aligned}
H_{bulk}^{\delta\theta_n} \simeq S^2 \sum_{n=2}^{\infty} \Bigg[& J_\parallel \cos 2\theta_n - \frac{J_\perp}{2}\left(\cos 2\theta_n - \delta\theta_n \sin 2\theta_n - \frac{(\delta\theta_n)^2}{2}\cos\theta_n\right) \\
& - \frac{J_\perp}{2}\left(\cos 2\theta_n + \delta\theta_{n-1}\sin 2\theta_n - \frac{(\delta\theta_{n-1})^2}{2}\cos\theta_n\right) \\
& - J_2 \left(1 - \frac{(\delta\theta_n)^2}{2}\right) - J_2\left(1 - \frac{(\delta\theta_{n-1})^2}{2}\right) \Bigg].
\end{aligned}
\tag{6.3.7}
$$

We justify the relevance of Taylor expanding by considering that the angle θ_n will rotate from $\frac{\pi}{2}$ on the surface to 0 in the bulk over a length scale D, such that we can approximate $\delta\theta_n$ to be $\frac{\pi}{2D}$. As such, if we are in the region of parameter space corresponding to D being many layers, then the approximation is valid.

We make the additional approximation that $\delta_n \simeq \delta_{n-1}$ and so determine that, for small $\delta\theta_n$, the expression for the Heisenberg cost is given by

$$H_{bulk}^{\delta\theta_n} \simeq S^2 \sum_{n=2}^{\infty} \left[J_\perp \cos 2\theta_n - \frac{J_\parallel}{2} \left(2\cos 2\theta_n - (\delta\theta_n)^2 \cos 2\theta_n \right) \right.$$
$$\left. - J_2 \left(2 - (\delta\theta_n)^2 \right) \right]. \tag{6.3.8}$$

The Heisenberg energy associated with the state where the domain boundary is present is therefore dependent on $\delta\theta_n$ only to second order. As such, for small $\delta\theta_n$, or in other words for parameter values where the surface state protrudes into the bulk over many layers, we can ignore the cost of the domain boundary and merely pay attention to the first 2 energy considerations discussed previously. Note however that for small D, $\delta\theta_n$ is no longer small. As such the domain boundary cost is very much relevant in this case and the following simple analysis is not valid.

We therefore consider the case of small $\delta\theta_n$ and neglect the structure of the domain wall, simply assuming that the system takes state 2 down to a depth D, whereby the system switches to take up state 1 instead, with no superposition of the states involved. In this case our balance becomes the energy gain of using state 2 on the surface layer versus the cost of having state 2 in the bulk, referenced to state 1, and within the parameter regime $J_\parallel > \frac{J_\perp}{2}$ in which the surface can prefer a different state from that taken by the bulk:

$$H_{n=1}^1 - H_{n=1}^2 = D(H_{bulk}^2 - H_{bulk}^1) \tag{6.3.9}$$

$$\left[\frac{(J_\perp + J_\parallel)}{2} - \frac{3}{2}(J_\perp - J_\parallel) \right] = 2D(J_\perp - J_\parallel) \tag{6.3.10}$$

and so we find that the depth is approximately of the form:

$$D \simeq \frac{\left(J_{\parallel} - \frac{J_{\perp}}{2}\right)}{(J_{\perp} - J_{\parallel})}. \tag{6.3.11}$$

Note that this D is a maximum bound as we have completely ignored the cost of the domain wall, which is not negligible if we are not near the continuum limit whereby $\delta\theta_n$ is vanishing, corresponding to not being near the degeneracy regime $J_{\perp} = J_{\parallel}$, as shall be shown in section 6.7. As one would expect, D increases as one approaches degeneracy, tending to infinity at degeneracy whereby the system takes on state two throughout.

The continuum limit calculation tackled later in this chapter takes into account the domain wall cost that we have neglected in this simple calculation and provides the optimum structure.

6.4 Linearising to Obtain the Phase Boundary

The first natural limit is to *linearise* the 'minimisation problem' for $J_\perp \neq 2J_2$. This amounts to assuming that the distortion is infinitesimally small but *finite*, and as we will see leads to the phase boundary where the surface phase first appears. Linearising eq.(6.2.12) and eq.(6.2.13) we obtain

$$\theta_{n+1} + \theta_{n-1} = 2\phi_n + \frac{2J_\parallel}{J_\perp}(\theta_n - \phi_n) \tag{6.4.1}$$

and

$$\phi_n = \frac{(2J_2 + J_\perp)}{(2J_2 - J_\perp)}\theta_n \tag{6.4.2}$$

and hence generate the equation for turning points of the energy in the linearised regime:

$$\theta_{n+1} + \theta_{n-1} = 2\theta_n \frac{2J_2 + J_\perp - 2J_\parallel}{2J_2 - J_\perp}. \tag{6.4.3}$$

To solve this second order difference equation we employ the general solution

$$\theta_n = \theta_0 \lambda^n, \tag{6.4.4}$$

where substitution results in an expression λ must obey for the general solution to be valid:

$$\lambda + \frac{1}{\lambda} = 2\left[\frac{2J_2 + J_\perp - 2J_\parallel}{2J_2 - J_\perp}\right]. \tag{6.4.5}$$

λ is further constrained by our specific problem by our 'surface' boundary condition $\theta_0 = \phi_1$. The constraint comes into play by using eq.(6.4.2) and making use of our

general solution to replace θ_1. This sets λ to be

$$\lambda = \frac{(2J_2 - J_\perp)}{(2J_2 + J_\perp)}. \tag{6.4.6}$$

We observe that eq.(6.4.5) is only valid for infinitesimally small but *non-zero* distortion, and hence represents the condition at which the distortion first appears: our phase boundary for the surface reconstruction. We substitute our value for λ and obtain the phase boundary

$$J_\parallel = \frac{2J_\perp J_2}{(2J_2 + J_\perp)}. \tag{6.4.7}$$

.

This phase boundary is the lower curve in Fig. 6.4. At this phase transition, the symmetry with respect to lattice translations parallel to the surface, which is respected by the bulk magnetic state, is spontaneously broken in a layer near the surface with finite thickness ξ. Specifically, Eq. 6.4.4 describes an exponential decay of θ_n for $\lambda > 0$, or an exponentially-decaying envelope to the oscillating case of $\lambda > 0$), as we move from the surface ($n = 1$) into the bulk ($n = \infty$) with the characteristic decay length,

$$\xi = -\ln \left| \frac{2J_2 - J_\perp}{2J_2 + J_\perp} \right|^{-1}. \tag{6.4.8}$$

This formula is valid along the boundary line given by Eq. (6.4.7). It is plotted in Fig. 6.5 along with two representative dependences of the angle θ_n on the layer index n at the phase boundary. Note that the length ξ diverges as $J_\perp \to 0$ or $J_\perp \to \infty$ as in those limits the state favoured by the surface becomes degenerate with the bulk state.

Note that the dependence of θ_n on the layer index n is monotonic for $J_\perp < 2J_2$ but oscillatory for $J_\perp < 2J_2$. The oscillatory state corresponds to the preferred
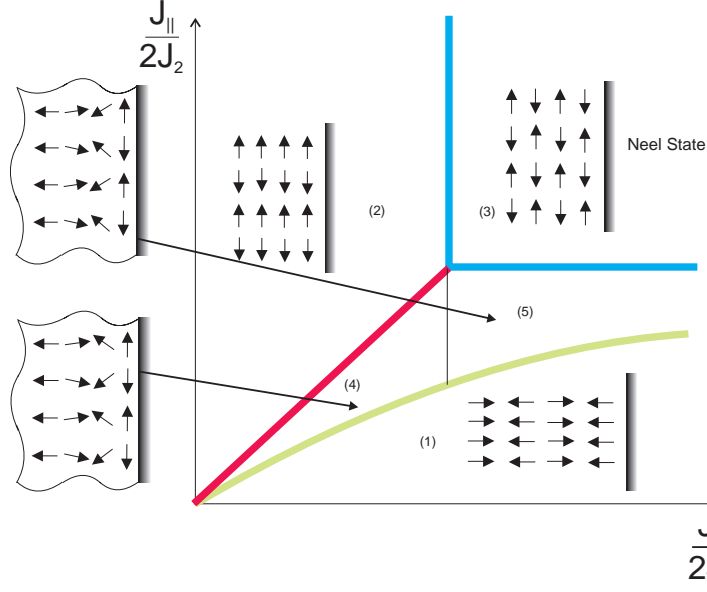
Figure 6.4: *A qualitative representation of the completed phase diagram for our square lattice model, showing regions (4 and 5) in which the surface reconstruction exists. In region (4), the surface-preferred state is the $\theta = \pi/2$, whereas in region (5) the superposition involves the 'bulk' state, $\theta = 0$ and the Néel state.*

surface phase being the Néel phase as opposed to the $\theta = \pi/2$ phase and one can generate this new state from that depicted in Fig. 6.3 by simply translating every second layer of spins by one unit parallel to the surface. The transformation between the oscillating and non-oscillating states will be seen in the next section.

6.5 Transformation

We can also understand the presence of the two styles of surface-reconstructed states by considering a transformation of the form

$$
\begin{aligned}
\theta_n &\mapsto (-1)^n \tilde{\theta}_n \\
J_2 &\mapsto \tilde{J}_2 \\
J_\perp &\mapsto \frac{(2\tilde{J}_2)^2}{\tilde{J}_\perp} \\
J_\parallel &\mapsto \frac{2\tilde{J}_2 \tilde{J}_\parallel}{\tilde{J}_\perp}
\end{aligned} \tag{6.5.1}
$$

125
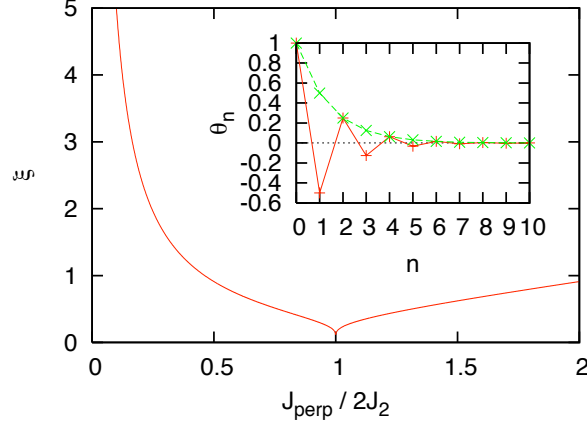
Figure 6.5: *The characteristic length of the surface state at the phase boundary where it forms, as a function of $J_\perp$. Inset: dependence of the angle θ_n on the layer index n for $\lambda = -0.5$ (solid line) and $\lambda = +0.5$ (dashed line).*

which sends

$$E \mapsto \frac{2\tilde{J}_2}{\tilde{J}_\perp} \tilde{E}. \tag{6.5.2}$$

The solution to the problem using the variables $\tilde{J}_\perp$, $\tilde{J}_\parallel$ and $\tilde{J}_2$ is $\tilde{\theta}_n$ which is identical to the solution θ_n for the square lattice defined by the variables $J_\perp$, $J_\parallel$ and J_2, but with the plane-by-plane oscillation that was discovered in the previous section. Applying this transformation maps our surface phase boundary onto itself and maps two regions that were not obviously related. The transformation provides the solution for $J_\perp > 2J_2$ in terms of the solution to $J_\perp < 2J_2$ with an added oscillation. Additionally, the transformation demonstrates a degeneracy when $J_\perp = 2J_2$, which amounts to the final boundary as depicted in fig.6.4 where both the monotonic and oscillatory solutions are degenerate. This completes the agreement with the solutions found on the phase boundary by the linearisation procedure in the previous section. The degeneracy between solutions is expected as it is located in the region whereby the two different surface-preferred states are degenerate. This degeneracy also manifests itself as a degeneracy associated with the spin quantisation direction within the planes parallel to the surface, which can be different for each plane. This corresponds to there being Néel sheets parallel to the surface, but the direction of

the spins within the sheets being arbitrary as long as this order is maintained.

6.6 Exact Solution

The next task is to analyse the special case of $J_\perp = 2J_2$ which provides an exact solution and a picture for how the solutions behave in general. The special equation of Eq. (6.2.16) has two possible solutions, either we find $\theta_n = 0$ and we are dealing with the undistorted bulk phase or we need to solve

$$\cos\theta_{n+1} + \cos\theta_{n-1} = 2\frac{J_\parallel}{J_\perp}\cos\theta_n \tag{6.6.1}$$

and we are dealing with the surface reconstruction. To solve this recursion relation we write it as the real part of an equation constructed using a new variable $z_n = e^{i\theta_n}$:

$$z_{n+1} + z_{n-1} = 2\frac{J_\parallel}{J_\perp}z_n. \tag{6.6.2}$$

We can solve this equation in exponentials using a power law, and we hence make the substitution $z_n = C\lambda^n$ to obtain

$$\lambda^2 - 2\frac{J_\parallel}{J_\perp}\lambda + 1 = 0. \tag{6.6.3}$$

Rearranging to the form

$$\frac{J_\parallel}{J_\perp} = \frac{\lambda + \frac{1}{\lambda}}{2}, \tag{6.6.4}$$

one can identify a trigonometric or hyperbolic function form, and since we are interested in the parameter range $J_\perp > J_\parallel$ where our surface reconstructs, we let $\lambda = e^{i\alpha}$ to obtain the expression in terms of a cosine function

$$\frac{J_{\parallel}}{J_{\perp}} = \frac{e^{i\alpha} + e^{-i\alpha}}{2} = \cos\alpha, \tag{6.6.5}$$

where we constrain $\cos\alpha$ to lie between 0 and 1 and further choose to constrain α to be between zero and $\frac{\pi}{2}$ in order to avoid ambiguities later. By using this specific substitution, we ensure the range defined by $J_{\perp} > J_{\parallel}$ is appropriate to the chosen function.

The substitution $\lambda = e^{-i\alpha}$ also returns expression (6.6.5) and represents another solution to our recursion relation. As such, the general solution to the recursion relation can now be determined from the real part of the general solution to z_n, which in turn is constructed from a linear combination of the roots of the linear equation eq.(6.6.2)

$$z_n = Ae^{in\alpha} + Be^{-in\alpha} \tag{6.6.6}$$

so that, given A and B can be complex,

$$\begin{aligned}
\cos\theta_n = Re[z_n] &= \frac{z_n + z_n^*}{2} \\
&= \frac{A + B^*}{2}e^{in\alpha} + \frac{A^* + B}{2}e^{-in\alpha} \\
&= \frac{c}{2}e^{in\alpha} + \frac{c*}{2}e^{-in\alpha} \\
&= \frac{|c|}{2}e^{i\gamma}e^{in\alpha} + \frac{|c|}{2}e^{-i\gamma}e^{-in\alpha} \\
&= |c|\left(\frac{e^{i(n\alpha+\gamma)} + e^{-i(n\alpha+\gamma)}}{2}\right) \\
&= |c|\cos(n\alpha + \gamma), \tag{6.6.7}
\end{aligned}$$

where $\alpha = \cos^{-1}\left(\frac{J_{\parallel}}{J_{\perp}}\right)$, and $|c|$ and γ are constants to be determined via the boundary conditions of our problem.

The appropriate boundary conditions to implement for the exact solution problem are our bulk boundary condition, $\theta_n = 0$, and our 'surface' boundary condition $\theta_0 = \frac{\pi}{2}$. Considering firstly the solution $\theta_n = 0$, we can see that whilst our bulk boundary condition is satisfied, our surface boundary condition is not. Conversely, the solution to eq.(6.6.7), which we label from hereon as $\tilde{\theta}_n$, can satisfy the surface boundary condition if $\gamma = \pm\frac{\pi}{2}$ but cannot simultaneously satisfy the bulk boundary condition. As such, our solution to the $J_\perp = 2J_2$ case for the entire system, θ_n defined for all n, must be constructed using a combination of both solutions $\theta_n = 0$ and $\tilde{\theta}_n$.

In constructing the combined state, we are hence forced to use $\tilde{\theta}_n$ for θ_0 and $\theta_n = 0$ for θ_∞. Additionally, we require the minimum energy solution, which further constrains how we construct the combined state. Applying firstly the surface boundary condition, we obtain

$$\cos\tilde{\theta}_n = |c| \cos\left(\frac{\pi}{2} - n\alpha\right) = |c| \sin(n\alpha). \tag{6.6.8}$$

From this form, one can resolve that $\tilde{\theta}_n$ is a decaying function up to its first zero-crossing, which we label $\tilde{n}$. The minimum energy combined state corresponds to switching to the $\theta_n = 0$ solution at this $\tilde{n}$, in order not to increase the energy of the combined state unneccessarily through the Heisenberg energy cost present in the $\tilde{\theta}_n$ solution for all subsequent $n > \tilde{n}$.

According to this construction, it is useful to express 6.6.7 with respect to an n at which $\tilde{\theta}_n$ is zero, which we label N. Hence we can now evaluate γ and obtain the useful form of

$$\cos\tilde{\theta}_n = \frac{\sin(n\alpha)}{\sin(N\alpha)}. \tag{6.6.9}$$

.

We now have an equation for our $\tilde{\theta}_n$ which obeys two constraints; firstly, that

at the zeroth layer, $\tilde{\theta}$ is $\frac{\pi}{2}$, and secondly, that at some layer, N, $\tilde{\theta}_N$ goes to zero. On analysing the roots of the function $\tilde{\theta}_n$ defined by eq. 6.6.9 we will find that *two distinct* roots come into existence as α is varied and that this corresponds to the surface state moving into the bulk on the variation of α, or rather, the variation of the ratio $\frac{J_\perp}{J_\parallel}$, the distance from the line of degeneracy.

The roots of $\tilde{\theta}_n$ obey

$$\sin\left(N\alpha\right) = \sin\left(n\alpha\right) \tag{6.6.10}$$

and in addition, from trigonometric identities, obey

$$-\sin\left(-N\alpha\right) = \sin\left(\pi - N\alpha\right) = \sin n\alpha. \tag{6.6.11}$$

Thus two roots exist; $N = n_a$ and $N = n_b = \frac{\pi}{\alpha} - n_a$. These roots are identical when $N = n_a = n_b = \pi/2\alpha$. Given that N is an integer, on the variation of α the roots first become distinct when $n_b = n_a \pm 1$.

We now study the consequences of this by setting $n_a = 1$, which corresponds to the case of there being no surface phenomenon (where all layers have $\theta_n = 0$) and varying α to access additional zero-crossings. The next available zero-crossing occurs for $n_b = n_a + 1 = 2$ corresponding to $\alpha = \pi/(2n_a + 1) = \pi/3$ and so the decrease of α results in an additional zero-crossing being accessed at a higher plane number. This additional zero-crossing can be thought of as an n_a value in its own right corresponding to a particular $\tilde{\theta}_n(n_a)$ solution (since the solutions are functions of $n_a = N$) with an additional zero-crossing appearing again at $\alpha = \pi/(2n_a + 1)$. Thus, as α is decreased, solutions corresponding to the surface state moving further and further into the bulk become accessible. The ground state is constructed by splicing the $\tilde{\theta}_n(n_a)$ solution with the $\theta_n = 0$ solution at the location of the first zero-crossing, or lowest root value n_a, of the $\tilde{\theta}_n$ function for the energetic reasons described above. However, a final task exists of determining *which* $\tilde{\theta}_n(n_a)$ function

corresponds to the minimum energy solution for a given value of α.

The number of solutions $\tilde{\theta}_n(n_a)$ available at a certain value of α increases as $J_\parallel \to J_\perp$. Bearing in mind that we cut the solution $\tilde{\theta}_n$ at the first zero-crossing n_a, which we will refer to from now on as N, one can determine the energy saved by using the different surface solutions $\tilde{\theta}_n(N)$ instead of using the bulk state all the way to the surface, as a function of α

$$\frac{\Delta E}{J_\perp}(\tilde{N}, \alpha) = 2(\tilde{N} - 1)(\cos\alpha - 1) + \frac{\sin([\tilde{N} - 1]\alpha)}{\sin\tilde{N}\alpha}. \qquad (6.6.12)$$

From the graphs of fig. 6.6, where ΔE is only plotted for any specific N when it becomes 'available' as a solution, it can be seen that the larger the N, the lower the energy of the solution, for any α. As such, once a new N appears as α is decreased, the $\tilde{\theta}_n$ corresponding to that N is the ground state solution. Specifically, $\tilde{\theta}_n(N)$ only represents the ground state solution for the range

$$\frac{\pi}{2N + 1} \leq \alpha \leq \frac{\pi}{2N - 1}, \qquad (6.6.13)$$

or alternatively,

$$\cos\left(\frac{\pi}{2N - 1}\right) \leq \frac{J_\parallel}{J_\perp} \leq \cos\left(\frac{\pi}{2N + 1}\right) \qquad (6.6.14)$$

Therefore as α is decreased, the solution corresponding to N stays the ground state until a certain α, at which point it 'jumps' to the next plane.

As such, the ground state solution evolves as α decreases in a very special way. The length scale over which the solution decays to zero increases, changing at an increasing number of planes. More importantly there is *no* exponential decay into the bulk; the surface state has a sharp cut-off with respect to its protrusion into the
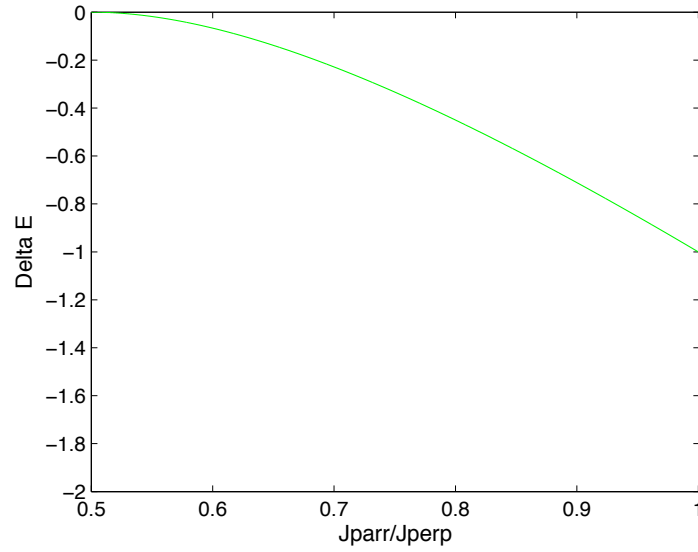
(a) N=1
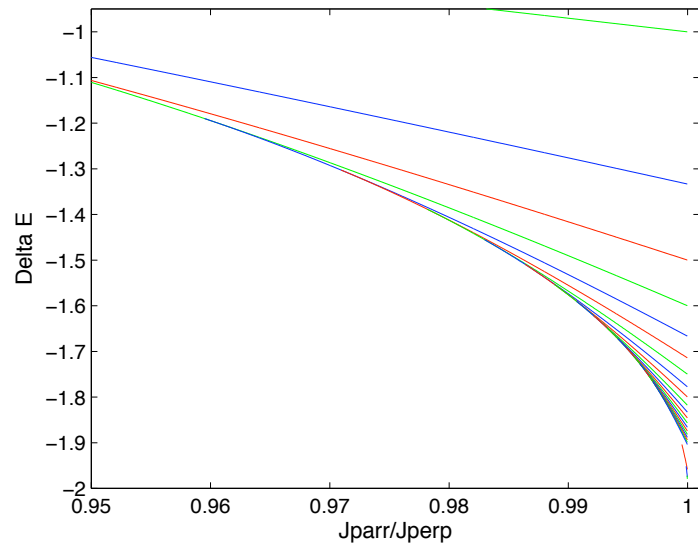
(b) several N

Figure 6.6: *Plot of the difference in energy between bulk state and superposition of surface and bulk states, ΔE, versus ratio $\frac{J_\parallel}{J_\perp}$, for (a) $N = 1$ (when the surface state first appears), and (b) $N = 1$ to $N = 20$, plus $N = 50, 100$ and 150, for $J_2 = 1$. Increasing N corresponds to the curve location being lower*

bulk of the material and goes like

$$N \simeq \frac{\pi}{2 \left(1 - \frac{J_\parallel}{J_\perp}\right)^{\frac{1}{2}}}. \tag{6.6.15}$$

We check agreement with the phase boundary found earlier by the linearisation procedure. The solution constructed by assigning N equal to 1, which corresponds to no surface phenomenon, is the valid ground state for the range

$$0 \leq \frac{J_\parallel}{J_\perp} \leq \frac{1}{2}. \tag{6.6.16}$$

On our phase diagram, this range corresponds to a parameter line on our exact solution line that extends from zero up to and including the phase boundary. This is as expected, since it is in the region of no surface phenomenon. Furthermore, the upper bound of this range indeed corresponds to the phase boundary for the exact solution, since at this point in phase space $\tilde{\theta}_n$ has zero-crossings at both $n = 1$and $n = 2$. Thus, increasing $J_\parallel$ further results in the ground state becoming the state where $N = 2$, and the surface phenomenon hence appears. Finally, as the triple point on the phase diagram is approached, N tends to infinity, corresponding to the ground state tending towards $\theta_n = \pm\frac{\pi}{2}$ for all n, again as expected.

To further understand the qualitative form of the combined state, we study the 'shape' of the function $\tilde{\theta}_n$. If $N\alpha = \frac{\pi}{2}$, the value of α at which there is no degeneracy in where the zero-crossing lies and the system has settled on a single choice of layer at which to go to zero, then we simply have a decaying linear dispersion

$$\tilde{\theta}_n = -n\alpha + \frac{\pi}{2}. \tag{6.6.17}$$

For other values of α, we can describe the solution as a deviation from the linear

dispersion

$$\tilde{\theta}_n = -n\alpha + \frac{\pi}{2} - \gamma_n, \qquad (6.6.18)$$

where γ_n is the deviation of θ_n from that of the linear dispersion. We determine the deviation for the limit of large N, which corresponds to small α. This limit corresponds to the limit of $J_\parallel \to J_\perp$. We express N as

$$N\alpha = \frac{\pi}{2} + \mu\alpha, \qquad (6.6.19)$$

where μ is determined by considering the range for $N\alpha$ outside of which the solution returns to a linear form. Due to the discreteness of our problem, the range corresponds to the values of α at which N shares a root with $N+1$ or $N-1$, which. Thus, we have a range for α of

$$\frac{\pi}{2N+1} \le \alpha \le \frac{\pi}{2N-1}, \qquad (6.6.20)$$

which corresponds to the range of $\mu \in [-\frac{1}{2}, \frac{1}{2}]$. $\mu = 0$ returns the N that corresponds to the original linear dispersion solution. Moving outside of this range, $N\alpha$, being a discrete variable, corresponds next to another linear solution.

Expression 6.6.19 is substituted into eq.(6.6.9). Since α is very small, so is the term $\mu\alpha$ and as such we can perform a Taylor's expansion of $\sin(N\alpha)$ followed by a binomial expansion to obtain, to first order,

$$\cos\tilde{\theta}_n \simeq \sin(n\alpha)\left[1 + \frac{(\mu\alpha)^2}{2}\right]. \qquad (6.6.21)$$

135

To determine the deviation γ_n, we compare eq.6.6.21 to the cosine of expression 6.6.18

$$\cos \tilde{\theta}_n = \sin(n\alpha) \left[\frac{\sin \gamma_n}{\tan(n\alpha)} + \cos \gamma_n \right], \qquad (6.6.22)$$

which, to leading order in γ_n, gives

$$\gamma_n \simeq \frac{1}{2}(\mu\alpha)^2 \tan(n\alpha). \qquad (6.6.23)$$

This expression for the deviation from the linear solution is valid for small α, corresponding to large N.

Since only the cosine of the angle is relevant, the angles may be chosen to have *arbitrary* signs and this amounts to an arbitrary choice of using the single-q or Néel continuation for the surface distortion. Therefore our exact solution corresponds to the boundary between the two states where the surface distortion is of a single-q character and when it is of a Néel character. Indeed this phase boundary marks a *pure surface* phase transition.

6.7 Continuum Limit

The fourth style of calculation is the continuum limit in which we take the system size L to ∞. The continuum limit is hence the limit at which 'change' occurs over an infinite length. One can determine the shape of the domain wall, or in other words the form of the function θ_n using this limit, and proceed to fix the scaling and position of the function with respect to the variable n by choosing the appropriate boundary condition to the problem where we approach but are not at the continuum limit. The generation of this boundary condition is undertaken in detail later in this section.

Taking the continuum limit is equivalent to assuming a slowly varying solution where $\frac{d\theta_n}{dn}$ tends to zero, and treating n as a continuous variable. As such, the summations present in the energy equation (become integrals over dn and we can Taylor expand around θ_n to obtain the energy functional in terms of

$$E = E\left(\theta_n, \theta'_n; n\right) \tag{6.7.1}$$

such that Euler Lagrange can be applied. Applying the boundary condition $\theta_\infty = 0$, we obtain an expression for the energy to second order in $(\theta_{n+1} - \theta_n)$

$$
\begin{aligned}
E = \quad & (J_\parallel - J_\perp) \int_n dn \cos 2\theta_n + \tfrac{1}{2} \int_n dn (\theta'_n)^2 \left[2J_2 - J_\perp \cos 2\theta_n\right] \\
& - \tfrac{J_\perp}{2} (1 - \cos 2\theta_0) - \tfrac{J_\perp}{2} \theta'_n (n = 0) \sin 2\theta_0 - 2J_2(n_\infty - n_0).
\end{aligned}
\tag{6.7.2}
$$

Since we are only interested in finding the function θ_n that minimises the energy, we ignore constant terms and define the Lagrangian as

$$\mathscr{L} = (J_\parallel - J_\perp) \cos 2\theta_n + \frac{1}{2}(\theta'_n)^2 [2J_2 - J_\perp \cos 2\theta_n], \tag{6.7.3}$$

where we wish to minimise the value F defined by

$$F = \int_0^\infty \mathscr{L}(\theta_n, \theta_n') dn. \tag{6.7.4}$$

Since the Lagrangian for our problem does not depend explicitly on n, to minimise F we therefore use

$$\theta_n' \frac{\partial \mathscr{L}}{\partial \theta_n'} - \mathscr{L} = C, \tag{6.7.5}$$

where C is defined by boundary conditions.

The Euler-Lagrange equation for our system returns the following condition that must be satisfied by all θ_n in order for the solution to correspond to a turning point in the energy:

$$\left(\frac{d\theta_n}{dn} \right)^2 = 2 \frac{\left[C + (J_{||} - J_\perp) \cos 2\theta_n \right]}{(2J_2 - J_\perp \cos 2\theta_n)}. \tag{6.7.6}$$

Given that $\theta_n \to 0$ as $n \to \infty$, we can assume that as $n \to \infty$, $\theta_n' \to 0$ (since the solution must skim the $\theta_n = 0$ line as $n \to \infty$). Applying this boundary condition in conjunction with our bulk boundary condition $\theta_n \to 0$ as $n \to \infty$, the value of C is determined to be $J_\perp - J_{||}$. As such, we arrive at an expression that minimises the energy in the continuum limit

$$\left(\frac{d\theta_n}{dn} \right)^2 = 2 \frac{\left[(J_\perp - J_{||})(1 - \cos 2\theta_n) \right]}{(2J_2 - J_\perp \cos 2\theta_n)}. \tag{6.7.7}$$

The continuum limit is valid only when θ_n' is vanishingly small, which, from expression 6.7.7, is true when the parameter $J_\perp - J_{||}$ is vanishingly small. This

corresponds to the region of the phase diagram which is only a small departure from the degeneracy line $J_\perp = J_{||}$.

Eq.(6.7.7) in turn integrates to yield

$$
2 \left[\frac{J_\perp - J_{||}}{2J_\perp} \right]^{\frac{1}{2}} (n_0 - n) = \cos^{-1} \left[\left(\frac{2J_\perp}{2J_2 + J_\perp} \right)^{\frac{1}{2}} \cos \theta \right]
$$
$$
+ \left(\frac{2J_2 - J_\perp}{2J_\perp} \right)^{\frac{1}{2}} \ln \left[\frac{(2J_2 + J_\perp)^{\frac{1}{2}} \sin \theta}{(2J_2 - J_\perp \cos(2\theta))^{\frac{1}{2}} + (2J_2 - J_\perp)^{\frac{1}{2}} \cos \theta} \right],
$$

$$(6.7.8)$$

where the ambiguity of signs present in deriving solution (6.7.8) has been removed by requiring that the lowest energy solution is chosen, which corresponds to choosing signs so that as $n \to \infty$, $\theta_n = 0$.

Being a continuum limit, all values of θ_n are valid solutions to all/any n at the continuum limit, since the solution changes over an infinite length scale. To single out the solution for which the 'surface state' of $\theta = \pi/2$ is adopted, we choose the solution (by applying a suitable boundary condition) such that at the continuum limit, i.e. when $J_\perp = J_{||}$, $\theta = \pi/2$ for any n, including the surface layer, as required. Using this construction, once the boundary condition and hence the length scale is introduced, the corresponding solution to the continuum limit becomes one in which θ_n moves from $\pi/2$ to zero as the plane number increases, as is required.

This construction amounts to defining a new variable m_0 as

$$
2 \left[\frac{J_\perp - J_{||}}{2J_\perp} \right]^{\frac{1}{2}} n_0 = 2 \left[\frac{J_\perp - J_{||}}{2J_\perp} \right]^{\frac{1}{2}} m_0 + \frac{\pi}{2} \tag{6.7.9}
$$

and as such, expressing the solution to the continuum limit as

$$2 \left[\frac{J_\perp - J_\parallel}{2J_\perp} \right]^{\frac{1}{2}} (m_0 - n) = -\frac{\pi}{2} + \cos^{-1} \left[\left(\frac{2J_\perp}{2J_2 + J_\perp} \right)^{\frac{1}{2}} \cos\theta \right]$$
$$+ \left(\frac{2J_2 - J_\perp}{2J_\perp} \right)^{\frac{1}{2}} \ln \left[\frac{(2J_2 + J_\perp)^{\frac{1}{2}} \sin\theta}{(2J_2 - J_\perp \cos(2\theta))^{\frac{1}{2}} + (2J_2 - J_\perp)^{\frac{1}{2}} \cos\theta} \right].$$

$$(6.7.10)$$

The next task amounts to choosing an appropriate value for m_0, the 'other part' of the boundary condition so to speak. Before we begin this task, let us understand further the role m_0 plays by studying the form of solution (6.7.10). By considering the LHS of the equation as the variable, x, for a function that returns θ [2], one can see that $J_\perp - J_\parallel$ controls the length scale of the function θ and m_0 shifts the function to the left and right wrt x i.e. wrt the parameter $(J_\perp - J_\parallel)^{\frac{1}{2}}$. As such, the continuum limit solution can be fitted to the discrete solution for values of the parameter $J_\perp - J_\parallel$ close to the continuum limit range, up to a reasonable accuracy, and we have successfully modelled the problem by using the continuum limit technique.

We now return to the problem of determining an appropriate value of m_0. The boundary condition must satisfy the surface boundary condition of the general problem, in the regime of the continuum limit. We reproduce the boundary condition of the general problem in its exact form here:

$$\tan(\theta_0) = \left(\frac{2J_2 + J_\perp}{2J_2 - J_\perp} \right) \tan(\theta_1) \tag{6.7.11}$$

and rewrite in a more convenient form for our next steps as:

$$\sin(\theta_0 - \theta_1) = \frac{J_\perp}{2J_2} \sin(\theta_0 + \theta_1). \tag{6.7.12}$$

---

[2]The function can be obtained in practice by rearrangement, but this is not required here, only the concept is considered

One can use the fact that $n = m_0$ when $\theta = \pi/2$ to express θ_n as a Taylor expansion around m_0

$$\theta(m_0 + [n - m_0]) = \theta_n = \theta_{m_0} + (n - m_0)\frac{d\theta}{dn}\bigg|_{n=m_0}$$
$$+\frac{(n - m_0)^2}{2}\frac{d^2\theta}{dn^2}\bigg|_{n=m_0} + ... \qquad (6.7.13)$$

One can show that this expansion is valid for *any* n, not just for $n \simeq m_0$ and furthermore that the first order expansion is an expansion of appropriate accuracy. We hence obtain an expression for θ_n

$$\theta_n = \frac{\pi}{2} + (n - m_0)\frac{d\theta}{dn}\bigg|_{n=m_0}, \qquad (6.7.14)$$

which can be substituted into our surface boundary condition (6.7.12). A further simplification can be applied in the sense of Taylor expanding the sine function to first order, by taking into account that the 1st differential of θ_n at m_0 has previously been shown to be small. As such, we arrive at a value for our continuum limit boundary condition

$$m_o = \frac{(J_\perp - 2J_2)}{2J_\perp} \qquad (6.7.15)$$

that satisfies the surface boundary condition as applied to the continuum limit. For completeness we now state the complete boundary condition

$$2\left[\frac{J_\perp - J_\parallel}{2J_\perp}\right]^{\frac{1}{2}} n_0 = 2\left[\frac{J_\perp - 2J_2}{2J_\perp}\right]\left[\frac{J_\perp - J_\parallel}{2J_\perp}\right]^{\frac{1}{2}} + \frac{\pi}{2}. \qquad (6.7.16)$$

Returning to the form of our continuum limit solution, we study what the form tells us about our problem. The 'perturbative' parameter, $(J_\perp - J_\parallel)$, which 'perturbs' the system away from case whereby all spins take up the bulk ground state configuration, serves to control the diverging n in the solution. One can also observe

141
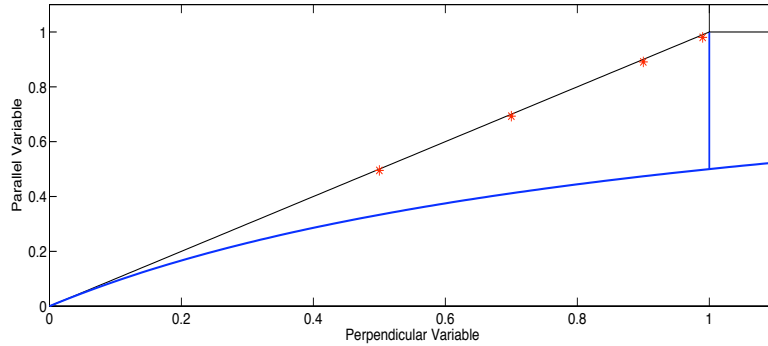
Figure 6.7: *Bulk and surface phase diagram for our square lattice model to show the positions (red stars) at which we explicitly calculate the solution (seen in figs. 6.8 and 6.9) using both the continuum limit technique and direct numerical calculation to determine the exact solution.*

the presence of a $\cos 2\theta_n$ term, which one can immediately contribute to the difference in energy in having the two states, applied to a given superimposition described by θ, and which is dependent on the ratio of the superimposition of the states. We employ a numerical 'shooting' method to solve the difference equation, Eq. (6.2.12), and the continuum limit is compared with the exact solution in figure 6.

If both θ_0 and θ_1 are known, the difference equation generates θ values for all other values of n. Moreover, the problem is further simplified by the surface boundary condition, such that if solely θ_1 is known, ϕ_1 and hence in turn θ_0 can be calculated and the solution to the problem therefore solved entirely from a single value, θ_1.

To determine a θ_1 appropriate for the minima solution, a secant method is employed, whereby θ_N is expressed as a function of θ_1 and we require the root of this function to be zero, corresponding to requiring θ_N be zero. Furthermore, this N value must be chosen such that the solution given by the function θ_n has no turning points wrt n, so that we choose the minima energy solution from our set of 'turning point' solutions.

The parameter that is small in the continuum limit is $\epsilon = 1 - \frac{J_\parallel}{J_\perp}$ and we have chosen ϵ=0.01 in fig. 6.8 and allowed $J_\perp$ (or effectively $j_\perp$) to vary. There is a very close correspondence between the exact solution and the continuum limit as might be expected in this limit. The behaviour of the spins is well described by the exact
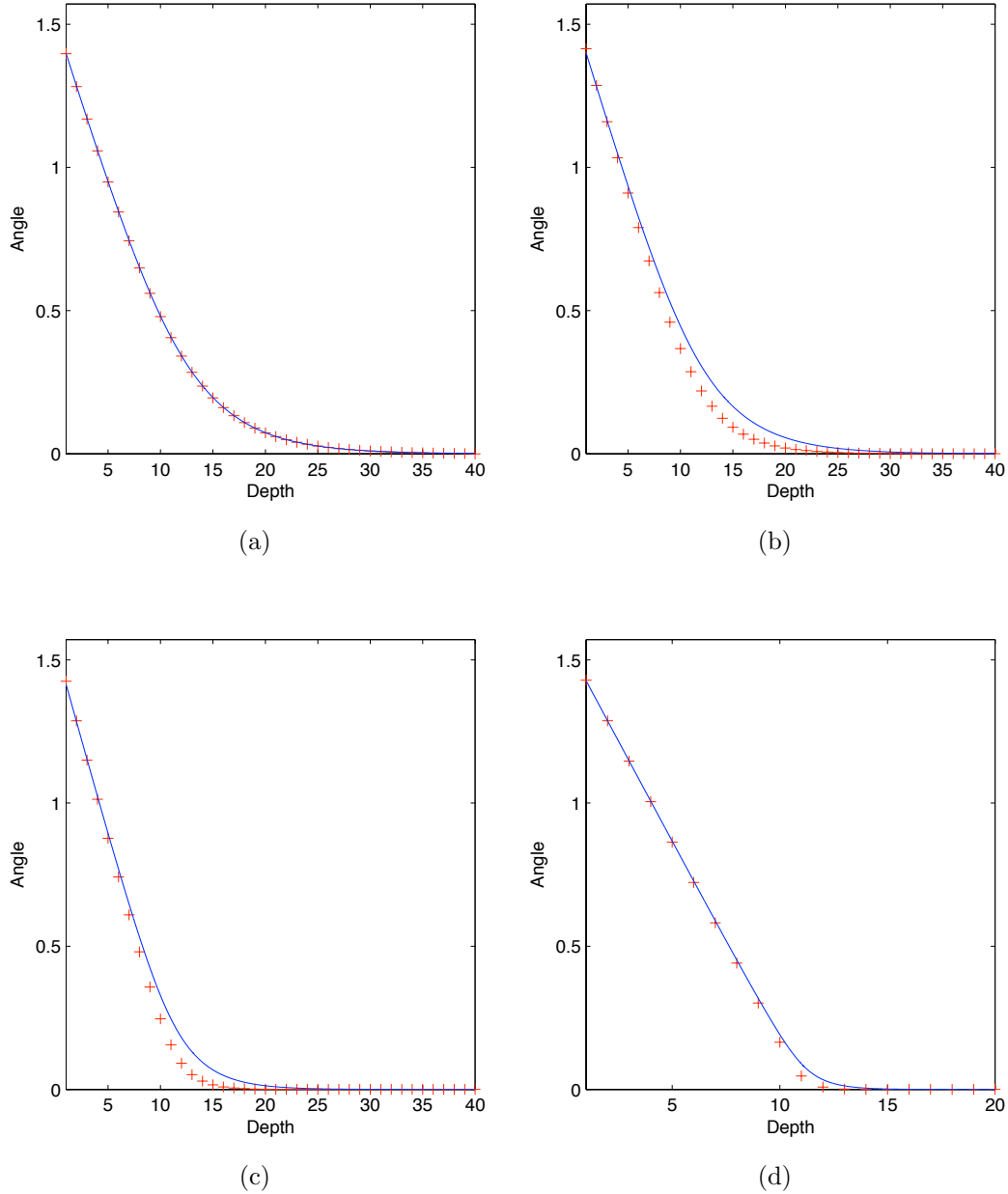
Figure 6.8: *A variety of angular profiles that describe the surface distortions for $\epsilon = 0.01$ for various values of the ratio $\frac{J_\perp}{2J_2}$, where ϵ quantifies the departure from the degeneracy line $J_\perp = J_\parallel$. The full curves denote the continuum limit and the symbols are the (numerically obtained) exact solution. (a) 0.5 (b) 0.7 (c) 0.9 (d) 0.99.*
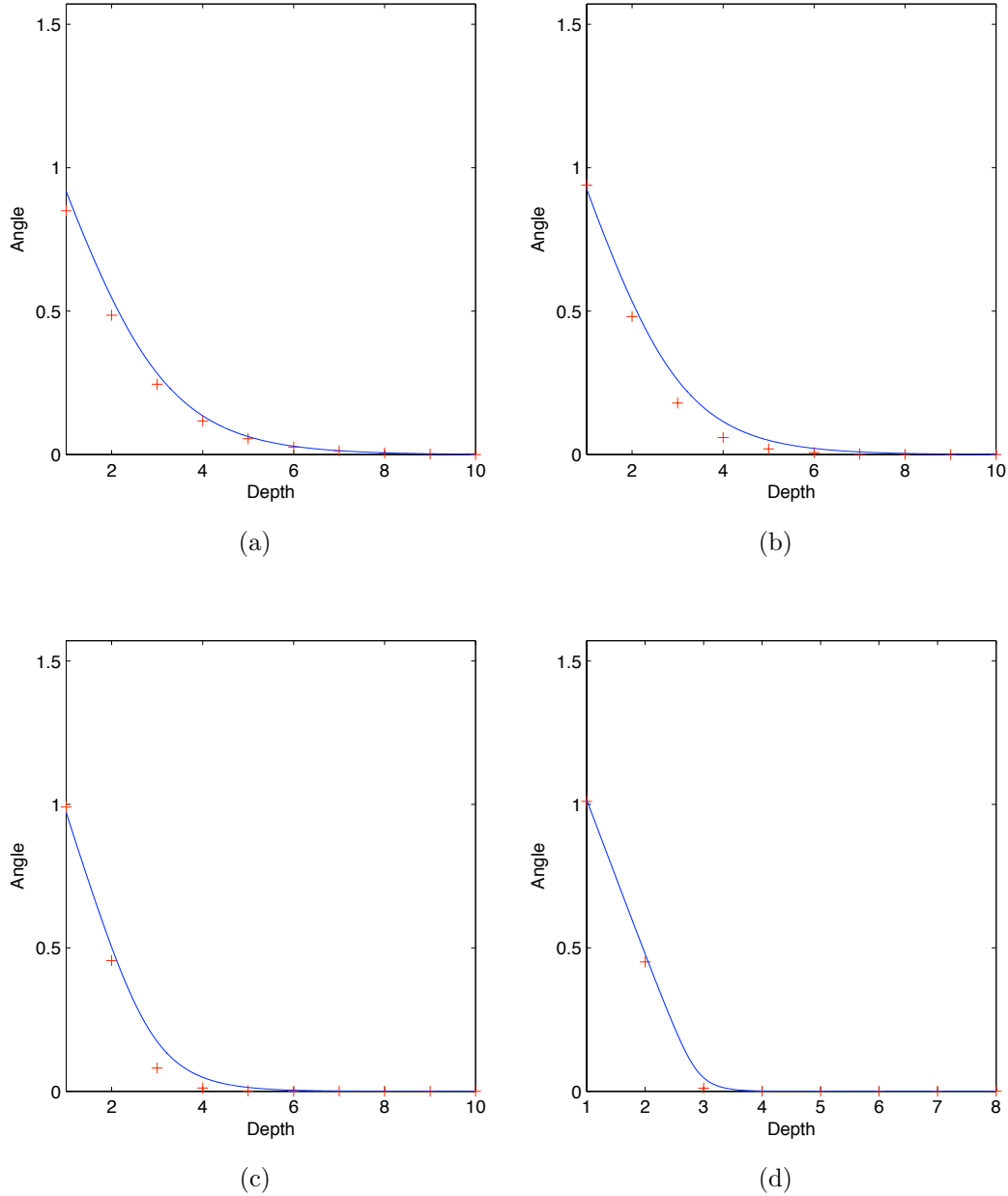
Figure 6.9: *A variety of angular profiles that describe the surface distortions for $\epsilon = 0.15$ for various values of the ratio $\frac{J_\perp}{2J_2}$, where ϵ quantifies the departure from the degeneracy line $J_\perp = J_\parallel$. The full curves denote the continuum limit and the symbols are the (numerically obtained) exact solution. (a) 0.5 (b) 0.7 (c) 0.9 (d) 0.99.*

solution of an essentially linear spiral for small n with the linearised solution taking over when the angle becomes small. The linearised solution becomes exact as the angle tends to zero and the exponential decay is controlled by Eq. (6.4.4). A larger value of $\epsilon = 0.15$ is chosen in fig. 6.9 and although the agreement is not always very good, the basic picture of the linear regime followed by the exponential regime remains valid.

In this section we have investigated the expected behaviour of a *pure* surface to the frustrated square lattice Heisenberg model. We have tuned the system off degeneracy, equivalent to employing a *fixed* magnetoelastic deformation and find that if this deformation is not too great, then the surface would be expected to reconstruct and a cap of the surface preferred phase would be expected to develop if the bulk phase was locally different. The depth of this surface phase appears to involve *two* length-scales, one over which the spins rotate linearly from the surface preferred phase to the bulk phase and then a second over which the residual spin distortion decays exponentially into the bulk. One can interpret the phenomenon as a phase boundary between the two phases which is bound to the surface. Additionally, due to the implicit magnetoelastic distortion, the distinct phases that can, under certain circumstances, form on the surface are *not* equivalent to each-other, and we have found a transition which is solely associated with the surface; where the surface phase transits from a single-q to a Néel state while the bulk retains the single-q character throughout.

6.8 FCC Lattices

Being three-dimensional, the face-centred-cubic lattice is geometrically more sophisticated than the square lattice but at its simplest level, the nearest-neighbour level, it involves fewer free parameters and is algebraically simpler. We shall show that the magnetic state that results from introducing a Cartesian surface to a FCC lattice with nearest neighbour coupling is in fact the solution to our square lattice model. Additionally, we introduce and solve for a non-trivial surface orientation designed to be a 'worst case scenario' whereby the different types of bond cut by the surface equal a net zero over the whole surface. This calculation shows the robustness of the phenomenon, since, contrary to initial expectations, the new order on the surface survives.

To model the surface reconstruction, we first remind the reader that we require two states with different symmetries *parallel* to the surface to be superimposed, as opposed to states with different symmetries perpendicular to the surface, as this translational symmetry disappears on the introduction of a surface and so has no meaning with respect to the order that we require if our surface reconstruction is to be realised.

6.8.1 Cartesian Surface

We introduce a Cartesian surface perpendicular to the z-direction, as in the previous convention for our square lattice model, and solve the resulting problem. We use a convention whereby coupling with a *component* in the direction perpendicular to the surface is labelled the $\tilde{J}_\perp$ coupling, and the remaining couplings, which are completely parallel to the surface are labelled $\tilde{J}_\parallel$ couplings, as before. The $\mathbf{k}_{min}$ for the nearest neighbour Heisenberg model of the FCC lattice were calculated in section 3.2.4, and turned out to be what we termed 'lines of degeneracy'. A magnetoelastic distortion of the lattice such that $\tilde{J}_\perp \neq \tilde{J}_\parallel$ breaks the degeneracy in such a

way that, for $\tilde{J}_\parallel < \tilde{J}_\perp$, the ground state corresponds to a single point, $(0, 0, \pi)$, and for $\tilde{J}_\parallel > J_\perp$, the $\mathbf{k}_{min}$ instead correspond to the lines of degeneracy described by $(\pi, 0, k_z)$ and $(0, \pi, k_z)$. These lines of degeneracy correspond to planes of Néel structure, orientated parallel to the surface. They possess a free parameter with respect to the quantisation direction defined in each plane, describing how the planes are magnetically independent from each other, a result of the Néel-type order imposed on the FCC geometry. In this way, the states are not affected energetically by the surface. Conversely, the surface 'hating' state, $(0, 0, \pi)$, looses energy at the surface. This is a result of the state consisting of planes containing ferromagnetically-aligned spins which therefore have coupling to neighbouring layers.

As such, only the $(0, 0, \pi)$ state is expected to be capped, and so we consider the case whereby the magnetoelastic distortion in the bulk finds the bonds parallel to the surface weakened and those perpendicular strengthened to stabilise this state in the bulk and investigate the superimposition of Néel sheets. The relevant Heisenberg model is

$$H = \tilde{J}_\parallel \sum_{<jj'>_\parallel} \mathbf{S}_j.\mathbf{S}_{j'} + \tilde{J}_\perp \sum_{<jj'>_\perp} \mathbf{S}_j.\mathbf{S}_{j'}. \qquad (6.8.1)$$

The surface distortion is described using just a single angle in each layer that describes the mixing between the underlying bulk magnetism, with amplitude $\cos\theta_n$, and an arbitrary-orientated (but perpendicular to the bulk) Néel component of amplitude $\sin\theta_n$. The second angle ϕ required to completely describe the spin direction is dependent only on the quantisation directions of the Néel planes we described above, and as such makes no contribution to the Heisenberg energy of our system. The energetics reduce down to (per spin in each layer)

$$E = 2\tilde{J}_\parallel \sum_{n=1}^\infty \cos 2\theta_n - 4\tilde{J}_\perp \sum_{n=1}^\infty \cos\theta_n \cos\theta_{n+1} \qquad (6.8.2)$$

and this is proportional to the energy of the previous model, given by Eq.(6.2.1), in the case that corresponds to the exact solution, $J_\perp = 2J_2$. One can understand this

correspondence by realising that we can transform the FCC lattice into our square lattice model through projection parallel to the surface, in directions where there is no spatial phase shift of the spin direction. The transformation corresponds to

$$J_2 = \tilde{J}_\perp \tag{6.8.3}$$

$$J_\perp = 2\tilde{J}_\perp \tag{6.8.4}$$

$$J_\parallel = 2\tilde{J}_\parallel, \tag{6.8.5}$$

where $\tilde{J}$ couplings are those of the FCC lattice, and J those of the square lattice. One can therefore map our FCC lattice to the case of $J_\perp = 2J_2$ of our square lattice. This is our exact solution case which was characterised by a linear or near-linear dispersion and additionally a finite number of planes where new order exists. The 'free' parameter in this mapping, $J_\parallel$, moves the model up and down this line in the square lattice phase diagram, specifically moving into regions where the surface reconstruction is predicted, and corresponds to the magnetoelastic distortion corresponding to $\tilde{J}_\perp \neq \tilde{J}_\parallel$. The degeneracy along this line in the square lattice, where both the non-oscillating and oscillating solutions can be superimposed in each plane with arbitrarily ratios, corresponds in the FCC lattice case to the free angle ϕ or in other words to the independence of the Néel planes that are superimposed onto the bulk state.

Following this proof of the equivalence of the FCC lattice and square lattice models, we therefore expect the surface distortion angle θ_n for FCC lattices to be essentially linear as we previously found for the square lattice model.

6.8.2 A Non-Cartesian Surface - Robustness to Non-Trivial Surfaces

So far we have examined Cartesian surfaces which are *optimal* for the surface reconstruction that we are investigating. The FCC lattice offers us another non-Cartesian

surface - the (110) surface - which has a preference for one state over another but not in an obvious way. Bond counting tells us that on average equal numbers of the two types of bonds are lost at the surface. As such, one might expect the system to be passive to the introduction of a surface. However, the surface layer has a biased distribution for which the bonds are lost, resulting in the system 'hating' the same 'capped' phase as with the previous case of a Cartesian surface, and as we now show, a distortion as depicted in figure 8 *is* stable.

The 'subtlety' relating to the slanted surface problem is that alternate layers have different numbers of broken bonds on the introduction of this particular surface, as can be seen in fig. 6.10, and as such react very differently to the surface. A determination of which state is preferred at the surface for each sublattice as a function of the coupling parameters is performed. Sublattice A prefers the Néel sheets described by the lines of degeneracy for a region on phase space that corresponds to the other state, $(0, 0, \pi)$, being the ground state in the bulk, and as such has a surface-preferred state with which it can lower its energy. Conversely, sublattice B does not prefer a different state on the surface from that in the bulk for any region of phase space, and as such there is an energy *cost* associated with using an orthogonal superposition of the two different states.

As such, we impose a superposition of the 'surface' state, the Néel planes, with the bulk state $(0, 0, \pi)$ only on sublattice A where energy can be gained by such a superposition, and note that, due to the Néel nature of the surface state, sublattice B is independent of this superposition and as such its spins remain invariant, taking on solely the bulk ground state all the way up to the surface.

We use the same labelling of couplings as introduced in the previous section as defined by a Cartesian surface, specifically so that $J_\parallel$ corresponds to the ferromagnetic direction and $J_\perp$ to the antiferromagnetic direction of the bulk state. In terms of our sublattices, this results in intra-sublattice bonds being $J_\parallel$ bonds and inter-sublattice bonds being $\perp$ bonds, and then the energy (per spin in the surface layer)
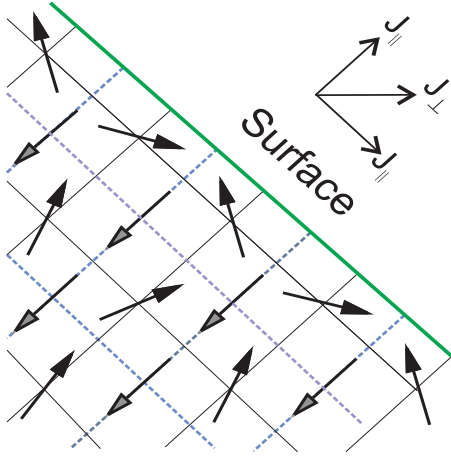
Figure 6.10: *Magnetic distortion close to a (110) surface. The hatched spins, residing on sub-lattice B, which remain passive to the surface, are in neighbouring layers to the spins on sublattice A, which rotate to take on a Néel state,.*

is

$$E = J_\parallel \sum_{n=1}^{\infty} \cos 2\theta_n + J_\parallel \sum_{n=1}^{\infty} \cos(\theta_n + \theta_{n+1})$$
$$-4J_\perp \cos\theta_1 - 8J_\perp \sum_{n=2}^{\infty} \cos\theta_n, \qquad (6.8.6)$$

where we ignore the energy of the spins that remain invariant.

This energy is optimised by solving

$$\sin(\theta_{n+1} + \theta_n) + \sin(\theta_{n-1} + \theta_n) = 4\sin\theta_n \left[2\frac{J_\perp}{J_\parallel} - \cos\theta_n\right] \qquad (6.8.7)$$

subject to the boundary condition

$$\sin(\theta_0 + \theta_1) = 4\frac{J_\perp}{J_\parallel}\sin\theta_1 \qquad (6.8.8)$$

and linearisation provides a phase boundary when $\frac{J_\perp}{J_\parallel}=3\text{-}\sqrt{5}$ and a decaying solution

$$\theta_n = \theta_0 \left[\sqrt{5} - 2\right]^n. \qquad (6.8.9)$$

As such, we find that even for this case, whereby one would naively expect no reconstruction due to the material having *overall* an equal number of each type of bond lost at the surface, a surface reconstruction is in fact expected.

6.9   General Considerations

Although we have analysed the square lattice in much detail, many of the funda-
mental ideas are likely to be relevant to *all* such multiple-q systems. Firstly, for a
Heisenberg model with a pure surface we can Bloch transform parallel to the surface
to generate

$$H \equiv \sum_{n=1}^{\infty} \sum_{n'=0}^{\infty} \sum_{\mathbf{q}_{\parallel}} J_n^{n'}(\mathbf{q}_{\parallel}) \mathbf{S}_n(\mathbf{q}_{\parallel}).\mathbf{S}_{n+n'}^*, (\mathbf{q}_{\parallel}) \qquad (6.9.1)$$

which offers the critical conclusion that spin density from different values of $\mathbf{q}_{\parallel}$
are *independent*. We apply this result to our surface phenomenon to understand
the energetic considerations in detail. A distinct surface phase is associated with
a distinct $\mathbf{q}_{\parallel}$ from that of the bulk phase and consequently, from the above proof,
is independent from the bulk phase. Given that the bulk order is guaranteed to
maintain its symmetry parallel to the surface from layer to layer, the surface phase
must be superimposed, and specifically, since the two phases have different spatial
structures *parallel* to the surface, the constraint of fixed spin length on each site
invariably forces the two phases to be associated with orthogonal spin orientations.

The energetic considerations in having a surface phenomenon can hence be sim-
plified down, as a result of the independence of the surface phase from the bulk
phase, to the statement that the surface phase need to only be *self-sustaining*, the
details of which we will now discuss.

In order to be self-sustaining the magnetic phase bound to the surface must be
very low energy intrinsically. Specifically, since the surface phase is *not* the bulk
ground-state it needs to gain more energy at the single surface layer than *all* the
bulk state that it replaces over the region in which it exists. The closer the surface-
state energy to the bulk-state energy, the deeper the surface state can penetrate into
the bulk. For a general multiple-q system, the distinct single-q states are degenerate
for the pure model and consequently the system would be expected to choose its
preferred state at the surface, which corresponds to the surface state descending

infinitely far into the bulk. It is the magnetoelasticity and magnetoanisotropy terms that lift this degeneracy and provide the length-scale over which the surface phase is stabilised. The magnetoelasticity provides an energy scale for the distortion from degeneracy, $J_\perp - J_{||}$, and this in turn is the energy scale for the cost of adopting the surface state within a parameter regime in which it is not a ground state of the bulk.

In transition metals the magnetoelastic energy is not large in comparison with the intrinsic magnetic energy, there being an order of magnitude separation between them, and so we might expect a surface phase over many layers. Conversely, in rare-earths and actinides, the magnetoelasticity is quite large and so no surface phase is expected. However in rare-earth and actinide systems like CeAs and UO_2 the magnetoelastic distortion required to achieve deformations from single-q to multiple-q is surprisingly small.

The effect that the magnetoanisotropic energy may have on the stability of the phase has not been quantified in this investigation, but, coupled with magnetoelastic energy scale considerations, we expect a surface phase to form for any system for which this magnetoanisotropic energy is small in comparison to the intrinsic magnetic energy. As a result, actinides and rare earths may not be prime candidates for the phenomemon, due to the presence of large anisotropy in these systems.

Since all multiple-q systems have an intrinsic degeneracy between the different single-q orientations, which is only lifted on a smaller energy-scale, we might expect all such systems to exhibit the phenomenon of a preferred surface phase capping the bulk domain structure.

Chapter 7

URANIUM DIOXIDE: MAGNETIC SURFACE RELAXATION

In this chapter we investigate the effect of introducing a surface to uranium dioxide, an actinide FCC geometrically-frustrated magnetic system that adopts a 3-q state in the bulk. The investigation is motivated by the findings of an x-ray resonant magnetic scattering experiment that uses the large resonant enhancements at the uranium M_{IV} absorption edge [49]. In addition to the unusual behaviour of the surface, which orders *continuously* in the presence of a *discontinuous* ordering of the bulk, unusual disordering behaviour is observed at a temperature lower than the bulk magnetic ordering temperature, and it has been proposed that the behaviour could be a phase transition.

After discussing results of experiments performed on UO_2, an appropriate model is constructed and the ground state found, which exhibits a magnetic reconstruction due to the ability of multiple-q states to compensate for the introduction of impurities such as a surface. The domain wall associated with this and also an order-disorder domain wall will be discussed with respect to the disordering behaviours found by experiment.
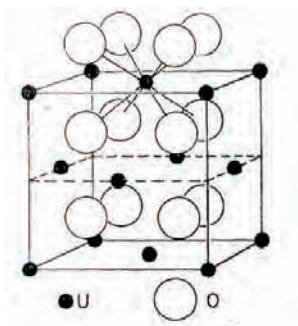
Figure 7.1: *Crystal structure of UO_2 - fluorite type CaF_2. The uranium atoms, surrounded by 8 oxygen atoms, are in the FCC structure [7]*

7.1 Literature Review for Uranium Dioxide

7.1.1 Electronic and Magnetic Structure

Above the magnetic ordering transition temperature $T_N = 30.8K$, Uranium dioxide is a paramagnet with a FCC fluorite structure, CaF_2, as shown in fig. 7.1. The uranium atoms, which take an FCC lattice structure, are surrounded by 8 atoms. The magnetism present below T_N is a result of the electrons that reside in the partially-filled orbitals of the uranium atoms which only undertake virtual hopping. The resulting magnetic moments form a type-1 antiferromagnetic structure. In terms of the electronic structure, the tendancy to fill a shell is incredibly strong in oxygen and so the oxygens become O^{2-} ions. The uranium therefore exists in the compound as U^{4+}, having an electron configuration $[R_n] + 2\acute{e}$, describing a fully-occupied shell of the noble gas plus a partially filled shell containing 2 electrons. These electrons reside in the 5f, the other options of the 7s or 6d shell having too great a radial extent and therefore costing electrostatic repulsion with the strongly-negatively-charged oxygen ions. The very small extent of the f-orbitals causes there to be very little crystal field dependence and so there is no large distortion caused by the magnetism. The occupation of the 5f rather than 7s or 6d shell has been experimentally verified according to the large angular extent of the form factor [7] [50]. Investigation of the intensities of the Bragg spots via the form factor also gives information about the

155
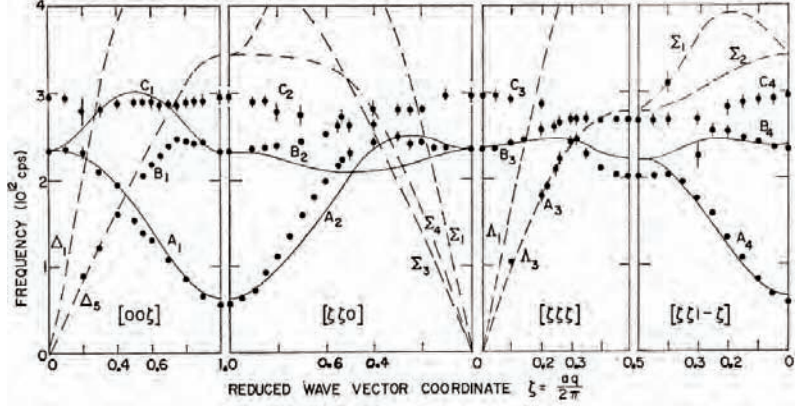
Figure 7.2: *Spinwave dispersion for UO_2 for $9K$, propogating along four high symmetry directions. The dashed curves show the phonon dispersion curves appropriate to $296K$. The solid curves are the result of a least squares fitting procedure in which the experimental measurements are assigned labels according to Cowley and Dolling's model AB [22]*

spin orientation within the system, which can be determined using knowledge of the vanishing of certain Bragg spots. Faber *et al*'s measurements indicate UO_2 to be a *transverse* rather than longitudinal triple-q magnet [51]. As such, the spin density vectors $\mathbf{s_k}$ are directed perpendicular to the propagation vector $\mathbf{k}$, and this leaves two styles of S-type domain[51], as discussed in section 4.1.

In terms of the spin configuration, there has been some confusion as to which of the MSDW states the bulk takes, as discussed in section 4.1. However, the system is now known to take a triple-q state in the bulk, and this spin configuration explains the phonon-magnon hybridisation observed in the dispersion. The spinwave spectrum for UO_2 is shown in fig. 7.2 for $9K$ and one can clearly see the result of phonon-magnon coupling in the region of [0 0 0.5], where the dispersion has been 'pulled away' from crossing, or rather, the lowest branch has been split. It can be shown that phonons and magnons couple if the magnetic state is non-collinear - due to the non-collinearity of the spins, fluctuations couple in a perpendicular fashion to the spin moment and interact to make the spin length fluctuate accordingly.

We now determine the total angular momentum associated with the spin of each uranium ion, which allows us to validate the use of classical spin vectors rather than the quantum case. Each electron's spin and angular momentum are defined

156
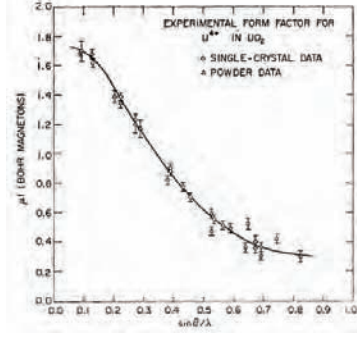
Figure 7.3: *Magnetic form factor for U^{4+} in UO_2.Reproduced from [7]*

as $s_1 = s_2 = 1/2$ and $l_1 = l_2 = 3$, being f-electrons. The total spin S and angular momenta L the system can take are given by the ranges $|s_1 - s_2| \leq S \leq |s_1 + s_2|$ and $|l_1 - l_2| \leq L \leq |l_1 + l_2|$. Hund's rules then apply. The first two rules plus consideration of Fermi-statistics result in the system adding the spins to make the maximum spin of $S = 1$, and the maximum angular momentum $L = 5$. $L = 5$ rather than 6 since the state $|L, L_z >= |6, 6 >$ is not allowed since this corresponds to both electron states being identical. Since the relevant shell is less than half-filled, the application of Hund's third rule results in the total momentum $J = |L - S| = 4$. Thus, the total number of ground states of the system in the absence of interactions between atoms is 9.

The crystal field of UO_2 in its paramagnetic state, i.e. in the absence of magnetic interactions, splits these 9 states such that the lowest energy states form a triplet; specifically aΓ_5 triplet.

Due to the uncertainty in the ground states taken by the uranium moment at low temperature, we stop the analysis here, and instead look to clues from experiment in order to determine how best to model the system. The complication related to uranium is a result of the total moment consisting of two electrons each residing in the f-shell, and as such there is a large number of combinations of the spin, angular momentum and spin-orbit coupling degrees of freedom that must be considered, especially as it is not clear whether the breaking of degeneracy by Hund's third

rule is in fact accessible energetically, or whether other magnetic interaction effects prevent this and instead cause a rearrangement of the previously-specified ground states to new levels and degeneracies. Any determination of the magnetic exchange interactions required in order to set up a model is best tackled with knowledge of the moment's individual spin and angular momentum values rather than the total moment so as selection rules can be applied. This procedure becomes far too complex for us to follow in the case of uranium dioxide and so our model will be based on experimental observations, as explained later.

Since even quantum-mechanical spin vectors can be made to point in any direction, a picture using classical spin vectors is still valid. For example, for a spin $1/2$ system, a spin in any direction can be represented in the eigenstate-of-$\hat{s}^z$-basis as the linear combination

$$|\psi(\theta,\phi) >= e^{-\frac{i\phi}{2}} \cos\frac{\theta}{2}| \uparrow > +e^{\frac{i\phi}{2}} \sin\frac{\theta}{2}| \downarrow>, \tag{7.1.1}$$

where the direction of the spin is defined in the regime of spherical polar coordinates as (θ,ϕ).

The difference between a classical model and the quantum-mechanical reality of a system comes about from the probability distribution of the direction of a spin. For a classical model, the spin points in the direction it is represented as with a probability of one. For a quantum mechanical spin vector however, even in its eigenstate of for example $\hat{s}^z$, there is still a finite probability that the spin is simultaneously pointing in the s^x and s^y directions, which is a result of the commutation relations of quantum mechanics. This manifests as $(s_z^{max})^2 < S(S+1)$. For example, for spin $S = 1/2$, the expectation value of the θ value of the spin, as measured from the $z-axis$, is given by

$$< \psi(\theta\phi)|\hat{s}_z|\psi(\theta\phi) >= \cos\theta, \tag{7.1.2}$$

where the the spin is in state $|\psi(\theta\phi) >$ as defined in eq.7.1.1, which can be though of as the eigenstate of $\hat{s}_{\theta,\phi}$. Thus the probability of a spin pointing a deviation (θ/ϕ) from a basis vector of which it is an eigenstate goes like $\cos^2\theta$.

The value s_z^{max} approaches the value of S^2 as S is increased. The probability distribution of the spin direction as a function of deviation from the z-direction gets much less broad as the total spin value increases. Thus, a larger total spin moment brings more agreement with the classical model.

Bulk First Order Transition

UO_2 is believed to undergo a first order transition from paramagnetic to antiferromagnetic at the Néel temperature 30.8K, as can be seen in fig. 7.4 [7]. Although the magnetisation goes discontinuously in close proximity to the ordering temperature, it seems to be second-order-like, since the spinwaves are seen to soften at the magnetic Bragg reflections towards zero as the temperature approaches the ordering transition temperature, indicating a sharp but nevertheless continuous transition.This behaviour can be seen in figures 7.5 and 7.6.
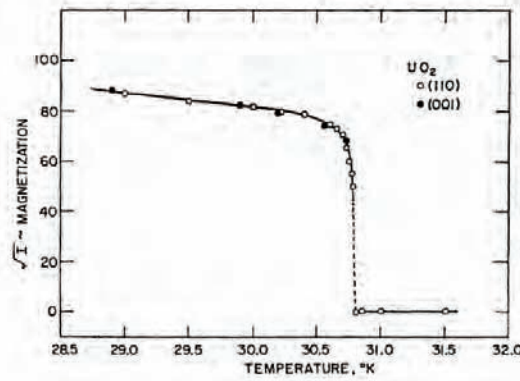
Figure 7.4: *Details of neutron measurements through the Néel temperature. Data scaled to 100 at 5°K. Reproduced from [7]*
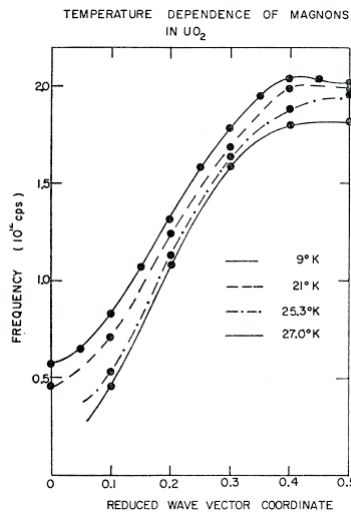
Figure 7.5: *Temperature dependence of the $[\xi\xi 1-\xi]$ branch of lowest frequency. The spinwave gap at (001) can be seen to soften with increasing temperature.[8]*
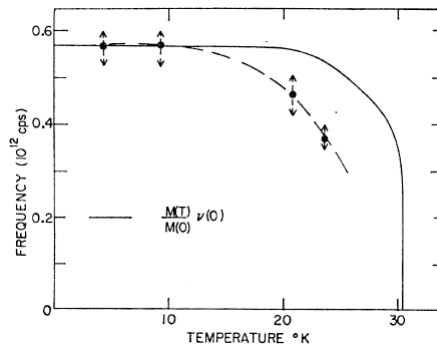
Figure 7.6: *Temperature dependence of the lowest frequency mode of excitation at $q = (001)$ compared with that of the intensity of a Bragg reflection.[8]*

160

7.2 Experimental Results of Langridge *et al* and Interpretation

Here we present the results of the experiments by Langridge *et al* [49] and Watson *et al* [13] on the (001) surface of UO_2. We begin by covering some background that is required in order to interpret the measurements.

The depth of the probe can be tuned via the grazing angle, which alters the reflection coefficient when the incident angle is near to the critical angle of the material. Specifically, below the critical angle, a purely evanescent wavefield with an exponential-like decay as a function of depth is set up inside the sample [45].

Additionally, the magnetic scattering can be enhanced by using photon energies that are tuned near to the U M_{IV} edge. The number of photons contributing to the cross section that have undergone a scattering process is increased via the resonant process in which the photon is absorbed and re-emitted. Furthermore, due to the magnetic splitting of the energy level associated with this process, the tuning of the photon energy to near the U M_{IV} edge results in the transitional probability associated with the absorption and re-emission of the photon to favour a particular spin direction. Thus, the magnetic part of the scattering is enhanced.

We shall discuss the different measurements acquired using this technique that are paramount to the experiments we are interested in.

7.2.1 Specular Reflection

We conduct a back-of-the-envelope derivation to illustrate how the scattering amplitude is affected by the loss of translational symmetry in a direction and also the depth profile associated with how the x-rays penetrate the system, taking into account that the contribution from each plane to the intensity measured by the detector decreases with depth, specifically as pure exponentials. It is the structure factor, $S(\mathbf{q})$ that controls the variation in intensity of the scattering, and is given by

161

$$S(\mathbf{q}) = \sum_j f_j(\theta) e^{i\mathbf{q}.\mathbf{R}_j}, \tag{7.2.1}$$

where j labels points on the lattice, and hence $\mathbf{R}_j$ is the location of the lattice sites, $\mathbf{q}$ is the difference in incoming and outgoing wavevectors and $f_j(\theta)$ is the scattering amplitude of a scatterer. In defining the structure factor in this way, we have made several assumptions; that all scatterers are identical, that the scattering is weak so that only single-scattering events occur, and that we can take the limit of the distance at which the observation of the cross section as infinity. Ignoring the structure of each of the scatterers and treating them instead like point scatterers, we tackle the structure factor form by assuming translational symmetry of the magnetism parallel to the surface and hence Bragg scattering and are left with the sum over the layers that the x-rays penetrate:

$$\sum_j e^{i\mathbf{q}.\mathbf{R}_j} = \sum_j e^{iq^z R_j^z} \sum_l e^{i\mathbf{q}^\parallel.\mathbf{R}_l^\parallel} = N_\parallel \sum_{\mathbf{G}_\parallel} \delta_{\mathbf{q}_\parallel,\mathbf{G}_\parallel} \sum_j e^{iq^z R_j^z}, \tag{7.2.2}$$

where we have used the identity 2.4.2 for the parallel term where translational symmetry is present and primitive vectors can be used to label each point within this quasi-2D lattice of the parallel component. The attenuation of the probe with depth is incorporated by using a complex 'propagation' vector:

$$q^z \rightarrow q^z - i\delta, \tag{7.2.3}$$

where δ is a small parameter. Representing R^z with respect to the lattice parameter in this direction, a^z, so that $R^z = ja^z$, we can perform the remaining sum over j to provide

$$\sum_{j=0}^{\infty} e^{iq^z R_j^z} = \sum_{j=0}^{\infty} e^{-iq^z ja^z - ja^z \delta} = \frac{1}{1 - e^{-iq^z a^z - a^z \delta}}, \tag{7.2.4}$$

162

where the summation of j from *zero* to ∞ takes care of the presence of the surface. Squaring this last expression leads to the intensity in the direction perpendicular to the surface:

$$I^2[q^z] = \frac{1}{1 - 2\cos(q^z a^z e^{a^z \delta}) + e^{-2a^z \delta}} = \frac{e^{a^z \delta}}{2[\cosh(a^z \delta) - \cos(q^z a^z)]}. \qquad (7.2.5)$$

The Bragg spots of an infinite crystal are thereby modified due to the attenuation with depth of the scattering power into a collection of peaks along a truncation rod (TR). As δ is decreased with respect to q^z, so the probe penetrates further into the bulk. As $\delta \rightarrow 0$, we gain back the profile of Bragg spots, as the peaks get sharper and converge onto δ-functions. The case of no absorption, $\delta = 0$, returns the form as described by Robinson and Tweet of

$$I^2[q^z] \sim \frac{1}{\sin^2(q^z a^z / 2)}. \qquad (7.2.6)$$

As such, it is the structure *between* the locations that the Bragg spots would take in a non-truncated system that provides information about the near-surface layers of the sample. Due to the inverse nature of the Fourier transform from real to reciprocal space, a less-severe truncation of the surface corresponding to the broadening of the step function leads to a sharper decay from the Bragg point of the intensity profile. This often occurs for real chemical surfaces, where there may be adatoms, steps etc.

Thus, the contribution to the intensity profile from the bulk is centered around $q_z = \frac{2\pi m}{a_z}$ and the near surface contributes to the other q_z regions. In order to determine how the order parallel to the surface is behaving both within the near surface and within the bulk, one can perform and contrast scans taken in q-space parallel to the surface direction both at $q_z = \frac{2\pi m}{a_z}$ and off this value of q_z, in order to pick up either bulk or near-surface contributions respectively. However, due to the finite attenuation of the probe, it is not solely the bulk that contributes to the
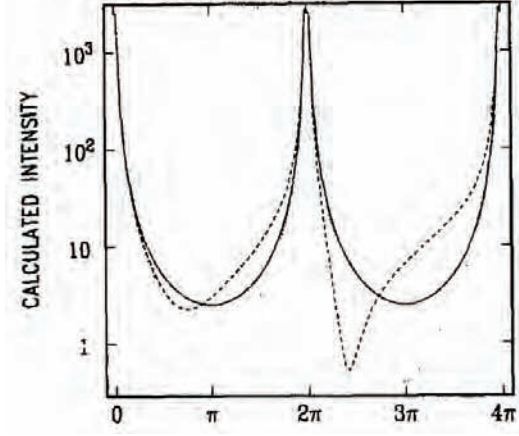
Figure 7.7: *Crystal truncation rod profiles. The full curve shows the CTR for a perfect surface, the dotted curve for a rough surface (eq. 7.2.7).Reproduced from [52]*

scattering located at $q_z = \frac{2\pi m}{a_z}$, but also the surface, and so care must be taken - we can only compare and contrast rather than get information solely about the bulk and vice versa.

The resulting intensity distribution is shown in fig. 7.7. The figure also includes the more realistic example of a non-smooth surface; specifically, using the model of a 'statistically rough surface'. The height of the surface is modelled by an exponential distribution - layer zero is assumed to be fully occupied layer, 1 above it has a fraction β of sites filled, layer 2 has fraction β^2 filled etc. This leads to a modification of the CTR intensity by an additional factor:

$$I_{rough} = I_{CTR}\frac{(1-\beta)^2}{1 + \beta^2 - 2\beta\cos\left(q^z a^z\right)}. \tag{7.2.7}$$

The discussion so far has assumed no in-plane correlations. For this case of no in-plane correlations, the intensity removed from the TR would be distributed uniformerly over reciprocal space as a flat background. The effect of the system possessing in-plane correlations causes the flat background to instead become peaked at the same in-plane positions as the peaks in the TR, with a width inversely-related to the in-plane correlation length. The scattered intensity is therefore a sum of that

due to the in-plane scattering which contributes sharp peaks due to the translational symmetry, and 'diffuse' scattering associated with the truncation of the surface and also thermal and impurity effects etc.

Lateral Magnetic Order and Lineshapes

The results of particular interest in the following sections are those of Langridge *et al*[49], whereby scans *across* the truncation rods are performed. One can obtain important information from the resulting lineshapes of these intensity profiles, by relating the lineshapes to correlation functions and hence to thermodynamics present with respect to the direction parallel to the surface. This is in contrast to the specular reflection discussed above, which obtains information about the depth profile of the average magnetisation

If the system were perfectly periodic, void of domain structures, defects, thermal fluctuatios, dislocations etc., then one would obtain δ-functions in this direction, and the system would have correlations of infinite range. These impurities serve to broaden the peaks as the correlations become weaker, and the particular shape of the peak gives information about the type of order or disorder present.

It can be shown [52] that the electron density-density correlation function, $C(\mathbf{r}) = \langle \rho(\mathbf{r})\rho(0) \rangle$, can be related to the integrated intensity $I_{\mathbf{q}}$ measured in reciprocal space by

$$C(\mathbf{r}) = \int I(\mathbf{q})e^{i\mathbf{q}.\mathbf{r}}d^3q. \qquad (7.2.8)$$

Interpreting the entire correlation function from the entire integrated intensity profile is complicated. Even though one may only have short range interactions present, between for example nearest and next-nearest neighbours only, a correlation will still exist at further distances than next-nearest neighbour. Thus, even if a

correlation exists, there is *not* a simple relationship that indicates the interactions present in the system.

In order to assess whether long range order is present, one can examine the lineshape of $I(\mathbf{q})$, the inverse fourier transform of the correlation function which is the scattering normalised to the system size. If I(q) diverges with system size at some q, then this is indicative of long range correlations existing. Consider the definition of

$$I(q) = \int_{-\infty}^{\infty} c(r)e^{-iqr}dr. \tag{7.2.9}$$

If the correlations in real space do not decay to zero at a large enough rate with r, which indicates long range correlations, then the integral must diverge with increasing system size. This defines the presence of long range correlations, since the contribution is relevant for all r up to the system size even as the system size tends to infinity. Thus, given the limits of 7.2.9, a system possessing long range correlations possesses a divergent I(q) function:

$$\lim_{N\to\infty} I(q=0) = \lim_{N\to\infty} \int_{-N}^{N} c(r)d^3r = \infty. \tag{7.2.10}$$

The divergence of I(q) at some q does not necessarily indicate long range *order* however - a system is long range ordered only if the contributions to the correlation function are *identical* for all r, such that the correlation is linearly proportional to system size. The form of $I(q)$ must therefore be examined in order to determine whether long range order exists. This is achieved by taking the integral around the Bragg spot at which long range correlations appear:

$$\lim_{\delta q \to 0} \int_{-\delta q}^{+\delta q} I(q) \qquad\qquad (7.2.11)$$

and determining if the integral is equal to a constant, indicative of a delta function, or zero, indicating no long range order is present. In a perfect system, in the absence of impurities, thermal fluctuations etc. the long range order shows up as a δ-function in the ($\mathbf{q}$) profile, since this corresponds to a flat correlation function $c(r)$, which in turn corresponds to the correlation function having equal contributions from all length scales. In addition, for a δ-function, the resulting finite value for the integral 7.2.11 is proportional to the system size, and so all scattering, which is proportional to system size, is located under this area. For a system with long range correlations but no long range order, the correlations are a function of system size, *but* not in a linear fashion - the correlations decay as a function of r, but not 'fast'enough for the contribution to the correlation to be irrelevant at a certain distance - all spins correlate to some degree up to an infinite seperation of spins.

A third case concerns no long range correlations and corresponds to any q that is not located at the divergent peak of I(q). For a particular q, I(q) can be considered to be a measure of the amount of the corresponding spin spiral present in the system, from 7.2.9, where $c(r)$ can be considered to be a probability/ or weighting, to each spiral present in the spin state. For a quantum spin state, the ground state consists of a linear superposition of spin spirals due to the presence of quantum fluctuations which lower the energy of the system further from the classical configuration. As such, there exists non-zero I(q) and the peak broadens due to the presence of long-wavelength spin spirals in the ground state. The I(q) does not diverge at these points, and instead converges with respect to system size, with the length scale of convergence corresponding the length scale at which the correlations die away, or in other words the range of the short range order.

Due to the finite size of experimental materials, the presence of domains, dislocations, etc., the spin density of real materials possesses additional structure to a delta-function as the scattering gets thrown between the Bragg spots of the pure system. In addition, non-zero temperature contributes structureless diffuse scattering as a flat background. As such, the spin density is moved into a broader profile whose width is inversely-proportional to the in-plane correlation length[53], and which consists of a diffuse contribution plus the original delta-function contribution from the long-range-ordered system. For real systems therefore, the profile $I(q)$ can have a complicated structure. As such, one examines the long range correlation behaviour by analysing the profile $I(q)$ near the peak in question, which corresponds to analysing the behaviour of tail of the correlation function $C(r)$. If $I(q)$ diverges near the peak, then it follows that $C(r)$ must also diverge and long range correlations are present.

This can be understood by considering the correlations having, for example, a power-law-like tail at large distance. A power-law tends to zero slower than, for example, an exponential, and so the correlations are finite and fall to zero with a longer length scale than for example an exponential tail would. Next consider expanding the correlation function around large r, given that it takes a power-law form *plus* corrections due to, for example, short range correlations, defects of the crystal etc that are represented by a Taylor expansion:

$$c(r) \sim \frac{1}{r^\alpha} \left(a + b\frac{1}{x} + c\frac{1}{x^2} + ... \right). \tag{7.2.12}$$

The fourier transform of this leads to a form

$$I(q) \sim \frac{1}{q^{1-\alpha}} \left(a + bq + cq^2 + ... \right) \tag{7.2.13}$$

and as such, in order to study the long range order in the absence of the diffuse scattering component, one considers the form of I(q) close to $q = 0$ (or, in the case of antiferromagnetic ordering for example, around the $q = \pi$ point.

Thus, if the $I(\mathbf{q})$ profile near the peak is a power law, the correlation function tail will also follow a power law; if the intensity profile is a lorentzian, the correlation function tail will follow an exponential, and thus will be correlated over smaller distances. Different lineshapes and their corresponding correlation function profiles, being inverse fourier transforms, are shown in fig. 7.8. The profiles provided by [52] accompany the derivation of the height-height correlation function $\langle (h(\xi) - h(0))^2 \rangle$ in real space associated with the roughening transition from that of the intensity profile, where

$$I(q_x, q_z) = \sum_{\xi}^{N} e^{iq_x a_1 \xi} c(\xi) \tag{7.2.14}$$

and $c(\xi)$ is the gaussian quantity

$$c(\xi) = e^{-\langle (h(\xi) - h(0))^2 \rangle a_3^2 [q_z]^2 / 2}. \tag{7.2.15}$$

However, we can apply the illustrations to our magnetic correlations. Comparing to our procedure of simply fourier transforming the electron density-density correlation function to obtain the intensity profile, we point the reader to the second and third columns of fig. 7.8 in order to illustrate the relevant relationships. Figure (a) represents a correlation function with an exponential decay, which corresponds to short range order. One can observe that the faster the exponential decay, the broader the peak of the Lorentzian lineshape. For correlations with a flat profile (b), LRO is present and one can see this as a Dirac delta-function as mentioned previously. Figure (d) concerns correlations with an algebraic decay, or rather, a power

law form. The fourier transform is another power law but with an inversely-related power to the untransformed power law. For our analysis of the UO$_2$ results, the power $\eta < 1$ and so the lineshape is always a decay. The correlations decay over the characteristic length scale η but do not diverge linearly with the system size and as such do not correspond to long range order.

One must however take care - we study only the small region around the intensity peak which gives us information about the tail of the correlation function and *not* the whole function as this comprises of non-trivial dependencies on distance. This can be understood simply by figure (c); a correlation function with multiple-dependencies on distance presents itself in the intensity profile as a sharp peak plus a broader peak, relating to the long range and short range correlations respectively. The behaviour of the correlations at short range is represented by the behaviour of the intensity profile away from the peak and thus corresponds to the broader contribution. An example can be seen in the intensity profiles of experiments on the Cu$_3$Au surfaces, as shown in fig. 5.14.

We run through examination of the particular lineshape we shall be interested in: that which describes the lateral correlations in a 3D system. The lineshape near the peak is therefore a function of a 2D variable $\mathbf{q}_{\parallel}$, and for the case we shall be studying is given by the circularly-symmetric function that follows a power law:

$$I(\mathbf{q}_{\parallel}) = |\mathbf{q}_{\parallel}|^{-\eta}. \tag{7.2.16}$$

The correlation function corresponding to this lineshape is given by

$$c(\mathbf{x}) \quad = \quad \int_{-\infty}^{\infty} d\mathbf{x} |\mathbf{q}_{\parallel}|^{-\eta} e^{i\mathbf{q}_{\parallel}\cdot\mathbf{x}}. \tag{7.2.17}$$

$$\tag{7.2.18}$$
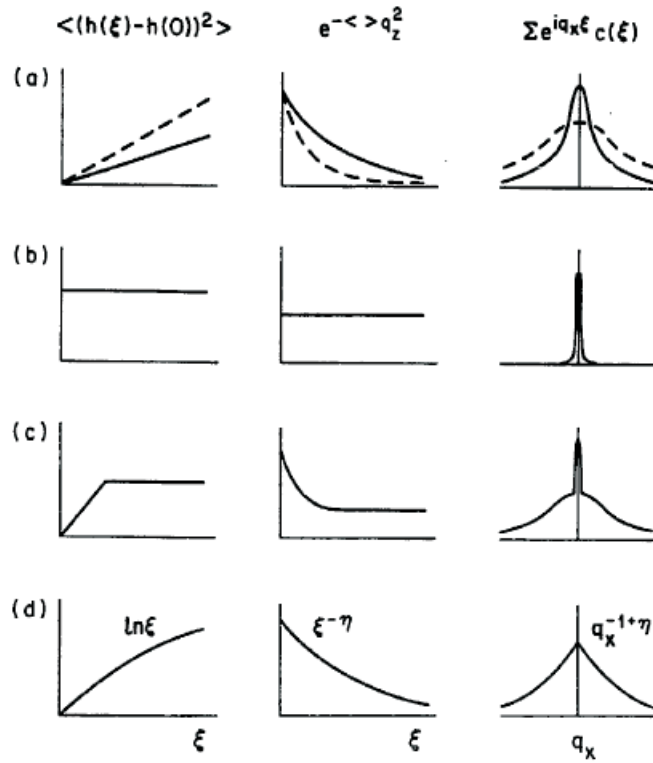
Figure 7.8: *Cross-sectional lineshape of crystal truncation rods from a rough surface represented by different height-height correlation functions. The left column is the lateral dependence of the height-height correlation function. The middle column is the correlation function $C(\xi)$ obtained with equation eq. 7.2.15. The right column is the Fourier transform of $C(\xi)$ which is the cross-sectional lineshape according to eq. 7.2.14[52].*

171

Given that $\mathbf{q}_\parallel.\mathbf{x} = r|\mathbf{x}|\cos\theta$ and making the substitution $R = r|\mathbf{x}|$,

$$= \int_{-\infty}^{\infty} d\theta \frac{dR}{|\mathbf{x}|} \left(\frac{R}{|\mathbf{x}|}\right)^{1-\eta} e^{iR\cos\theta}. \qquad (7.2.19)$$

As such, the correlation function $c(r) \sim |\mathbf{x}|^{\eta-2}$. The inverse relationship of the powers with respect to the correlations and the lineshape indicates that the smaller η is, the larger the length scale over which the system is correlated; or in other words, a decreasing η value corresponds to a decrease in disorder present in the system. Power law correlations are significant since they occur when a system is at or near criticality, where fluctuations are present over all length scales.

XRMS signal

A final note concerns the type of correlations discussed in the following experiments. The integrated intensity measured, referred to as the X-ray Resonant Magnetic Scattering (XRMS) signal, correspond to *static* spin-spin correlation functions, in the same way as for neutron scattering cross sections. Spin-spin correlation functions are defined in reciprocal space as $\langle \mathbf{s}_\alpha^*(\mathbf{q}, \omega)\mathbf{s}_\alpha(0,0)\rangle$, where $\mathbf{s}_\alpha$ is a spin direction component of $\mathbf{s}$ and the average is a thermal average. For their experimental geometry, the XRMS signal is sensitive to the component of the uranium moment parallel to the scattered wavevector, which is primarily in the surface. As such, the correlations measured are with respect to the component of the spins that lie in the xy-plane. The spin-spin correlation function covers any correlations found in both elastic and inelastic scattering, whereby correlations between spins undergoing excitations described by ω are also included. The static case of elastic scattering that the following experiments measure corresponds to $\omega = 0$.
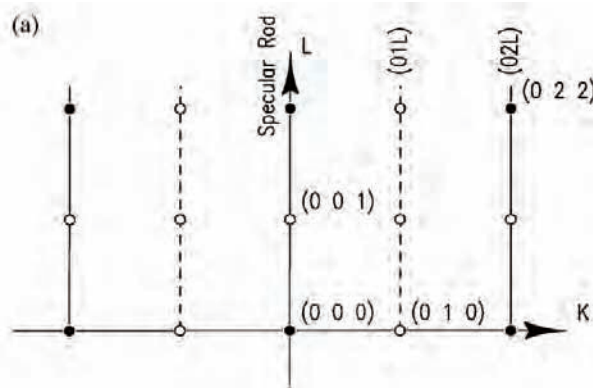
Figure 7.9: *Reciprocal space map for the UO₂ (001) surface showing chemical (solid circles) and magnetic (open circles) bulk Bragg reflections and mixed (solid lines) and magnetic (dashed lines) truncation rods. Reproduced from [13]*

7.2.2 Experimental Results

We now turn to the results of the experiments. The scattering geometry of the two experiments is shown in fig. 7.9. Both experiments are carried out using a glancing incidence, whereby the incident and exit angles of the x-ray beam to the surface are near the critical angle for total external reflection, $\alpha_c \sim 0.75 \deg$.

Figure 7.10 shows a dramatic difference between the magnetic order parameter in the near-surface versus the bulk. It may be shown that the measurements at positions $(0, 1, 0.075)$, $(0, 1, 0.15)$ and $(0, 0, 1)$ correspond to penetration depths of 50, 120 and 850$\mathring{A}$. The bulk shows a discontinuous transition at the Néel temperature of 30.2K, as is well-known [7]. The magnetic order parameter for the near-surface however decreases *continuously* as the Néel temperature is approached from below, with a power-law dependence on the reduced temperature. The surface ordering temperatures are equal to within $\pm 0.5K$ of the bulk.

Watson's findings suggest that the magnetic structure begins to disorder in the near-surface at a temperature *below* the bulk first order transition temperature. The structural order-disorder transition of [47] that we visited in section 5.3 which is interpreted as an interface delocalisation transition shows the same behaviour. From Landau theory, one obtains regions of the phase diagram for which the or-
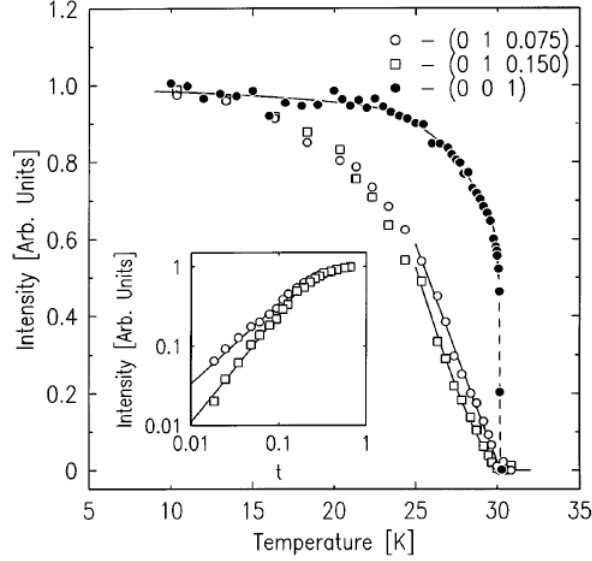
Figure 7.10: *Magnetic intensities obtained at the (001) specular Bragg reflection (solid circles) and along the (01L) magnetic truncation rod at L=0.075 (open circles) and 0.15 (open squares). They have been normalised to 1.0 at low temperatures The solid lines present best fits to a power law dependence on reduced temperature. The solid line for the (001) reflection is a guide for the eye. Inset:Log-Log plot of the magnetic scattering intensity at (0,1,0.075) and (0,1,0.15) vs reduced temperature. Reproduced from [13].*

der parameter at the surface varies continuously, following a power law in reduced temperature, and this appears to occur in Watson's experiments. Watson fits their data to power laws $I = I_0 t^{2\beta}$ where $t = \frac{T_N - T}{T_N}$, the reduced temperature, and the critical exponent is dependent on the reciprocal lattice location L. In particular, the exponents *increase* with increasing distance from the nearest Bragg peak.

Langridge *et al*'s experimental results agree with these findings so far discussed. The order parameter behaviour as a function of temperature is shown in fig. 7.11 which also illustrates a fit to a power law for the continuous transition of the $(0, 1, 0.97)$ intensity. The bulk Bragg peak intensity saturates below $25K$. They do however propose that the continuous transition associated with the ordering of the near-surface region may occur at a temperature *below* the bulk ordering temperature and as such that the system exhibits an extraordinary transition (although this is not certain due to experimental resolution).

The interesting phenomenon however has been discovered in transverse scans
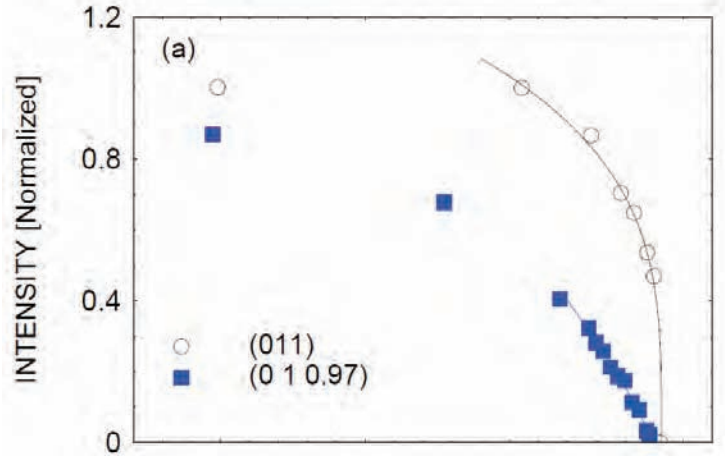
Figure 7.11: *Integrated intensity vs temperature of the bulk (011) magnetic Bragg reflection (open circles) and the surface magnetic rod (0 1 0.97) (filled squares). The continuous transition of the surface magnetic rod has been fitted to a power law $I = I_0 t^{2\beta}$ where t is the reduced temperature. Reproduced from [49]*

taken by Langridge across the magnetic truncation rods (MTRs) at two temperatures $T = 29K$ and $T = 14.8K$. The intensity measurements shown in Fig. 7.12 correspond to measurements of the static spin-spin correlations with respect to the component of the spins that lie in the xy-plane, as was introduced in the previous section. The scans are taken along the bulk Bragg reflection $(0, q_k, 1)$ and purely magnetic truncation rod $(0, q_k, 0.97)$. The lineshape of the bulk shows clear order independent of temperature in the temperature region 29K to 14.8K, in agreement with Watson. Langridge *et al* fit this lineshape to a Lorentzian raised to the power 1.75.

The scan taken along $(0, q_k, 0.97)$ represents the near-surface region and shows a phenomenon not picked up by Watson. For scans performed by Watson at $(0, 1, 0.075)$ and $(0, 1, 0.15)$, the widths of these MTR's appeared to be temperature-independent. As such, the correlations within the near-surface appeared to remain the same as the temperature was lowered and the near-surface became more ordered. Conversely, the experiments by Langridge present a key find. Below T_N the lineshape of the peak obtained from a transverse scan of the MTR instead becomes temperature dependent. The lineshape near q_k can be fitted to a power-law decay
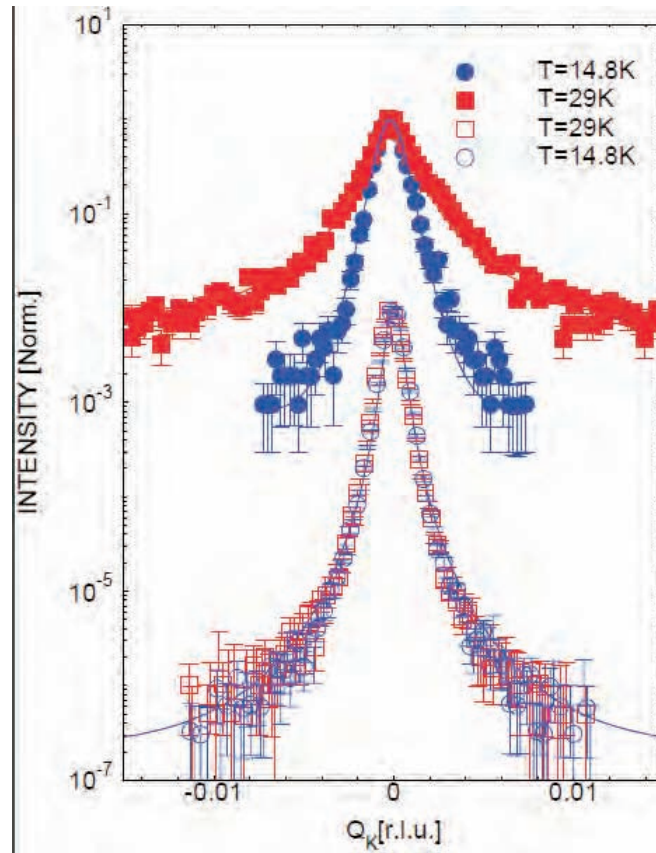
Figure 7.12: *Transverse cuts through the bulk magnetic (011) Bragg reflection (open symbols) and purely magnetic truncation rod $(0q_k0.97)$ (closed symbols) as a function of two temperatures above and below T_N. The bulk magnetic Bragg reflection shows no change in lineshape with temperature and is fitted to a Lorentzian raised to the power 1.75. Conversely, the lineshape of the rod $(0q_k0.97)$ shows a temperature dependence. Reproduced from [49]*

of the form $s(q) \propto q^{\bar{\eta}}$ as in the log-log plot of fig. 7.13 and it is the behaviour of the exponent $\bar{\eta}$ which appears to exhibit a phase transition. The transform from the lineshape in reciprocal space to the real space correlation function $\langle s(r)s(0)\rangle$ is detailed in section 7.2.1 and from this one can determine that the real space correlations develop a power-law-like tail as the temperature is increased past T_{KT}. The power-law nature indicates that the correlations do not extend macroscopically, and furthermore that their length scale decreases with decreasing $\bar{\eta}$.

Fig. 7.14 plots the exponent of the corresponding real space exponent, $\eta = 2 - \bar{\eta}$, as a function of temperature [1] . As the temperature is increased from $T = 0$, the behaviour of the correlations, which have a finite extent, change from a steady, slow decrease in correlation length with temperature, corresponding to a slow disordering parallel to the plane in the near-surface region, to a sudden sharp decrease, corresponding to a sharp onset of disorder in this direction. The subsequent decrease in correlation length, which is linear according to the author's least squares fit to the data, is in fact undertaken at a rate an order of magnitude faster than for temperatures below T_{KT}. It has been proposed that this sudden change in rate of decrease of correlation length may be discontinuous and as such has been assigned as a transition. Interestingly, the temperature of this apparent transition is much below the bulk ordering temperature.

7.3 Uranium Dioxide - Modelling

We study UO_2 at $T = 0$ to get a feel for how the spins reorient as the surface is approached in order to gain a better physical picture and foundation on which to hang possible explanations for the unusual disordering behaviour observed at a temperature below the bulk ordering temperature.

Assuming a type-1 spin configuration in the bulk, we begin by determining how

---

[1]The relationship between the 2D circularly symmetric power law lineshape and that of the real space correlation function is covered in section 7.2.1
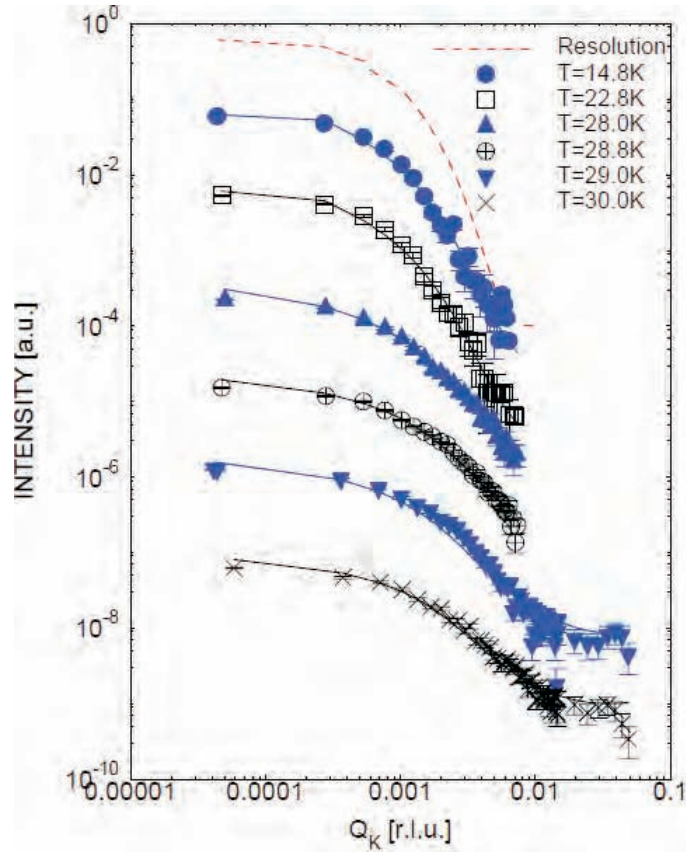
Figure 7.13: *log-log plot of the purely magnetic truncation rod near $q_k = 0$ for temperatures below T_N. The plots have been fitted to a power law of the form $I(q) \sim q^{2\bar{\eta}}$, and the gradient of the plots, corresponding to $-\bar{\eta}$, becomes shallower with increasing temperature. Reproduced from [49]*
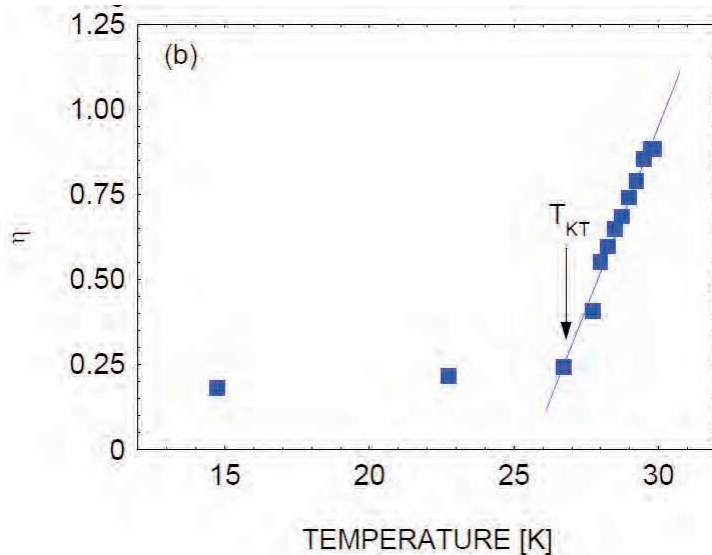
Figure 7.14: *Temperature dependence of the exponent of the real space correlations, $\eta - \bar{\eta}$. At the transition temperature T_{KT}, the exponent is seen to increase sharply and the rate of increase to be an order of magnitude larger than below T_{KT}. The increase is fitted to a linear function. Reproduced from [49]*

we would expect the spins of an FCC lattice to behave under a nearest-neighbour AFM Heisenberg interaction as the surface is approached, in order to simplify our model before solving the thereby reduced form of the Hamiltonian with respect to its degrees of freedom. A Hamiltonian, consisting of both a Heisenberg interaction and an anisotropy energy cost associated with departure from a triple-q structure, is then applied to the simplified model and the ground state determined, which is found to be of a solitonic nature. The magnetism of UO_2 has a transverse orientation with respect to its spins, but we study the simpler longitudinal case here.

7.3.1   Simplifying the Model

We simplify the general state acted on by the Hamiltonian by decreasing the manifold of states available to the system. This is done by considering how the triple-q state in the bulk may want to deform as the surface is approached, assuming there is no variation in the couplings as the surface is approached. We achieve this by performing a Bloch transform parallel to the surface and studying the form of the

179

ground state in terms of the remaining real-space dimension. Due to symmetry considerations assuming identical couplings throughout the system, we focus only on those states of the surface-terminated system that possess a vector component parallel to the surface, $\mathbf{k}_{\parallel}$, that is identical to the bulk, i.e. $\mathbf{k}_{\parallel} = (k_{min}^x, k_{min}^y)$. The effect of the surface is to break the translational symmetry of the lattice and as such we are working with *rods* of spin density located at the $\mathbf{k}_{\parallel}$'s. We can however qualitatively predict the structure of these rods, or in other words the evolution of the spin structure as the surface is approached, by constraining the spin lengths to be identical in real space, as we shall show.

An analysis of the bonds lost at the surface informs us that states with a phase $(\pi, 0)$ in the plane parallel to the surface of a FCC lattice with nearest neighbour only couplings are energetically invariant to the presence of the surface, but states with a $(0, 0)$ phase lose energy. As such, one would expect that, as the surface is approached, the system moves its spin density, originally equally-distributed between the 3 type-1 Bragg spots, from that that corresponds to a $(0, 0)$ phase parallel to the surface to that of $(\pi, 0)$. This is realised in real space as the system reorienting its spins from a 3-q towards a 2-q state as the surface is approached.

7.3.2   Heisenberg Hamiltonian for FCC Lattice with a Surface

Performing a Bloch Transform Parallel to the Surface

For convention, we align the surface to be perpendicular to the z-direction. The FCC lattice can be broken down into 2 distinct layers parallel to the surface which alternate. The layers are labelled by n_z and $n_{z'}$ and the positions of the spins within the layers are labelled by j_{n_z} and $j_{n_{z'}}$. The Bloch transform parallel to the surface is hence notated as:

$$\mathbf{S}_{j_{n_z} n_z} = \frac{1}{\sqrt{N}} \sum_{\tilde{\mathbf{k}}} e^{i\tilde{\mathbf{k}}.\mathbf{R}_{j_{n_z}}} \mathbf{S}_{\tilde{\mathbf{k}} n_z} \qquad (7.3.1)$$

and the inverse Bloch transform as

$$\mathbf{S}_{\tilde{\mathbf{k}} n_z} = \frac{1}{\sqrt{N}} \sum_{j_{n_z}} e^{-i\tilde{\mathbf{k}}.\mathbf{R}_{j_{n_z}}} \mathbf{S}_{j_{n_z} n_z}, \qquad (7.3.2)$$

where N is the number of atoms within the plane n_z (or $n_{z'}$), $\tilde{\mathbf{k}}$ is (k_x, k_y) and $\mathbf{R}_{j_{n_z}}$ is the position vector of the spin at the j_{n_z} position.

The Heisenberg of the system can be written as

$$H = \frac{J}{2} \sum_{<j_{n_z} n_z, j'_{n'_z} n'_z>} \mathbf{S}_{j_{n_z} n_z}.\mathbf{S}_{j'_{n'_z} n'_z}, \qquad (7.3.3)$$

where the notation $< j_{n_z} n_z, j'_{n'_z} n'_z >$ indicates that the sum must be calculated such that for each point $j_{n_z} n_z$, sum over all its nearest neighbours $j'_{n'_z} n'_z \neq j_{n_z} n_z$ then sum over all $j_{n_z} n_z$ points.

The Bloch transform is applied to the system. Additionally, a new 'convention' for performing the sum over all interactions is adopted which simplifies the problem as a result of the system not extending to infinity in both directions. This convention is described as performing a sum over planes n_z where each term in the sum over planes includes the energy associated with interactions within the plane n_z and with the plane below (towards the bulk). As such, all interactions are accounted for and the resulting expression is

$$H = \quad J\sum_{n_z}\sum_{\tilde{\mathbf{k}},\tilde{\mathbf{k}'}}\left[\left(\frac{1}{2N}\right)\mathbf{S}_{\tilde{\mathbf{k}}n_z}.\mathbf{S}_{\tilde{\mathbf{k}'}n_z}\sum_{<j_{n_z}n_z,j'_{n_z}n_z>}e^{(i\tilde{\mathbf{k}}.\mathbf{R}_{j_{n_z}}+i\tilde{\mathbf{k}'}.\mathbf{R}_{j'_{n_z}})}\right.$$
$$\left.+\left(\frac{1}{N}\right)\mathbf{S}_{\tilde{\mathbf{k}}n_z}.\mathbf{S}_{\tilde{\mathbf{k}'}(n_z+1)}\sum_{<j_{n_z}n_z,j'_{(n_z+1)}(n_z+1)>}e^{i\tilde{\mathbf{k}}.\mathbf{R}_{j_{n_z}}+i\tilde{\mathbf{k}'}.\mathbf{R}_{j'_{(n_z+1)}}}\right], \qquad (7.3.4)$$

where double-counting need only be taken care of in the sum over nearest neighbours within the plane, hence the factor of a half is present in the first term of the summation over n_z. Next we consider that the 2 terms in the summation over the planes n_z can be written in terms of structure factors so our expression simplifies to

$$H \quad = \quad \sum_{n_z}\sum_{\tilde{\mathbf{k}}}\left[\left(\frac{1}{2}\right)\mathbf{S}_{\tilde{\mathbf{k}}n_z}.\mathbf{S}_{-\tilde{\mathbf{k}}n_z}J\sum_{\mathbf{R}_m}e^{i\tilde{\mathbf{k}}.\mathbf{R}_m}\right.$$
$$\left.+\mathbf{S}_{\tilde{\mathbf{k}}n_z}.\mathbf{S}_{-\tilde{\mathbf{k}}(n_z+1)}J\sum_{\mathbf{R}_p}e^{i\tilde{\mathbf{k}}.\mathbf{R}_p}\right], \qquad (7.3.5)$$

where $\mathbf{R}_m$ are the vectors $\mathbf{R}_{j_{n_z}} - \mathbf{R}_{j'n_z}$ and constitute the vectors joining 2nd nearest-neighbour points on a 2D square lattice, and $\mathbf{R}_p$ are the vectors $\mathbf{R}_{j_{n_z}} - \mathbf{R}_{j'(n_z+1)}$ which correspond to the vectors joining nearest neighbour points again on a 2D square lattice. The structure factors corresponding to the 2 summation terms over the vectors $\mathbf{R}_m$ and $\mathbf{R}_p$ were calculated in section 3.2.3 as 3.2.21 and so our expression becomes

$$H \quad = \quad \sum_{n_z}\sum_{\tilde{\mathbf{k}}}\left[(2J\cos k_x\cos k_y)\mathbf{S}_{\tilde{\mathbf{k}}n_z}.\mathbf{S}_{-\tilde{\mathbf{k}}n_z}\right.$$
$$\left.+2J(\cos k_x+\cos k_y)\mathbf{S}_{\tilde{\mathbf{k}}n_z}.\mathbf{S}_{-\tilde{\mathbf{k}}(n_z+1)}\right]. \qquad (7.3.6)$$

7.3.3 Determining Eigenstates for the Ground State Configuration

Now that we have an expression for H_{k_x,k_y,n_z}, we limit the manifold of states accessible to the system, as described above, by substituting the $\mathbf{k}_\parallel$'s present in the bulk and obtain the Hamiltonian as a function of only one variable, n_z. The turning points of the energy correspond to the eigenstates of this Hamiltonian, as proved in 2.6, which includes our ground state. In the current basis the eigenstates we determine are of the form $\left(\mathbf{s}_{(k_x,k_y)}\right)_{n_z}$, where we label the element of this vector by plane number n_z. In order to allow for the determination of the eigenstates, we terminate the system also at $n_z = N$ such that the matrix becomes of finite size tridiagonal.

Substituting the rods $(k^x_{min}, k^y_{min}) = (\pi, 0)$ and $(k^x_{min}, k^y_{min}) = (\pi, 0)$ results in a diagonal matrix for H_{k_x,k_y,n_z} and as such any vector $\left(\mathbf{s}_{(k_x,k_y)}\right)_{n_z}$ is an eigenstate with eigenvalue $2J$. As such, the order with planes parallel to the surface is fixed, *but* we therefore have complete freedom with respect to the magnitude and direction of the spin density associated with the different planes parallel to the surface. In other words, we have 'independent' xy planes with respect to the spin interaction. This is due to the FCC lattice geometry; in this geometry, if a plane consists of Néel order, then adjacent planes are independent from each other in the nearest-neighbour Heisenberg model due to a cancelling of the plane-to-plane coupling. As a result, this state, whereby the planes parallel to the surface are Néel order in character, is passive to the surface.

Substituting the rod $(k^x_{min}, k^y_{min}) = (0, 0)$ however results in a tridiagonal matrix which couples the n_z planes and fixes the eigenstates. To solve for the eigenstates, we first determine the eigenstates of the problem concerning a system with infinite extent in the z-direction. Ring boundary conditions are used in order to solve for the eigenstates, with the result that states defined by $(\mathbf{s}_{0,0})_{n_z} = z^{n_z}\hat{\mathbf{s}}_{0,0}$ and $(\mathbf{s}_{0,0})_{n_z} = z^{-n_z}\hat{\mathbf{s}}_{0,0}$ are both eigenstates. We shall use these to construct a solution

to the finite system.

Surfaces are then introduced to the system by terminating the basis at $n_z = 1$ and $n_z = N$. The elements of the eigenstates can thus be found by solving the set of simultaneous equations

$$\beta \left(\mathbf{s}_{0,0}\right)_{n_z-1} + \alpha \left(\mathbf{s}_{0,0}\right)_{n_z} + \beta \left(\mathbf{s}_{0,0}\right)_{n_z+1} = \lambda \left(\mathbf{s}_{0,0}\right)_{n_z} \tag{7.3.7}$$

for all n_z subject to the boundary conditions $\left(\mathbf{s}_{0,0}\right)_{N+1} = 0$ and $\left(\mathbf{s}_{0,0}\right)_0 = 0$, where λ is the eigenvalue, $\alpha = 2J \cos k_x \cos k_y = 2J$ and $\beta = J(\cos k_x + \cos k_y) = 2J$.

Eigenstates to satisfy this expression can be constructed from those of the infinite problem and are defined by $\left(\mathbf{s}_{0,0}\right)_{n_z} = \left(z^{n_z} - z^{-n_z}\right).\hat{\mathbf{s}}_{(0,0)}$ where z is a $(2N + 2)$'th root of unity, to satisfy the second boundary condition. The eigenvalue λ is thus given by the expression

$$\lambda = 2J \left[1 + \left(z + \frac{1}{z}\right)\right]. \tag{7.3.8}$$

The minimum value that gives a non-trivial eigenstate corresponds to $z = e^{\frac{i\pi N}{N+1}}$, thereby defining the minimum energy eigenstate as

$$\left(\mathbf{s}_{0,0}\right)_{n_z} = 2i \sin\left(\frac{2\pi N}{N + 1}n_z\right).\hat{\mathbf{s}}_{0,0}, \tag{7.3.9}$$

with eigenvalue

$$\lambda = 1 + 2 \cos\left(\frac{n\pi}{N + 1}\right). \tag{7.3.10}$$

As such, the spin space vectors in each plane oscillate in the direction perpendicular to the surface by a π phase, resulting in a final state consisting of ferromagnetic planes orientated parallel to the surface with an antiferromagnetic configuration in the direction perpendicular to the surface. Furthermore, the direction of this vector is forced to lie along the same direction, $\hat{\mathbf{s}}_{0,0}$, plane to plane, unlike those of the $(\mathbf{s}_{\pi,0})_{n_z}$ eigenstate with its independent independant planes. [2]

Since $(\mathbf{s}_{0,0})_{n_z}$ varies its magnitude from plane-to-plane, it cannot satisfy the length constraint on its own and we must therefore construct the real space spin by using a superimposition of both eigenstates. We hence continue our study of the eigenstates in order to determine how to construct the combination as the surface is approached by focussing on how exactly the surface affects these eigenstates.

$(\mathbf{s}_{0,0})_{n_z}$ decreases its magnitude as the surface is approached, since this state 'hates' the surface. In contrast, ignoring the length constraint, $(\mathbf{s}_{\pi,0})_{n_z}$ has the freedom to choose the magnitude of each element. As such, the system can maintain the spin length of all spins by compensating for the decreasing spin contribution of eigenstate $(\mathbf{s}_{0,0})_{n_z}$ with $(\mathbf{s}_{\pi,0})_{n_z}$, superimposing them contributions orthogonally. This construction in real space is described by

$$\mathbf{s}_{n_x,n_y,n_z} = e^{i\pi n_x} (\mathbf{s}_{\pi,0})_{n_z} + (\mathbf{s}_{0,0})_{n_z}, \qquad (7.3.11)$$

where the vector $(\mathbf{s}_{\pi,0})_{n_z}$ lies in a plane perpendicular to the vector $(\mathbf{s}_{0,0})_{n_z}$ which remains fixed in direction with n_z,

We therefore arrive at a simpler problem to solve - the manifold of states available to the system can be decreased according to this construction, and the problem then reduces to determination of the ratio involved in the superimposition as a function

---

[2]It is also worth noting that that magnitude of the vector $\mathbf{s}_{k_\parallel}$ is very small according to the eigenstate. This is a consequence of the Bloch transform consisting not of one or two $\mathbf{k}$ points but many, a consequence of the system being truncated which produces rods of spin density in reciprocal space.
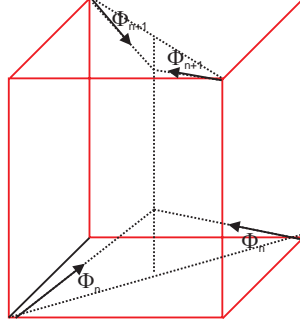
Figure 7.15: *Spin states available to our UO$_2$ model. The surface, directed perpendicular to the z-axis, is located at n = 1*

of plane n_z. The simplified manifold of states is illustrated in fig. 7.15 whereby there is solely one variable, ϕ, which we expect to soften as the surface is approached. The resulting components of each spin are shown explicitly in the figure.

Note that this ϕ-model reflects the different MSDW phases involved in the spin-density-wave phase transitions of γ-Mn that was studied in section 4.3.

7.3.4   Solving the Model

We introduce a single-ion anisotropy term which is applied to cubic crystals in order to break the spin space degeneracy inherent in the Heisenberg model and reflect the preference of spin direction which we know to be triple-q in the bulk. The Hamiltonian now takes the modified form

$$H = \frac{J}{2} \sum_{<jj'>} \mathbf{S}_j \mathbf{S}_{j'} + \kappa \sum_j \left([s_j^x]^4 + [s_j^y]^4 + [s_j^z]^4 \right). \qquad (7.3.12)$$

The term serves to stabilise both single-1 and triple-q states, which can be seen by applying a lagrange-multiplier, λ, to the minimisation, such that the anisotropy term is minimised subject to the length constraint. Analysing the energies of the turning-point solutions to the equation that involves a lagrange multiplier λ:

$$f(s_j^x, s_j^y, s_j^z) = \left([s_j^x]^4 + [s_j^y]^4 + [s_j^z]^4\right) - \lambda \left([s_j^x]^2 + [s_j^y]^2 + [s_j^z]^2 - S^2\right), \quad (7.3.13)$$

one finds that the minimum solution corresponds to the spins pointing along the cubic diagonals, but with the freedom to point towards or away from the centre of the cube. The manifold of minimum solutions thus corresponds to $(s_j^x, s_j^y, s_j^z) = 1/\sqrt{3}(1, 1, 1)$ and all combinations achieved by independently changing the signs of each component. These states are a subset of the manifold described by our simplified ϕ state of figure 7.15 that is a solution to the Heisenberg model with a surface included and as such does indeed merely break the degeneracy rather than renormalise the states.

Although the inclusion of this anisotropy results in the double-q state no longer being a ground state of the system, both the 1-q and 3-q states accommodate this anisotropy. This degeneracy, which prevents good agreement of the model with the experimentally-observed spin wave dispersion, shall be discussed later on and improvements made to the model. For now though, we assume this simple model and solve for the ground state solution in the presence of the surface.

In acting the Heisenberg term, H_1, on our general state, the calculation is split into a sum over planes that are labelled n, and a sum over the sites within each plane, which are labelled by i, taking care to include double-counting for interactions within planes only:

$$
\begin{aligned}
H_1 \;=\; & J \sum_{n=1}^{\infty} \sum_i \Bigg[\;\; 2S\left(\frac{c_n}{\sqrt{2}}, \frac{c_n}{\sqrt{2}}, s_n\right).S\left(\frac{-c_n}{\sqrt{2}}, \frac{-c_n}{\sqrt{2}}, s_n\right) \\
& + 2S\left(\frac{c_n}{\sqrt{2}}, \frac{c_n}{\sqrt{2}}, s_n\right).S\left(\frac{c_{n+1}}{\sqrt{2}}, -\frac{c_{n+1}}{\sqrt{2}}, -s_{n+1}\right) \\
& + 2S\left(\frac{c_n}{\sqrt{2}}, \frac{c_n}{\sqrt{2}}, s_n\right).S\left(-\frac{c_{n+1}}{\sqrt{2}}, \frac{c_{n+1}}{\sqrt{2}}, -s_{n+1}\right) \Bigg], (7.3.14)
\end{aligned}
$$

where c_n and s_n refer to $\cos\phi_n$ and $\sin\phi_n$ respectively. Converting the cosines into sines and given that the number of spins within a plane is N, we arrive at

$$H_1 = 2JS^2N \sum_{n=1}^{\infty} \left(2s_n^2 - 1 - 2s_n s_{n+1}\right). \tag{7.3.15}$$

The second term in the Hamiltonian, H_2 is given by

$$H_2 = \kappa N \sum_{n=1}^{\infty} \left[\left(\frac{Sc_n}{\sqrt{2}}\right)^4 + \left(\frac{Sc_n}{\sqrt{2}}\right)^4 + (Ss_n)^4 \right]. \tag{7.3.16}$$

Completing the square puts H_2 into the form

$$H_2 = \kappa N S^4 \sum_{n=1}^{\infty} \left[\frac{1}{6}(3s_n^2 - 1)^2 + \frac{1}{3} \right]. \tag{7.3.17}$$

The full Hamiltonian $H = H_1 + H_2$ can be written in terms of a parameterisation $\beta^2 = \frac{\kappa S^2}{4J}$, describing the relative strengths of the interaction constant and the cubic anisotropy of the system:

$$H = 2JS^2N \left[s_1^2 + \sum_{n=1}^{\infty} \left[(s_n - s_{n+1})^2 - 1 + \frac{\beta^2}{3} \left((3s_n^2 - 1)^2 + 2\right) \right] \right]. \tag{7.3.18}$$

Since the summation is over an infinite number of planes, our expression diverges. However, we are interested in the spin state that corresponds to the ground state close to the surface, and so we may use the bulk state energy as a reference energy, H_0, and minimise the convergent expression $H - H_0$.

We constrain the spins to point along the cubic diagonals in the bulk by applying the bulk boundary condition $s_\infty = \frac{1}{\sqrt{3}}$. As such, we can write the Hamiltonian as

$$H = 4JS^2NE + H_0, \tag{7.3.19}$$

where

$$E = \frac{1}{2}\left[s_1^2 + \sum_{n=1}^{\infty}\left[(s_n - s_{n+1})^2 + \frac{\beta^2}{3}(3s_n^2 - 1)^2\right]\right] - \frac{1}{6}. \tag{7.3.20}$$

To determine the spin state that corresponds to the ground state configuration for the spins near the surface, we only need to minimise E which corresponds to differentiating the expression

$$\left(s_n - s_{n+1}\right)^2 + \frac{\beta^2}{3}(3s_n^2 - 1)^2, \tag{7.3.21}$$

with respect to s_n for all n. Equation 7.3.21 involves s_n and s_{n+1}, so we must take care to include all relevant terms during the minimisation procedure. We obtain

$$s_{n+1} + s_{n-1} = 2s_n + 2\beta^2[3s_n^2 - 1]s_n \qquad \text{if } n \neq 1, \tag{7.3.22}$$

$$s_{n+1} = 2s_n + 2\beta^2[3s_n^2 - 1]s_n \qquad \text{if } n = 1. \tag{7.3.23}$$

We can express eq.7.3.23 as eq.7.3.22 by incorporating a surface boundary condition $s_0 = 0$, and hence can define the minimisation condition as

$$s_{n+1} + s_{n-1} = 2s_n + 2\beta^2[3s_n^2 - 1]s_n \qquad \text{for } n \subset [0, \infty]. \tag{7.3.24}$$

The continuum limit to our problem can also be considered, since in the limit

189

$\beta \rightarrow 0$, n becomes a continuous variable (since $\frac{ds_n}{dn} \rightarrow 0$). In this case, we find that the minimisation problem reduces down to a standard soliton problem. Given eq. 7.3.20 we define the lagrangian, L, as

$$L = L(s_n', s_n; n) = (s_n')^2 + \frac{\beta^3}{3}(3s_n^2 - 1)^2 \tag{7.3.25}$$

and applying the Euler-Lagrange equation. We obtain

$$\left(\frac{ds_n}{dn}\right)^2 = \frac{\beta^2}{3}(3s^2 - 1)^2 + C \tag{7.3.26}$$

where C is defined by boundary conditions. Given that $s_n' \rightarrow 0$ as $n \rightarrow \infty$, or equivalently as $s_n \rightarrow \frac{1}{\sqrt{3}}$, we arrive at the ordinary differential equation

$$\frac{ds_n}{dn} = \frac{\beta}{\sqrt{3}}(3s^2 - 1) \tag{7.3.27}$$

and hence the solution

$$s_n = \frac{1}{\sqrt{3}} \tanh \beta n. \tag{7.3.28}$$

Calculation of the continuum limit value of E yields

$$E = \frac{2\beta}{9} - \frac{1}{6}. \tag{7.3.29}$$

Eq. 7.3.24 is solved numerically using a recursion method with boundary condition $s_\infty \rightarrow \frac{1}{\sqrt{3}}$. Specifically, the s_n are set to the bulk value $\frac{1}{\sqrt{3}}$ initially, except for s_0 which takes its boundary condition value of zero. Iterations are then performed based on a rearrangement of eq.7.3.24:

$$s_n^{(new)} = F.\frac{s_{n+1}^{(old)} + s_{n-1}^{(old)}}{2 + 2\beta^2 \left[3 \left(s_n^{(old)}\right)^2 - 1\right]}, \qquad (7.3.30)$$

where F is a percentage and solves convergence problems. The results for $\beta = 0.1$ and $\beta = 0.8$ for a system with 100 planes are shown in figure 7.16. We can see that the system smoothly transforms from the bulk state towards a double-q state on the surface (although the system only becomes double-q on the virtual plane neighbouring the surface layer). The rotation of spins occurs over a very small length scale of only a few planes when the anisotropy term has a similar strength to the interaction term.

7.3.5   Solitonic Solution

The ground state of the triple-q structure can be thought of as alternating sublattices in the direction perpendicular to the bulk, due to the π phase of the state in this direction. As a result, there exists a two-fold degeneracy in the ground state that are related by a translation by one layer in this direction. The surface can be thought of as a defect that upsets this alternating configuration in such a way that one can think of extending our spin configuration past the surface, whereby the triple-q ground state turns into the other degenerate triple-q ground state. This configuration is a result of the two boundary conditions of the problem, being the surface termination and the triple-q structure taken in the bulk. The surface termination forces a topological soliton to form, in the same way described in [54] which is concerned with soliton formation in polyacetylene. The bond-alternation of polyacetylene, in terms of *pi* and *sigma* bonds, is anologous to the alternation of the spin configuration in the direction perpendicular to our surface, and results in a topological soliton. The soliton comes about as a localised excitation in the polyacetylene in accordance with imposed boundary conditions of having one of the

two degenerate phases, A, at one end of the system, and the other, B, at the other end.

Specifically, consider the system initially being in one of the degenerate states, which we shall call the A phase. In order to create a soliton, the B phase must be, for example, the left-hand portion of the chain. We want to treat the soliton as a *localised* excitation, which it is not if the two ends terminate at different phases. Su *et al* deal with this construction by considering creation of an additional antisoliton, such that the configuration goes from phase A to B and back to A along the chain. If the soliton and antisoliton are widely separated then they do not interact and one can neglect this construction and the energy to create the configuration is solely the addition of the energy required to create the antisoliton plus the soliton. They find that in a perfect lattice there is relatively free translation of the soliton down to temperatures of $20 - 40K$.

Solitons by definition cannot be created or destroyed by perturbative effects, and hence are very stable - in order to destroy a soliton, one would need to 'move' it all the way to the edge of the system, which in our case is into the bulk. This is not allowed due to the large energy cost of having a double-q state in the bulk which cannot be compensated for by the energy gain at the surface layer (unless appropriate surface roughness exists).

7.3.6 Improved Model

The model 7.3.12 used in the calculations so far does not in fact break enough degeneracies to give reasonable solutions. This is due to the degeneracy between single-q and triple-q states, which is not broken by the anisotropy term present - the term serves solely to stabilise the spin vectors to point along cubic diagonals. According to the spin wave dispersion calculated for this model by Long [14], there is a softening of the spin waves in the Cartesian directions that are not present in the experimental spinwave dispersions. This softening corresponds to the lines of
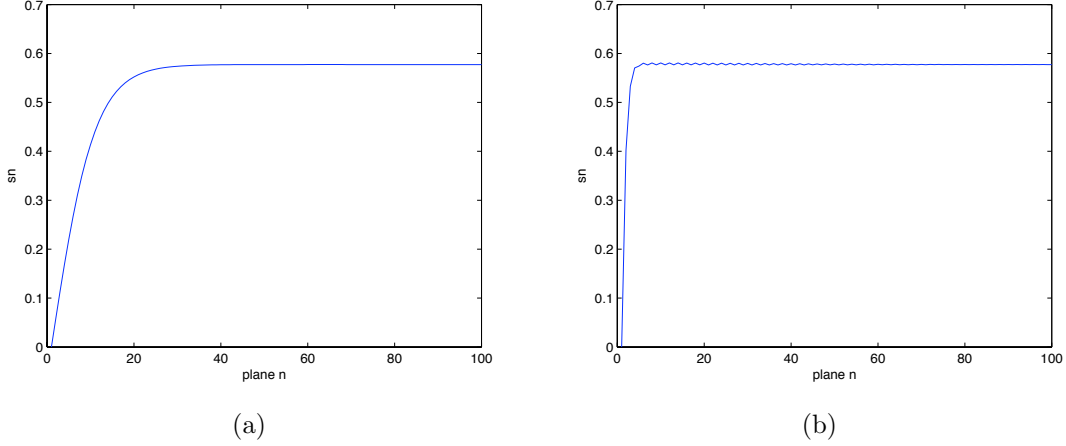
Figure 7.16: *Numerically-generated plot of s_n against plane n for (a)$\beta = 0.1$ and (b)$\beta = 0.8$. 1000 iterations performed for a system with 100 planes n and F set to 0.01*

degeneracy present in a Heisenberg model with respect to the $\mathbf{k}_{min}$ as we covered in section 3.2.4. This 1q-3q degeneracy present in the model results in the minimum energy configuration of the system in fact being sheets aligned perpendicular to the surface of Néel character. In this way, the surface can be completely compensated for since the sheets are not coupled and so there is no energy cost in introducing a surface to the system. In addition, one may align the spins within these néel sheets to the (111) direction and therefore pay no anisotropy energy according to the present model.

As such, extra anisotropy terms are required, to stabilise the triple-q structure and also the longitudinal structure we have assumed in our investigation. We know from our previous studies of chapter 4 that quantum fluctuations stabilise collinear states and so strong anistropies are required to overcome this factor. Impurities, entering the system local disorder, stabilise multiple-q states, but UO_2 is inherently clean/very pure as a material, and so the phenomenon stabilising triple-q in the bulk must be something else.

As such, Long [14] introduces two terms to the Hamiltonian. The term

$$\frac{H}{4} \sum_{<jj'>} (\mathbf{s}_j . \mathbf{s}_{j'})^2 \tag{7.3.31}$$

stabilises the 3q state over the 1q state by promoting perpendicular bonds and penalising parallel bonds. The term is isotropic in spin space, and so an additional term

$$\frac{J}{2} \sum_{\alpha} \sum_{<jj'>_{\alpha}} (\delta - 1) s_j^{\alpha} s_{j'}^{\alpha}, \tag{7.3.32}$$

where $\sum_{<jj'>_{\alpha}}$ denotes nearest neighbour bonds oriented in a direction *perpendicular* to the Cartesian α-axis, is used to modify the Hamiltonian to prefer longitudinal rather than transverse spin orientations by reducing the strength of the frustrated, parallel components by a factor δ.

7.3.7 Results and Conclusion

The calculations performed in this chapter indicate that a solitonic domain wall exists between a 2q state on the surface and 3q state in the bulk. The MSDW behavior with depth is similar to the behaviour seen in the spin-reorientation transition of $Mn_{85}Ni_9C_6$ detailed in section 4.3 and illustrated in fig. 4.15 For the $Mn_{85}Ni_9C_6$, as the temperature is decreased past the bulk ordering temperature, the system takes on the triple-q structure with all three Bragg spots possessing equal spin density amounts. As the temperature reaches T_{MS} the system is ordered enough for the energetics near the impurities to play a part and the system to prefer to orient the spins into a 2q configuration in the vicinity which becomes long range correlations if the concentration of impurity is past a critical value. Thus as the temperature passes through T_{MS} the spin density originally located at the third Bragg spot becomes

194

redistributed to the other two Bragg spots and increases in intensity as the system orders further. The depth profile of ground state of uranium dioxide can be considered in a similar fashion. The truncation of the system by the surface results in the loss of Bragg spots, but if one considers the truncation rods in the limit of small attenuation so that one could envisage measuring the depth profile as large enough 'chunks' of depth to give an approximately coherent scattering, then a spot can be associated with different depths. In this way, the 'spots' as a function of depth follow a similar behaviour as those for $Mn_{85}Ni_9C_6$ as a function of temperature.

Long [14] has applied classical fluctuation theory to the solitonic ground state configuration at $T = 0$. The lowest energy excitation constrained to be uniform within the planes perpendicular to the surface has a structure which, when superimposed onto the ground state profile, corresponds to a profile in which the domain wall has shifted more towards the bulk. The distortion as a function of depth is shown in Fig.7.17. This mode is bound to the surface and on the same length scale as the soliton. The distortion suggests the possibility of the domain wall moving further into the bulk, since thermal excitations of this mode, which lie within the bulk spinwave gap, would amount to distortions of this type as thermal fluctuations from the ground state. Since the surface creates a boundary and the profile is not symmetric, these fluctuations would be biased towards the direction of the bulk. This corresponds to a movement of the average location of the wall towards the bulk and an increase in temperature would correspond to the excitement of more of these modes, creating larger fluctuations and therefore the movement of the wall towards the bulk on the increase of temperature.

A similar picture can also be gained through comparison of the behaviour of the spinwave gap observed by Cowley and Dolling to the theoretically produced spinwave spectrum for our model as detailed in [14]. The theoretical analysis indicates that the low energy spinwave gap to double-q fluctuations is equal to $4JS\alpha$, where $\alpha = \frac{3KS^2}{J}\sin^2\phi\cos^2\phi = 12\beta^2\sin^2\phi\cos^2\phi$. It has been shown experimentally that this

gap, corresponding to (001), softens as temperature is increased, as shown in figure 7.5 [8]. It therefore seems appropriate to consider the parameter $4JS\alpha$ decreasing with increasing temperature. Renormalisation can then be applied in an attempt to introduce temperature into the theory and this is done in [14]. The following idea based on preliminary analysis has not been analysed in detail, but gives a reasonable picture of how the domain wall may behave as the temperature is increased. β can be thought of as a measure of how far the domain wall moves into the bulk, as can be see in fig. 7.16. One can express β^2 in terms of the spin wave gap $G = 4JS\alpha$ which is known to decrease with temperature:

$$\beta^2 \sim G\left(\frac{1}{Jf(\phi)}\right) \tag{7.3.33}$$

where $f(\phi)$ is the ϕ dependence of α. As such, one may expect, since J does not alter much with temperature, the domain wall to drop into the bulk as the temperature is increased and G decreases.

Although it is possible that a picture of the behaviour of the magnetisation profile could be obtained by analysis of the scattering intensity distribution along the truncation rods in a direction perpendicular to the surface, it is particularly tricky to calculate. The correlations as a function of depth can be obtained from the size of the magnetic moment as a function of depth and can provide a length scale which, if altering with temperature, would indicate that our domain wall is fluctuating as a function of depth. The intensity, relating to the size of the magnetic moment, measured at a particular location on the truncation rod, can be associated with a particular depth, as per the analysis of Watson et al [13]. However, to obtain said profile of the magnetic moment length, the surface termination, probe attenuation with depth etc. all need to be taken into account and this can prove tricky. Instead, we look to the explicit information indicated by Langridge *et al*'s experiment, being the correlations *parallel* rather than perpendicular to the surface,

which are in fact tied to those in the perpendicular direction.

Further analysis is hence performed by Long *et al* whereby the fluctuation on each lattice site is allowed to vary independently within planes as well as from plane-to-plane. The result is a band of excitations that control the disordering parallel to the surface and this again sits inside the spinwave gap to bulk excitations. Thus, the movement of the domain wall into the bulk is indeed associated with a disordering of spins in a direction parallel to the surface moving further into the bulk, and this is what may be being observed in Langridge *et al*'s experiments.

The disordering of the surface and in particular the system behind the wall at a lower temperature than the bulk is intuitively sound, as is seen in the measurements of Fig.7.10. The theoretical determination of the low energy spinwave gap indicates that the gap is smaller for smaller ϕ angles [14]. This is as expected since as ϕ is decreased the spins reside more towards the xy plane and so there is stronger coupling in the xy plane. Thus, more energy is required to access fluctuations within the xy plane than those associated with an added phase in the z-direction, perpendicular to the surface, since in this direction the Heisenberg coupling has decreased at the expense of the in-plane coupling. This leads to hardening of the spin waves within the planes and softening in the perpendicular direction to the surface, so that fluctuations that lead to double-q excitations become more energetically accessible near the surface. Thus, one would indeed expect the surface to disorder at a lower temperature than the bulk.

Wetting or Not?

We look to wetting as an explanation due to it explaining the presence of a transition associated with the surface that occurs *below* the bulk ordering temperature. The only other magnetic surface transition that can occur below the bulk ordering temperature of which the author is aware is via the phenomenon of magnetic surface reconstruction that has been formulated within this thesis. However, this theory can
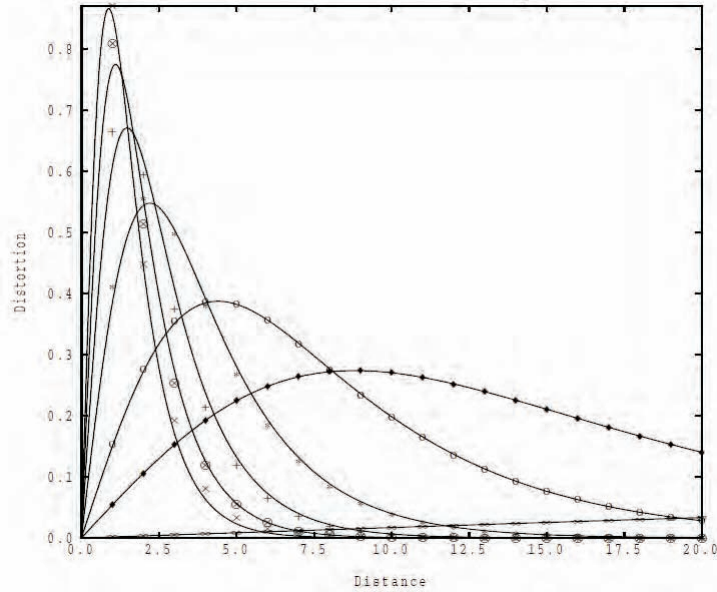
Figure 7.17: *Shape of lowest energy distortion (mode), which appears close to the surface, based on a fluctuation calculation modelling fluctuations $\delta\phi_n$ that are allowed to vary plane-to-plane. The symbols represent the exact solution and the curve the continuum solution as computed using impurity theory by Long in [14]. The distance axis measures the number of planes from the surface layer and the distortion is the sinusoid of the distortion $\delta\phi_n$ from the ground state angle (see calculation in [14].*

be disregarded since the phenomenon requires the surface to have access to a new, independent magnetic order not taken by the bulk which then has its own transition. The bulk of uranium dioxide is triple-q and as such all magnetic orders are taken by the bulk, leaving no scope for a new order and hence magnetic reconstruction on the surface.

On approaching the surface from the bulk, the magnetisation profile related to the third spot increases as the system reorients from a 2-q to a 3-q state as a function of depth. Wetting-type transitions are concerned with the behaviour of the magnetisation profile as a function of temperature, and one can consider there to be three cases as the temperature is increased: (1) The order parameter decreases uniformally with respect to depth, such that there is no change in shape of the magnetisation profile (2) there is a change in the shape of the magnetisation profile, corresponding to the interface location moving, but continuously and (3) there is a *discontinous* change of shape of the magnetisation profile, corresponding

to the interface suddenly moving into the bulk, either divergent or to another finite but larger value. The theoretical analysis points towards the shape of the profile altering with temperature as thermal fluctuations cause the domain wall interface to effectively move towards the bulk, but whether or not this movement can be considered wetting-like is another matter.

Wetting transitions and the associated surface-induced disorder transition was covered in chapter 5 and we refer to this literature. The order parameter associated with wetting transitions is concerned with the depinning of the domain wall, and measures the fluctuations of the interface length as defined in section 5.2. The wetting case occurs for the limiting case of $h_1 \rightarrow 0$ where the bulk and surface states become degenerate. For the SID transition, the wetting-type analogue again concerns the bulk and surface free energies becoming degenerate as the temperature is increased and both states completely disorder. In both these cases there is therefore scope for the bulk to take up the surface state once certain parameters are reached and for the domain wall to become delocalised, possessing fluctuations up to and including macroscopic length scales.

For the 2q-3q interface however, wetting does not seem a fitting theory. The free energies of the 2q and 3q states are *not* degenerate in uranium dioxide on the increase of temperature, and so whilst the domain wall may move into the bulk via thermal fluctuations of the spins, the interface length is not able to diverge into the bulk as per complete wetting and critical wetting. There remains the possibility of a pre-wetting transition occurring, in which the interface width jumps discontinuously but to a finite value as per a first order transition.

Although there is hesitation in using wetting-type transitions to explain the sudden, sharp disordering in the near-surface region at a temperature lower than the bulk ordering temperature, it is possible that an interface-delocalisation SID transition could explain the unusual onset of a *continuous* disordering of the surface in the presence of a bulk that remains ordered up to a first order transition. $CuAu_3$

shows this behaviour, and Lipowsky [44] analyses the behaviour in terms of a magnetisation profile between the surface and bulk, present due to the reduced coupling at the surface in comparison with the bulk. The magnetisation at the surface, M_1, can go continuously to zero in the presence of a bulk that shows no disordering until the ordering temperature T_N is reached for a variety of values of surface coupling. If the profile possesses a point of inflection, an interface width can be assigned to the inflection point and the idea is that movement of this interface width, which occurs as the surface disorders further with temperature, results in M_1 decreasing continuously. The presence of this interface prevents the large field present from the ordered bulk from affecting the surface layer magnetisation, allowing a continuous disordering transition to occur there. The phenomenon has been compared to wetting via analysis of Landau models.

However, the continuous disordering of the surface is perhaps not surprising, since the bulk transition is slow but continuous up to a very small deviation from the bulk ordering temperature 7.1. The surface can therefore follow the bulk's second-order disordering character up to very close to the bulk ordering temperature, but with a much more pronounced disordering due to the loss of magnetic bonding at the surface. The surface may in fact then follow the first order behaviour of the bulk ordering transition in the small temperature range below it, but it may be discernible from a continuous transition due to experimental resolution.

There are two domain walls that need to be considered in the theory; this order-disorder-type wall, and the 2q-3q domain wall. The sharp disordering seen in the surface layer is at a temperature much below that of the bulk ordering temperature. It therefore seems reasonable to assume that the disordering is concerned with the domain wall between the 2q and 3q states, rather than the other order-disorder wall as the surface order parameter has almost approached saturation at the sharp disordering transition. As such, we can expect the sharp disordering to occur in a system that is reasonably near to being fully ordered, which is our solitonic state

perturbed with thermal fluctuations. There exists a picture in which, on lowering the temperature past the bulk ordering temperature, the 3q state exists everywhere and begins to order sharply. At a temperature below the bulk ordering temperature the system prefers a 2q state to form in the near-surface region, and so a magnetisation profile is set up corresponding to the intensity of the third order that the near-surface prefers not to have. Since a magnetisation profile exists, one can assign an interface width to it and try to apply wetting-like ideas. However, this situation would correspond to the wetting of the bulk by the 2q state as the temperature is increased, which will not occur due to energetics. One can instead consider the wetting of the surface by the bulk, whereupon the interface width can be considered instead to go from infinity to a finite value at the temperature at which the system prefers the 2q state to reside in the near-surface region. It is unclear as to whether this can be termed a wetting transition. Also, the relationship to disorder, the parameter measured by the experiments, is not clear and thinking of the 2q-3q interface as an ingredient to a *wetting* phenomenon does not seem to give any useful insight into the problem.

A different theory is proposed instead. Although the unusual change in rate of disordering parallel to the surface at a temperature below the bulk ordering temperature could be interpreted as a first order phase transition, it could in fact just be a sharpish but *continuous* change in the disorder measured parallel to the surface. Thus, as opposed to a pre-wetting-like jump in the domain wall location towards the bulk, there is also the possibility that at this temperature the interface location merely begins to fluctuate over a depth which is the length scale of the probe.

Chapter 8

CONCLUSION AND DISCUSSION

8.1 Conclusions

Most magnets react to a surface in quite a dull way; the loss of magnetic interactions at the surface weakens the magnetism there, allowing the paramagnetic state to nucleate there first but otherwise offering no new physics. However, we have considered two phenomena that occur in multiple-q systems: magnetic relaxation and magnetic reconstruction. The collinear configuration in normal magnets, being ferromagnets or bipartite magnets, does not reorient to gain back energy at the surface. This is a result of there being no change in the direction of the local field of the surface spins on the introduction of a surface, since the underlying magnetism is collinear, and additionally no degeneracy available, leaving no ability to superimpose another state to obtain a non-collinear local field and reorientation.

Multiple-q systems however possess an interesting property - degeneracy exists between states that are related by a rotational symmetry of the Hamiltonian. This degeneracy leads to the possibility of states possessing two or three magnetic orders, corresponding to putting spin density down at more than one distinct Bragg momentum location in reciprocal space.

The first consequence of this property is the ability of a multiple-q magnet to reorient near the surface to gain back some energy from the missing bonds by de-

creasing spin density at one Bragg momentum location and redistributing to the other two orders already present. This is termed a magnetic surface relaxation. The relaxation does not involve the introduction of any new order at the surface, and as such the relaxation configuration is taken at the bulk ordering transition.

The second consequence of the property is the ability to magnetically *reconstruct* at the surface, a new phenomenon that has not been proposed before. For systems which do not take all magnetic orders available to the multiple-q magnet in the bulk, there leaves the opportunity to take the remaining magnetic order(s) at the surface to gain back energy from lost bonds. Our analysis was concerned with the square lattice and type-1 FCC lattice and a single-q state was considered in the bulk. Due to the single-q states of a multiple-q magnet being related by a rotational symmetry of the Hamiltonian, and importantly not a trivial global rotation of all spins but of the lattice, each state possesses different translational symmetries. As such, the states react to a surface in different ways and the case of the bulk taking a state that is one that is not preferred energetically by the surface layer becomes possible. Additionally, the states are close to degeneracy in multiple-q systems, with the degeneracy being broken by magnetoelastic distortions, and can be superimposed orthogonally. The orthogonal superimposition allows for a low domain wall cost, which consists of a multiple-q state of varying spin density ratios. In this way, the domain wall cost solely involves the energetic cost of having a state that is not the ground state in the bulk and also spin-orbit effects.

Once the system orders in the bulk to become one of these single-q states, magnetoelastic distortions can detune the system slightly off degeneracy in real systems. If the bulk has chosen a state that does not favour the surface, then as the surface is approached the bulk state can reconstruct. The domain mixture present in the bulk cannot be overturned by surface effects, and as such domains exist in the bulk of real materials that would be expected to reconstruct. Therefore in real systems as the bulk domain structure meets the surface the surface-preferred domain is ex-

pected to provide a *cap*, yielding a few layers with a magnetically equivalent state across the entire surface, which smoothly decays into the bulk, being replaced by the underlying bulk domain structure.

This surface phase can develop at a phase transition that is distinct from the bulk transition. Specifically, the surface transition occurs at a *lower* temperature than the bulk transition, due to there being reduced magnetic coupling at the surface. Additionally, the surface phase can suffer its own internal transitions whilst the bulk behaviour remains unaffected. Hence it appears that there are good physical reasons for experimentally studying the magnetic properties of the surfaces of such magnets.

Our investigation of the uranium dioxide system that involves a surface provides a solitonic spin structure pinned to the surface at $T = 0$. This relaxation phenomenon is as a result of the system being triple-q and thereby having access to the variation of the different magnetic orders, allowing a double-q state to be approached as the surface is approached from the bulk. It has since been determined theoretically by Long *et al* [14] that there is a surface mode amounting to fluctuations of the position of the soliton which is the lowest energy excitation of the system and a picture appears in which the position of the soliton, or domain wall, moves further into the bulk as the temperature in increased. However, the idea of the interface delocalising and a wetting phenomenon occuring does not seem likely, since the free energies of the 2q and 3q states are never degenerate. As such, another explanation for the unusual disordering behaviour that occurs below the bulk ordering temperature is needed. It is proposed that the fluctuations of the location of the interface, which has disorder associated with it in the direction parallel to the surface, do not diverge or jump discontinuously into the bulk, but instead fluctuate over increasing length scales until crossing the length scale of the depth probe, which may explain the sudden onset of a larger disorder parameter.

8.1.1 Further Work

For the study of uranium dioxide, there are several points that need to be addressed. The Kosterlitz-Thouless (KT) transition has been proposed by other authors to explain the sudden change in the power law exponent describing lateral correlations in UO_2. The transition is associated with the unpairing of magnetic vortices as the temperature is increased past the transition temperature T_{KT}. This unpairing causes a sudden onset of disorder, and the ratio of the Néel temperature to the proposed KT temperature agrees with that predicted theoretically of 0.89. The author of this thesis has not yet studied this as a potential explanation.

In addition, there has been no detailed modelling that involves the introduction of temperature. The introduction of temperature to modelling is very hard and lengthy and this has not yet been achieved.

With respect to the magnetic reconstruction phenomenon, temperature again has not been included, and no materials have as yet been proposed in the literature to follow such a case. However, preliminary work by Long and Hopper seems to have provided materials for which the reconstruction would be expected to occur and the experimental signatures seem to support this theory. These findings lead one to the conclusion that whilst multiple-q systems are natural candidates for the surface reconstruction, in fact other systems also need to be considered. The requirement is solely for the symmetry of the state to be different such that the states react differently to a surface. The case of $FeBO_3$ [11][55] is an example of an 'accidental' degeneracy similar to that encountered in our square lattice model between a single-q state and a Néel state. In this case, the spin densities of the degenerate states are not related by a simple rotational symmetry of the Hamiltonian, but instead by the tuning of the interaction parameters. According to theoretical calculations [56] the bipartite antiferromagnet begins to develop a spiral character in the near-surface region as the transition temperature is approached, and it is this spiral that contains the new order that could be involved in a reconstruction at the surface.

For the case of hematite[57], the existence of more than one atom per unit cell leads to the possibility of states with different translational symmetries existing that are related by inversion rather than rotational symmetry of the Bragg spots. The bulk state consists of layers parallel to the surface which have robust sublattices, but which can rotate with respect to each other and also spiral from plane-to-plane for certain interaction parameter ratios.

Thus, for magnetic reconstruction, the main criteria can be contained in two points. Firstly, that the states possess frustration and for the bulk state to possess more frustration in a direction perpendicular to the surface than parallel. In this way, the loss of bonding at the surface costs energy. The second criterion is for there to exist another state close in energy that possesses a better ratio of frustrated to unfrustrated bonds with respect to the direction in which the surface is cut, such that more energy can be gained at the surface using this state in comparison with the bulk state. For the case of $FeBO_3$, the antiferromagnetically-aligned spins in neighbouring triangular planes which sit parallel to the surface are severed by a (111) surface, resulting in a large loss of magnetic energy. The interaction within the triangular planes is frustrated in the bulk. Another state exists close in energy in which the spin configuration within the planes is less frustrated, and it is this state that is taken by the surface in the reconstruction.

We have studied both magnetic surface relaxation and reconstruction and find that both phenomena can exist in multiple-q systems, and whatsmore that reconstruction is also expected to occur in other systems for which the general criteria are satisfied. This thesis has hopefully added to the richness of phenomena associated with multiple-q systems and provided frameworks with which to approach unusual surface-related phenomena.

List of References

[1] Corsin Battaglia, Katalin Gal-Nagy, Claude Monney, Clment Didiot, Eike Fabian Schwier, Michael Gunnar Garnier, Giovanni Onida, and Philipp Aebi. Elementary structural building blocks encountered in silicon surface reconstructions. *Journal of Physics: Condensed Matter*, 21(1):013001, 2009.

[2] JD Levine, SH McFarlane, and P Mark. Si (111) 7x7 surface structure: Calculations of leed intensity and comparison with experiment. *Phys. Rev. B*, 16(12):5415–5425, Dec 1977.

[3] FU Hillebrecht, H Ohldag, NB Weber, C Bethke, U Mick, M Weiss, and J Bahrdt. Magnetic moments at the surface of antiferromagnetic nio(100). *Phys. Rev. Lett.*, 86(15):3419–3422, Apr 2001.

[4] N Honda, Y Tanji, and Y Nakagawa. Lattice distortion and elastic properties of antiferromagnetic γ Mn-Ni alloys. *Journal of the Physical Society of Japan*, 41(6):1931–1937, 1976.

[5] MW Long and W Yeung. Spin-orientation phase transitions in itinerant multiple spin-density-wave systems. *Journal of Physics C: Solid State Physics*, 20(34):5839–5866, Dec 10 1987.

[6] RD Lowde, RT Harley, GA Saunders, M Sato, R Scherm, and C Underhill. On the martensitic transformation in f.c.c. manganese alloys. I. Measurements. *Proceedings of the Royal Society of London. Series A, Mathematical and Physical Sciences*, 374(1756):87–114, Jan 1981.

[7] BC Frazer, G Shirane, DE Cox, and CE Olsen. Neutron-diffraction study of antiferromagnetism in UO2. *Physical Review*, 140(4A):1448–&, 1965.

[8] RA Cowley and G Dolling. Magnetic excitations in uranium dioxide. *Physical Review*, 167(2):464–&, 1968.

[9] Karl D. Brommer, M. Needels, B. Larson, and J. D. Joannopoulos. Ab initio theory of the si(111)-(7x7) surface reconstruction: A challenge for massively parallel computation. *Phys. Rev. Lett.*, 68(9):1355–1358, Mar 1992.

[10] K Takayanagi, Y Tanishiro, S Takahashi, and M Takahashi. Structure-analysis of Si(111)-7X7 reconstructed surface by transmission electorn-diffraction. *Surface Science*, 164(2-3):367–392, Ded 1985.

[11] B Stahl, S Bhattacharya, S Gottschalk, J Ellrich, H Schmitt, J Ebert, M Ghafari, H Hahn, A Kamzin, D Vcherashniy, and AR Raju. Surface magnetism at the Neel temperature of an FeBO3 single crystal. *Physical Review B*, 66(10), SEP 1 2002.

[12] H Dosch. Surface-sensitive magnetic neutron Bragg scattering - Perspectives and limits. *Physica B*, 192(1-2):163–176, OCT 1993. Workshop on the use of neutrons and x-rays in the study of magnetism, Grenoble, France, Jan 21-23, 1993.

[13] GM Watson, D Gibbs, GH Lander, BD Gaulin, LE Berman, H Matzke, and W Ellis. X-ray scattering study of the magnetic structure near the (001) surface of uo_2. *Phys. Rev. Lett.*, 77(4):751–754, Jul 1996.

[14] MW Long and MS Hopper. unpublished paper.

[15] WL Roth. Neutron and optical studies of domains in NiO. *Journal of Applied Physics*, 31(11):2000–2011, 1960.

[16] WL Roth and GA Slack. Antiferromagnetic structure and domains in single crystal nio. *Journal of Applied Physics*, 31(5):S352–S353, 1960.

[17] GA Slack. Crystallography and domain walls in antiferromagnetic nio crystals. *Journal of Applied Physics*, 31(9):1571–1582, 1960.

[18] Methods of experimental physics, volume 23, part c. neutron scattering - magnetic structures.

[19] WL Roth. Multispin axis structures for antiferromagnets. *Physical Review*, 111(3):772–781, 1958.

[20] Hisamoto Kondoh and Tadao Takeda. Observation of antiferromagnetic domains in nickel oxide. *Journal of the Physical Society of Japan*, 19(11):2041–2051, 1964.

[21] N Cowlam, GE Bacon, and L Gillott. Changes in cell dimensions at martensitic transformation in γ-Mn-Cu alloys. *Journal Of Physics F: Metal Physics*, 7(12):L315–L319, 1977.

[22] RA Cowley and G Dolling. Magnetic excitations in uranium dioxide. *Phys. Rev.*, 167(2):464–477, Mar 1968.

[23] E Blackburn, R Caciuffo, N Magnani, P Santini, PJ Brown, M Enderle, and GH Lander. Spherical neutron spin polarimetry of anisotropic magnetic fluctuations in UO2. *Physical Review B*, 72(18), NOV 2005.

[24] MW Long. Effects that can stabilise multiple spin-density waves. *J.Phys.: Condens. Matter*, 1(17):2857–2874, 1989.

[25] MW Long and A Bayri. Spin impurities in noncollinear antiferromagnets with Mn_3Pt as an example. *Journal of Physics: Condensed Matter*, 5(41):7719–7736, Oct 11 1993.

[26] CL Henley. Ordering by disorder: Ground-state selection in fcc vector antiferromagnets. *Journal of Applied Physics*, 61(8, Part 2B):3962–3964, Apr 15 1987.

[27] CL Henley. Ordering due to disorder in a frustrated vector antiferromagnet. *Phys. Rev. Lett.*, 62(17):2056–2059, Apr 1989.

[28] MW Long. Multiple-Q structures in frustrated antiferromagnets. *International Journal of Modern Physics B*, 7(16-17):2981–3002, Jul 20 1993.

[29] Bidaux R Villain, J, JP Carton, and R Conte. Order as an effect of disorder. *Journal de Physique*, 41(11):1263–1272, 1980.

[30] MW Long and O Moze. Magnetic diffuse scattering and the triple-Q structure in FCC γ-MnNi. *Journal Of Physics: Condensed Matter*, 2(27):6013–6030, Jul 9 1990.

[31] H Uchishiba. Antiferromagnetism of γ-phase manganese alloys containing ni, zn, ga and ge. *Journal of the Physical Society of Japan*, 31(2):436–440, 1971.

[32] MW Long and W Yeung. Spin-orientation phase transitions in itinerant multiple spin-density-wave systems. *Journal Of Physics C: Solid State Physics*, 20(34):5839–5866, Dec 10 1987.

[33] RD Lowde, RT Harley, GA Saunders, M Sato, R Scherm, and C Underhill. On the martensitic transformation in f.c.c. manganese alloys. I. Measurements. *Proceedings of the Royal Society of London Series A-Mathematical Physical and Engineering Sciences*, 374(1756):87–114, 1981.

[34] MW Long, RD Lowde, and M Sakata. On the martensitic transformation in f.c.c. manganese alloys. IV. Associated magnetic transitions. *Phase Transitions*, 77(3):295–316, Mar 2004.

[35] TC Lubensky and Morton H Rubin. Critical phenomena in semi-infinite systems. ii. mean-field theory. *Phys. Rev. B*, 12(9):3885–3901, Nov 1975.

[36] AJ Bray and MA Moore. Critical behavior of semi-infinite systems. *Journal of Physics A: Mathematical and General*, 10(11):1927–1962, 1977.

[37] DL Mills. Surface effects in magnetic crystals near ordering temperature. *Physical Review B*, 3(11):3887–&, 1971.

[38] K Binder and PC Hohenber. Phase-transitions and static spin correlations in Ising models with free surfaces. *Physical Review B*, 6(9):3461–&, 1972.

[39] K Binder and PC Hohenber. Surface effects on magnetic phase-transitions. *Physical Review B*, 9(5):2194–2214, 1974.

[40] Phase transitions and critical phenomena vol. 10;field theoretic approach to critical behaviour at surface.

[41] K Binder and DP Landau. Crossover scaling and critical behavior at the "surface-bulk" multicritical point. *Physical Review Letters*, 52(5):318–321, 1984.

[42] H Nakanishi and ME Fisher. Multicriticality of wetting, pre-wetting, and surface transitions. *Physical Review Letters*, 49(21):1565–1568, 1982.

[43] JW Cahn. Critical-point wetting. *Journal of Chemical Physics*, 66(8):3667–3672, 1977.

[44] DM Kroll and R Lipowsky. Interface delocalisation transitions in semi-infinite systems. *Phys. Rev. B*, 28(11):6435–6442, Dec 1983.

[45] H Dosch, L Mailänder, H Reichert, J Peisl, and RL Johnson. Long-range order near the cu3au(001) surface by evanescent x-ray scattering. *Phys. Rev. B*, 43(16):13172–13186, Jun 1991.

[46] R Lipowsky and W Speth. Semi-infinite systems with first-order bulk transitions. *Phys. Rev. B*, 28(7):3983–3993, Oct 1983.

[47] H Reichert, PJ Eng, H Dosch, and IK Robinson. Thermodynamics of surface segregation profiles at Cu3Au(001) resolved by x-ray-scattering. *Physical Review Letters*, 74(11):2006–2009, MAR 13 1995.

[48] H Dosch, L Mailänder, A Lied, J Peisl, F Grey, RL Johnson, and S Krummacher. Experimental evidence for an interface delocalization transition in cu3au. *Phys. Rev. Lett.*, 60(23):2382–2385, Jun 1988.

[49] S Langridge, D Gibbs, GH Lander, JJ Betouras, N Gidopoulos, MW Long, C Vettier, H Zajonz, and GM Watson. unpublished. *fix this!!!!!*, 77(4):751–754, Jul 1996.

[50] AJ Freeman, JP Desclaux, GH Lander, and J Faber. Neutron magnetic form factors of uranium ions. *Physical Review B*, 13(3):1168–1176, 1976.

[51] J Faber and GH Lander. Neutron-diffraction study of UO2 - antiferromagnetic state. *Physical Review B*, 14(3):1151–1164, 1976.

[52] IK Robinson and DJ Tweet. Surface x-ray-diffraction. *Reports on Progress in Physics*, 55(5):599–651, MAY 1992.

[53] R. Feidenhans'l. Surface structure determination by x-ray diffraction. *Surface Science Reports*, 10(3):105 – 188, 1989.

[54] WP Su, JR Schrieffer, and AJ Heeger. Soliton excitations in polyacetylene. *Phys. Rev. B*, 22(4):2099–2111, Aug 1980.

[55] B Stahl, E Kankeleit, R Gellert, M Müller, and A Kamzin. Magnetic phase in the near-surface region of an $febo_3$ single crystal. *Phys. Rev. Lett.*, 84(24):5632–5635, Jun 2000.

[56] MW Long and MS Hopper. unpublished.

[57] MW Long and MS Hopper. unpublished.